Experimental Spectroscopic and Theoretical Studies of Organic Compounds and Polymeric Structures

By

John P. Ryall

[B.Sc. (Hons), Chemistry]

A thesis submitted in partial fulfilment of the requirements of the University of Greenwich for the Degree of Doctor of Philosophy in Chemistry

August, 2010

School of Science
University of Greenwich, Medway Campus,
Chatham Maritime,
Kent ME4 4TB, UK

ACKNOWLEDGEMENTS

Firstly, I would like to express my sincere gratitude to Professor Babur Z. Chowdhry and Dr Trevor J. Dines for their steadfast support.

I would also like to thank: Professor Steve Leharne.

Dr Andrew Mendham is thanked for his humour and hands on advice and Dr Louise Gracia for her expertise in ‘cooking up’ microgels.

Many thanks to Julia May for foreseeing the future and Julia Borwick for making it look good.

And finally, Dr Philip Steadman for ensuring I arrived at this point in time with a smile.

ABSTRACT

Experimental Spectroscopic and theoretical Studies of Organic compounds and Polymeric Structures

Solid state IR and Raman as well as aqueous solution state Raman spectra are reported for urazole, 4-methylurazole and their deuterated derivatives. DFT calculations, at the B3-LYP/cc-pVDZ level, established that the structures and vibrational spectra of the molecules can be interpreted using a model with hydrogen-bonded water molecules, in conjunction with the conductor-like polarizable continuum solvation method. The vibrational spectra were computed at the optimised molecular geometry, enabling normal coordinate analysis, which yielded satisfactory agreement with the experimental IR and Raman data. Computed potential energy distributions of the normal modes provided detailed vibrational assignments. Solid-state pseudopotential-plane-wave DFT calculations, using the PW91 functional, were also carried out reflecting the importance of intermolecular hydrogen bonding in the solid state.

Solid state IR and Raman as well as aqueous solution state Raman spectra are reported for the anions of urazole and 4-methylurazole, and their *N*-deuterated derivatives. DFT calculations, at the B3-LYP/cc-pVTZ level, established that the structures and vibrational spectra of both anions can be interpreted using a model that incorporates hydrogen-bonded water molecules, in conjunction with the polarizable continuum solvation method. In the case of the urazole anion it is shown that deprotonation occurs primarily at N1 rather than N4, but there is also evidence for the second tautomeric structure in both in the solid state and in aqueous solution. The vibrational spectra were computed at the optimised molecular geometry in each case, enabling normal coordinate analysis, which yielded satisfactory agreement with the experimental IR and Raman data. Computed potential energy distributions of the normal modes provided detailed vibrational assignments.

IR and Raman spectra have been obtained for N, N'–dicyclohexylcarbodiimide (DCC) in the solid state and in $CHCl_3$ solution. Structures and vibrational spectra of isolated gas phase DCC molecules with C_2 and C_i symmetries, computed at the B3-LYP/cc-pVTZ level, show that the IR and Raman spectra provide convincing evidence for a C_2 structure in both the solid and $CHCl_3$ solution states. Using a scaled quantum-chemical force field these DFT calculations have provided detailed assignments of the observed IR and Raman bands in terms of potential energy distributions. Comparison of solid state and solution spectra, together with a Raman study of the melting behaviour of DCC, revealed that no solid state effects were evident in the spectra.

Homopolymeric poly(N-isopropylacrylamide) and poly(4-vinylpyridine) as well as copolymer poly(N-isopropylacrylamide/4-vinylpyridine) [poly(NIPAM/4-VP)] microgels (the latter synthesized using percentage composition of 4-VP in the range of 7.5 – 90 %, w/w in the original reaction mixture) were prepared by surfactant-free emulsion polymerization. Freeze-dried samples of the microgels were subjected to analysis by Raman spectroscopy using 632.8 nm exciting radiation from a helium-neon laser. The Raman spectral profiles of the different microgels are compared and contrasted in the 600-1100 cm^{-1} wavenumber region. In the case of the poly(NIPAM/4-VP) copolymer microgels, differing in monomer composition, Raman spectroscopy can be employed as a quick/easy method to ensure that co-polymerization has occurred and also to determine, semi-quantitatively, the percentage incorporation of the 4-VP monomer.

John P. Ryall [B.Sc. (Hons)]

DEDICATION

This thesis is dedicated to

Julia,

Ewen & William

"Man will occasionally stumble over the truth,
but most of the time he will pick himself up
and continue on."

Winston Churchill

CONTENTS

FIGURES

TABLES

ABBREVIATIONS

Symbol	**Description**
Å	*angstrom*
λ_{max}	*absorption maximum*
AM	*acrylamide*
ATR	*attenuated total reflectance*
BA	*bisacrylamide*
k	*Boltzmann's constant*
Cd	*cadmium*
c.f.	*cartesian force constants*
CCD	*charge coupled device*
C=O	*carbonyl group (amide)*
cm	*centimetre*
ΔE	*change in energy*
μ	*component of electric dipole moment operator*
Co	*cobalt*
CPCM	*conductor-like polarizable continuum model*
g	*degeneracy of the levels n and m*
DCC	*N, N'–dicyclohexylcarbodiimide*
DFT	*density functional theory*
D_e	*dissociation energy*
DMSO	*dimethylsulfoxide*
^oC	*degree Celsius*
g_n / g_m	*degeneracy of the state*
ε	*dielectric constant*
K_a	*dissociation constant*
E	*electromagnetic radiation*
EM	*electromagnetic field*
μ	*electric dipole moment*
FFR	*far-from-resonance*
ω	*frequency*
k	*force constant*
FT	*Fourier transform*
FT-IR	*Fourier transform infra-red*
f.w.h.m.	*full-width-half-maximum*

Symbol	**Description**
V^X	*functional derivative of the exchange correlation energy*
v	*frequency*
g/mm	*grooves per millimetre*
GC-MS	*gas chromatography-mass spectroscopy*
GGA	*generalized gradient approximations*
GPa	*giga Pascal (bulk modulus)*
g/mol	*gram per mole*
He/Ne	*helium/neon*
HF	*Hartree-Fock*
HPLC	*high performance liquid chromatography*
H-GGA	*hybrid density functional methods*
HCl	*hydrochloric acid*
H	*magnetic*
IR	*infrared*
δ	*in-plane bending modes*
r	*inter-atomic distance*
I	*intensity*
IEF-PCM	*integration equation formalism polarization continuum model*
INS	*inelastic neutron scattering*
I_o	*intensity of excitation light*
I_R	*intensity of Raman field*
K	*Kelvin*
kDa	*kilo-daltons*
LDA	*local density approximation*
LSDA	*local spin density approximation*
pKa	$-\log_{10}(K_a)$
MCT	*mercury, cadmium,tellerium*
M.F.	*molecular formula*
M.W.	*molecular weight*
M.P.	*melting point*
MAA	*methacrylic acid*
MEOH	*methyl alcohol*
mg	*milligram*
mL	*millilitre*

Symbol	**Description**
mm	*millimetre*
mW	*milliwatt*
α	*molecular polarizabilty*
mol dm^{-3}	*mol per litre*
MM	*molecular mechanics*
N_2	*nitrogen*
Q	*normal coordinate*
N_m	*number of molecules in ground-energy level m*
N_n/N_m	*number of molecules in excited and ground state*
N_n	*number of molecules in the excited vibrational energy level n,*
NCA	*normal coordinate analysis*
NMR	*nuclear magnetic resonance*
γ	*out-of-plane bending mode*
ORD	*optical rotary dispersion*
h	*Planck's constant*
KBr	*potassium bromide*
P	*propagation*
V	*potential energy*
PES	*potential energy surface*
p.e.d.s	*potential energy distributions*
PCM	*polarization continuum model*
PCS	*photon correlation spectroscopy*
Poly(NIPAM)	*poly(N-isopropylacrylamide)*
Poly(NIPAM/4-VP)	*Poly (N-isopropylacrylamide/ 4-vinylpyridine)*
^{1}*H-NMR*	*proton nuclear magnetic resonance*
PSPW	*pseudopotential-plane-wave*
Q	*normal coordinate*
RP-HPLC	*reverse phase HPLC*
SES	*single-electronic state*
S/N	*signal to noise ratio*
STOs	*Slater orbitals*
c	*speed of light*
v	*stretching vibration*
SERS	*surface enhanced Raman spectroscopy*

Symbol	**Description**
T	*temperature (in Kelvin)*
TEM	*transmission electron microscopy*
τ	*torsional mode*
$\rho(r)$	*total electron density in space, r*
UV/vis	*ultra-violet/visible*
q	*vibrational coordinate*
υ	*wavenumber*
vib	*vibration*
λ	*wavelength*
ψ	*wave function*
X-ray	*X-ray crystallography*

Abbreviations for vibrational modes

ν = stretch, δ = deformation, ω = wag, τ = twist, ρ = rock, s = symmetric,
as = asymmetric, ip = in-plane, op = out-of-plane, b = bend

1. Introduction

This body of work reports a series of investigations using a combination of experimental techniques and theoretical calculations.

Chapter Two outlines the theoretical background to experimental and analytical techniques used to obtain the vibrational spectra and/or molecular structure of the molecules investigated. This chapter is divided into parts. The first part focuses on dispersive Raman spectroscopy and related techniques, the second part describes FT-IR and then finally chemical computational methods (density functional theory (DFT) calculations) are discussed.

Chapter Three details the experimental techniques and theoretical methods, together with the instrumentation used for Raman and FT-IR analysis of the examined molecules. Also methods employed for the preparation of freeze dried samples microgels prior to spectroscopy of colloidal nanoparticles. In addition DFT calculations and normal coordinate analysis and computational method used for structural determination and band assignments, respectively are discussed.

Chapter Four reports on experimental and theoretical vibrational spectroscopic studies of urazole and 4-methylurazole. Urazole (1,2,4-triazolidine-3,5-dione), is a 5-membered ring species which is found in a large number of organic compounds. There have been suggestions that it may have been a prebiotic compound acting as the precursor to uracil. Due to its structural "simplicity", urazole is an excellent candidate for detailed vibrational spectroscopic study and the examination of the influence of hydrogen bonding in aqueous solution and in the solid state. Previously reported calculations were based upon the assumption of isolated molecules in the gas phase.

Chapter Five reports measurements of the IR and Raman spectra of the mono-anions of urazole and 4-methylurazole species at high (alkaline) pH in aqueous solution, and in the solid state. The acidic properties of urazole and numerous substituted urazoles, have been reported previously by other researchers who established that the pK_a for both urazole and 4-methylurazole is 5.8 in aqueous solution but in DMSO the $pK_a = 13.1$ for urazole and 12.3 for 4-methylurazole. This being attributed to the much smaller pKa values in aqueous solution for the stabilization of urazole anions via hydrogen-bonding interactions. Significantly, in the case of urazole the possibility exists of deprotonation at either the N1 or N4 nitrogen atoms. Using a combination of IR and Raman spectroscopy, in conjunction with DFT calculations, the influence of hydrogen bonding on the structures of the urazole and 4-methylurazole anions is investigated, with a view to demonstrating that the vibrational spectra of the urazole anion are consistent with deprotonation at the N1 nitrogen atom, in agreement with previously reported NMR evidence, in both aqueous solution and in the solid state.

Chapter Six reports on studies of N, N'-dicyclohexylcarbodiimide (DCC), which is a widely used laboratory reagent e.g. as a carboxyl group activating agent in peptide synthesis, and for investigating biochemical systems. More recently carbodiimide chemistry has been employed for the functionalisation of carbon nanotubes and gold nanoparticles. No X-ray crystal structure of DCC had been reported, presumably because of the difficulty in obtaining diffraction quality crystals. It was therefore not known whether DCC has a *cis* or skew C_2 structure with a linear of nonlinear NCN group, or a *trans* C_i structure with linear NCN group. For this reason a detailed study of the IR and Raman spectra of DCC, supported by DFT calculations was undertaken with the objective of relating structural and vibrational spectral characteristics. The IR and Raman spectra of DCC have not previously been reported; DCC IR and Raman spectra have been obtained in the solid state and in $CHCl_3$ solution. Structures and vibrational spectra of isolated gas phase DCC molecules with C_2 and C_i symmetries were computed at the B3-LYP/cc-pVTZ level. By comparing IR and Raman spectra in both solid and solution states with the results of DFT calculations for C_2 and C_i structures with equatorial cyclohexyl rings it is suggested that DCC has a C_2 structure.

Chapter Seven reports on a study of co-polymer microgels, using dispersive Raman spectroscopy. It was found that using this technique, for the first time, poly(NIPAM-co-4-vinylpridine) co-monomer microgels could be analysed, semi-quantitatively, in relation to their monomer composition.

Finally, Chapter Eight provides a summary of the work presented in this thesis and a brief discussion on future research prospects relating to the molecules examined. An addendum is provided which incorporates appendices of work not included in the main body of the thesis together with a list of publications.

2. Theoretical Aspects of Techniques and Computational Methods

2.1. Theoretical Aspects

2.1.1. Introduction to Optical Spectroscopy

The classical theory of light proposed by Maxwell, Young, and others in the nineteenth century demonstrated that light could be considered as a form of rapidly oscillating electromagnetic field (EM). The interaction of EM radiation with matter can be used to extract very useful information, both structural and other physico-chemical data, about molecules. This is the basis of spectroscopy which involves the absorption and emission of electromagnetic radiation by a sample followed by interpretation of the measured spectral parameters to obtain either macroscopic and/or specific molecular information.

Electromagnetic radiation consists of two vector components orthogonal to each other: one is electric (**E**) and the other is magnetic (**H**) (Figure 2.1). They are produced by oscillating electric or magnetic dipoles and are propagated through a vacuum at the speed of light, *c* (3 x l08 ms^{-1}). In Figure 2.1 plane or linearly polarized light is shown, because the **E** vector oscillates in one plane. Un-polarized (isotropic) light contains oscillations of the **E** vector in all directions perpendicular to the direction of propagation (**P**).

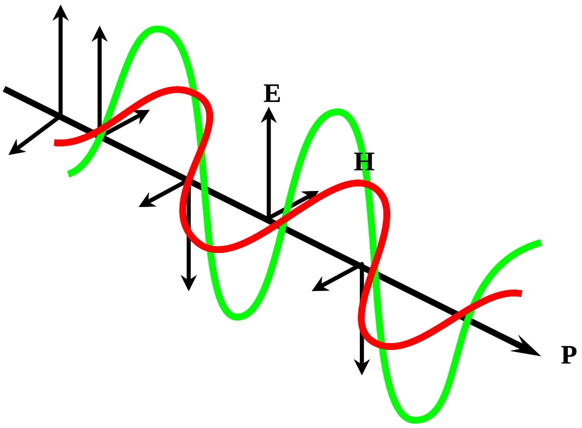

Figure 2.1 Plane-polarized light comprised of electric and magnetic vectors perpendicular to each other.

The frequency (ν) and wavelength (λ) of radiation are related by the equation:

$$\nu = c / \lambda \qquad (2.1)$$

Frequency can be directly converted into energy units using the relationship:

$$E = h\nu \qquad (2.2)$$

where h is Planck's constant[1,2] (6.63 x 10^{-34} Js^{-1}) and energy, E (J), frequency, ν (Hz), and wavelength, λ (m).

2.2. Vibrational Spectroscopy

The vibrational frequencies of a molecule can be determined by two fundamentally different spectroscopic techniques:

- IR, first systematically used by W. Coblentz in 1905[3]
- Raman spectroscopy which was theoretically predicted in 1923 by A. Smeckel[4] and experimentally observed in 1928 by C. V. Raman and K. S. Krishnan[5].

Both FT-IR and Raman depend on the interaction of electromagnetic radiation with matter, but the physical basis of the two techniques is fundamentally different. As a consequence, the two techniques are often considered complementary; a more complete analysis is therefore often only obtained by combining the two techniques.

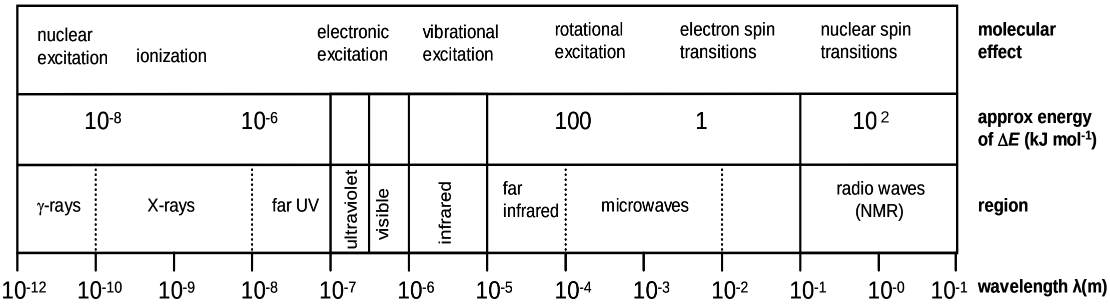

Figure 2.2. Diagram illustrating the various regions of the electromagnetic spectrum with their defining wavelengths, plotted on an approximate logarithmic scale.

2.2.1. Molecular Vibrations

Figure 2.2 shows a list of spectroscopic techniques and their relationship to the electromagnetic spectrum[6,7]. It also shows where molecular vibrations are normally observed in the mid IR region, *i.e.* at wavenumbers from 200-4000 cm^{-1} (see). A diatomic molecule can be represented in a macroscopic model by two masses, m_1 and m_2, connected by an elastic spring. This system will oscillate about an equilibrium distance, r_e, if it is distorted by a distance Δr, and then released. The oscillation is caused by the restoring force for the vibration *f*.[8-11] In the first approximation *f* is proportional to, and opposed to, the distortion (Hooke's law):

$$f = -K\Delta r = \mathrm{K}(r-r_e) \qquad (2.3)$$

The proportionality factor "*K*", is called the force constant in the case of molecular vibrations and *r* is the distance between the atoms. The calculation of "*K*" is a measure of the bond strength.

Hooke's Law equation also gives the relationship between frequency, the mass of the atoms involved in the vibration and the bond strength for a diatomic molecule:

$$\nu = \frac{1}{2\pi c}\sqrt{\frac{K}{\mu}} \qquad (2.4)$$

$$\mu = \frac{m_1 m_2}{m_1 + m_2} \qquad (2.5)$$

2.2.2. The Harmonic Oscillator

The potential energy (*V*), of a diatomic system, as a function of the inter-atomic distance, *r*, is obtained by integration of equation 2.3 as:

$$V(r) = \frac{1}{2}\left[k(\Delta r)^2\right] = \frac{1}{2}\left[k(r - r_e)^2\right] \qquad (2.6)$$

and therefore has a parabolic shape (Figure 2.3). The potential energy (*V*) and the vibrational motion are said to be harmonic, since they depend on a force proportional to the square of the displacement.

From the quantum theoretical treatment of the ‘harmonic oscillator’ the energy eigenvalues, E_v, are obtained:

$$E_v = h\nu_{vib}\left(n + \frac{1}{2}\right) \qquad (n = 0,1,2,.......) \qquad (2.7)$$

where ν_{vib} is the frequency of the oscillation and n is the vibrational quantum number which distinguishes the vibrational levels.

2.2.3. The Anharmonic Oscillator

A more realistic treatment uses the anharmonic oscillator model (Figure 2.3). In this case the potential energy is approximated by the Morse potential:

$$V(r) = D[1 - \exp\{-a(r - r_e)\}]^2 \qquad (2.8)$$

This corresponds to an asymmetric potential with curvature characterized by the constant a. D is the sum of the zero point energy, D_o, and the dissociation energy, D_e. Energy values are obtained by the quantum theoretical treatment of the anharmonic oscillator:

$$E_\upsilon = h\nu'_{vib}\left[\left(n + \frac{1}{2}\right) - x\left(n + \frac{1}{2}\right)^2\right] n = 0,1,2,....... \qquad (2.9)$$

The anharmonicity constant (x) is a measure of the deviation from the harmonic case. In real systems $x > 0$, so the energy difference between successive vibrational levels decreases as n increases until the dissociation energy of the molecule is attained.

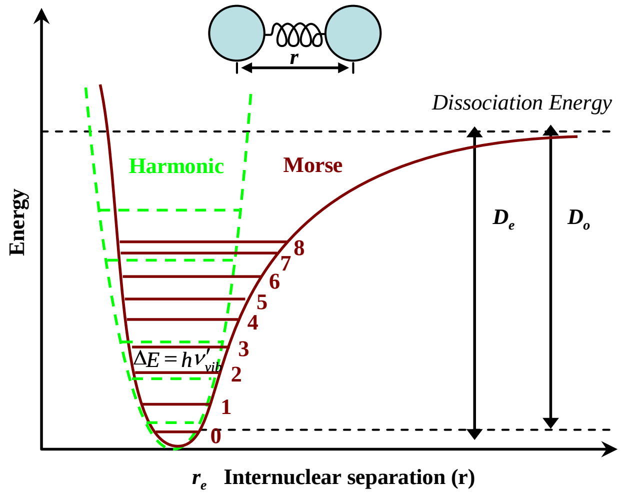

Figure 2.3. Potential energy curves for a simple harmonic oscillator and anharmonic (the Morse) oscillator.

Potential energy curves for a simple harmonic oscillator and anharmonic (the Morse) oscillator. The dissociation energy of a molecule, D_o, differs from the depth of the potential well, D_e, on account of the zero potential energy of the vibrations of the bond. The ground state corresponds to $n = 0$ with an energy $E_\upsilon = {}^1\!/_2\, h\nu'_{vib}; n = 1$ describes the first excited level $(E_1 = {}^3\!/_2\, h\nu'_{vib})$ etc. The difference between the two successive energy levels ΔE is the same for all levels $\Delta E = h\nu'_{vib}$.

2.2.4. Fundamental or Normal Modes of Vibrations

A normal mode is defined by the following conditions:

- an independent, synchronous motion of atoms, or groups of atoms,
- the vibrational motion does not cause a translation or rotation of the molecule as a whole,
- each normal mode of vibration is excited independently.

A normal mode of vibration is usually not localized at a single bond in a molecule, but includes several atoms. The vibrational motion is described by the normal coordinate, *Q*. The number of normal modes of vibration and consequently the number of normal coordinates follow from simple considerations.

A system of *N* particles has *3N* degrees of freedom corresponding to the three independent coordinates of each of the *N* particles. Three of these degrees of freedom are taken up by the translations of the entire molecule along the x, y, and z axes and another three by the rotation of the molecule about the three principle axes of inertia. Linear molecules have only two rotational degrees of freedom because the moment of inertia along the molecular axis is zero. The number of remaining vibrational degrees of freedom n is identical to the number of fundamental vibrations, that is:

$n = 3N - 3 - 3 = 3N - 6$ (for a non-linear molecule), and (2.10)

$n = 3N - 3 - 2 = 3N - 5$ [10,11] (for a linear molecule) (2.11)

It will become evident in the following discussion that a particle description of the vibrational degrees of freedom is not based on a Cartesian coordinate system but on internal coordinates, which correspond to bond lengths and angles.

2.2.5. Classification of Normal Modes of Vibration

Various criteria can be used to characterize normal modes of vibration.

2.2.5.1. *Classification by Type*

Four main types of vibrations can be distinguished:

- stretching vibrations (ν), where one or more of the bond lengths change during the course of vibration.
- in-plane bending modes (δ); one or more bond angles change, while bond lengths remain constant.
- out-of-plane bending modes (γ); one atom oscillates through a plane defined by at least 3 neighbouring atoms.
- torsional modes (τ); a dihedral angle (the angle between two planes, which have one bond in common) is changed, *i.e.* rotation of a methyl group.

2.2.5.2. *Classification by Symmetry*

According to symmetry, normal modes of vibration can be classified as follows:

- symmetric vibrations (s), where the symmetry of the molecule is retained throughout,
- asymmetric vibration (as), where one or more of the symmetry elements of the molecule vanish during the vibration, and

- in highly symmetric molecules degenerate vibrations can occur. In this case two or more vibrations, depending on the degree of degeneracy, have different coordinates but the same energy.

2.2.5.3. *Combinations and Overtone Vibrations*

Two further types of vibrations may be distinguished from the normal, or fundamental, vibrations: combination bands[12] occur at frequencies, ν_c, and are obtained by the combination of the frequencies (or multiples thereof) of one or more fundamental vibrations ($\nu_c \simeq a\nu_1 \pm b\nu_2 \pm .....$; where *a*, *b*, are integers); overtones occur at approximately twice or three times the frequencies of the respective fundamental vibrations $\left(\nu_{o,n} \simeq n\nu_1\right)$. Group theory and the symmetry of the molecule determine which of these vibrations are allowed and observed in the spectrum. Combination and overtone bands are usually observed with much lower intensities than normal vibrations. The Fermi resonance[13,14] represents a special case. If a combination or an overtone coincides approximately with a fundamental vibration then the frequencies move apart and two separate bands with more or less equal intensities are observed. The separate assignment of these bands to different vibrations is then difficult.

2.2.6. FT-Infrared Absorption Spectroscopy

In IR, the frequency of the incident radiation is varied continuously and the transmittance/absorbance of the radiation through the sample is plotted against the incident frequency (more usually wavenumber, cm^{-1}). The vibrations detected by IR spectroscopy are those that produce a change in the dipole moment of the molecule. IR spectroscopy can be divided into three areas based on spectral region: far-IR (500-10 cm^{-1}), mid-IR (4000-400 cm^{-1}), and near-IR (13,300-4000 cm^{-1}). Far IR is used for the detection of very low frequency vibrations, such as the stretching of metal-metal bonds, and also for metal-ligand interactions. Mid-IR is the most commonly used form of vibrational spectroscopy, for both on line processing, and in the research laboratory. This information-rich (fingerprint) region contains all of the common vibrational energies of organic and non-metallic inorganic species.

IR absorption arises from a direct resonance between the frequency of the IR radiation and a particular vibrational transition, typically on the femtosecond time scale (10^{-15} sec). IR absorption is a one photon event. The IR photon is absorbed by the molecule, exciting the molecule into an elevated vibrational state. The excitation of fundamental vibrations as the transition from the vibrational ground state to the next energy level upon absorption of one quantum of light is shown in Figure 2.4:

$$E_1 - E_0 = h\nu_{vib} = E_{ph} = h\nu_{ph} \qquad (2.12)^{15}$$

Thus the basic requirement is that $\nu_{vib} = \nu_{ph}$ (ph = photon)

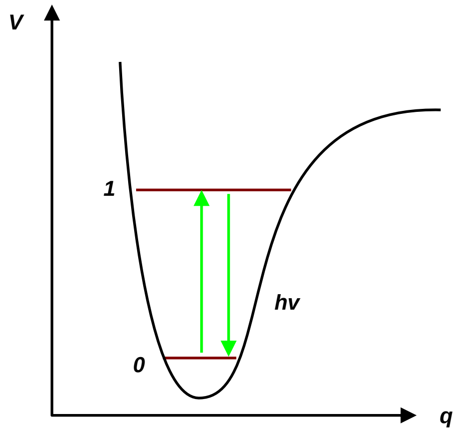

Figure 2.4. The excitation of fundamental vibration from the vibrational ground state to the next energy level (V is the potential energy, and q is the normal coordinate).

2.2.6.1. *Selection Rules for IR Spectroscopy*

A diatomic molecule will absorb IR radiation only if its dipole moment changes upon a change in the inter-nuclear distance. The transition probability is a product of the population difference between two quantum states (ΔN), and the square of the transition dipole moment (M):

$$\textit{transition probability} \sim \Delta N \text{ x } M^2 \qquad (2.13)$$

For a molecule in a given electronic state, the transition dipole moment for a vibrational transition is given by:

$$M = \int \Psi^*_{v''} \mu^{(e)}_{\circ} \Psi_{v'} d\tau \qquad (2.14)$$

The wave functions $\Psi_{v''}$ and $\Psi_{v'}$ represent the final and initial vibrational states, respectively, and $\mu^{(e)}_{\circ}$ is the permanent electric dipole moment in this electronic state. For the vibrational motion of a diatomic molecule, the permanent electric dipole moment can be expanded in a Taylor series about the equilibrium inter-nuclear separation, r_e:

$$\mu_{\circ}^{(e)} = \mu_e + \left(\frac{\partial \mu}{\partial r}\right)_{re} q + \frac{1}{2}\left(\frac{\partial^2 \mu}{\partial r^2}\right)_{re} q^2 + \ldots\ldots \quad (2.15)$$

where μ_e is the dipole moment, when the bond is in the equilibrium position. The probability for a vibrational transition occurring in a diatomic molecule can be derived by substituting the expanded form of the permanent electric dipole moment into the equation of the dipole moment for the vibrational transition:

$$\int \Psi_{v''}^{*} \mu_{\circ}^{(e)} \Psi_{v'} d\tau = \mu_e \int \Psi_{v''}^{*} \Psi_{v'} d\tau + \left(\frac{\partial \mu}{\partial r}\right)_{r_e} \int \Psi_{v''}^{*} q \Psi_{v}\, d\tau + \frac{1}{2}\left(\frac{\partial^2 \mu}{\partial r^2}\right)_{r_e} \int \Psi_{v''}^{*} q^2 \Psi_{v}\, d\tau + \quad (2.16)$$

The first term in equation 2.16 is equal to zero since the vibrational wavefunctions ($\Psi_{v''}$ and $\Psi_{v'}$) are orthogonal. The second term is non-zero if the dipole moment depends on the inter-nuclear distance (*r):*

$$\left(\frac{\partial \mu}{\partial r}\right) \neq 0 \qquad (2.17)$$

Therefore, diatomic molecules will only exhibit a vibrational absorption spectrum if there is a change in dipole moment during the vibrational motion. Homonuclear diatomic molecules, such as H_2 and N_2, have zero dipole moments and do not show vibrational absorption spectra. In general heteronuclear diatomic molecules have dipole moments that change with internuclear distance, and so they exhibit vibrational absorption spectra. Quantum mechanical theory specifies that absorption of IR light will only occur if a vibrational mode involves a change in dipole moment and that vibrational energy levels in molecules are quantized. The theory also dictates that transitions can take place between adjacent energy levels only when the integral in the second term for the Hermite polynomials, that describe the wavefunction of the harmonic oscillator, is non-zero i.e., $\Delta v = \pm 1$.

2.2.7. The Raman Effect

Raman scattering is a fundamental form of molecular spectroscopy. Together with IR absorption, Raman scattering is used to obtain information about the structure and physico-chemical properties of molecules from their vibrational transitions. The theory of Raman scattering is more complex than the theory of IR absorption, but there are a number of close parallels between the two theories. In contrast to IR, Raman scattering is a two-photon event. The interaction of the molecular polarizability with the incoming radiation creates an induced dipole moment in the molecule, and the radiation emitted by this induced dipole moment contains the observed Raman scattering. The induced electric dipole moment (μ) is proportional to the polarizability of the molecule:

$$\mu = \alpha E + 1/2\beta\, EE + 1/6\gamma\, EEE + ---- \qquad (2.18)$$

where α is the polarizability, β the hyperpolarizability, and γ the second hyperpolarizability of the molecule. The polarizabilities can be regarded as a measure of the flexibility of the electron cloud: the ease with which the electron cloud of the molecule can be deformed or displaced to produce an electric dipole under the influence of the external electric field. The nonlinear terms in equation 2.18 are usually so small compared to the linear term that they do not play a role in normal Raman scattering. Therefore we can neglect the non-linear terms in equation 2.18, and hence the following expression is obtained:

$$\mu = \alpha \mathrm{E} \qquad (2.19)$$

As stated above, we may consider the incident radiation to be plane-polarized. However, the effect is on the electron cloud of a molecule in all directions. Therefore α is not a simple proportionality constant, but a tensor. For example, the dipole moment may change along the Cartesian co-ordinates x, y and z *i.e.*:

$$\mu_x = \alpha_{xx}E_x + \alpha_{xy}E_y + \alpha_{xz}E_z \qquad (2.20)$$

Therefore, in order to describe the molecular polarizabilty of a molecule the polarisation angle of the linearly polarised laser light, and the polarizability components of the molecule have to be taken into account. In the above example α_{xx}, α_{xy}, α_{xz} are the components of the molecular polarizability tensor, where the first subscript refers to the direction of the molecular dipole, and the second refers to the polarisation of the incident irradiation.

Similar expressions can be derived for μ_y and μ_z; hence the polarizability of a molecule can be expressed as:

$$\begin{bmatrix} \mu_x \\ \mu_y \\ \mu_z \end{bmatrix} = \begin{bmatrix} \alpha_{xx}\alpha_{xy}\,\alpha_{xz} \\ \alpha_{yx}\alpha_{yy}\,\alpha_{yz} \\ \alpha_{zx}\alpha_{zy}\,\alpha_{zz} \end{bmatrix} \begin{bmatrix} E_x \\ E_y \\ E_z \end{bmatrix} \qquad (2.21)$$

The polarisation properties of a molecule become particularly important with respect to Raman studies of single crystals. For instance, all molecular axes can line up within a unit cell, in the same direction for each cell. Therefore, the polarisation of the incident laser beam bears a relationship to the molecular axes.

By analysing the polarisation of scattered light, each individual component of the tensor can be investigated. But this is only practicable[13,16] in single crystal polarisation studies where the crystal has a high symmetry space group. The light scattered by the induced dipole of the molecule consists of both Rayleigh and Raman scattering. Rayleigh scattering corresponds to the light scattered at the frequency of the incident radiation, whereas the Raman scattering is shifted in frequency, and hence energy, from the frequency of the incident radiation by the vibrational energy that is gained or lost in the molecule.

If a molecule gains vibrational energy (as shown in Figure 2.5b) the scattering is called Stokes scattering, whereas if the molecule loses energy (by starting from an elevated vibrational level), the process is known as anti-Stokes Raman scattering[13,17] (Figure 2.5c). The ratio of the intensities of the Stokes and anti-Stokes scattering is dependent on the number of molecules in the ground and excited vibrational levels which can be calculated from the Boltzmann equation,

$$\frac{N_n}{N_m} = \frac{g_n}{g_m} \exp\left[\frac{-(E_n - E_m)}{kT}\right] \qquad (2.22)$$

N_n is the number of molecules in the excited vibrational energy level (n), N_m is the number of molecules in the ground vibrational energy level (m), g is the degeneracy of the levels n and m. E_n-E_m is the difference in energy between the vibrational energy levels, k is Boltzmann's constant, and T is temperature (in Kelvin).

An energy level diagram is given in Figure 2.5, which illustrates Raman scattering.

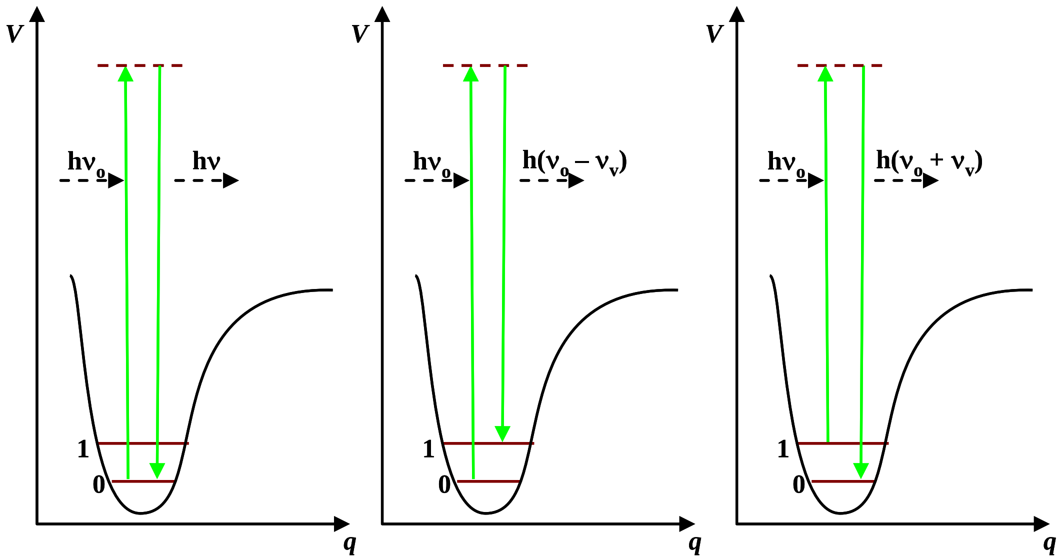

Figure 2.5. Schematic representation of energy transitions in: Rayleigh scattering (**a**), Stokes scattering (**b**) and anti-Stokes scattering (**c**).

The intensity of Raman scattering[16,18] is given by the expression:

$$I = Kl\left(\frac{\partial \alpha}{\partial q}\right)^2 \omega^4 \qquad (2.23)$$

where *K* is a constant and incorporates factors such as the speed of light, *l* is the power of incident light, ω is the frequency of the incident radiation, α is the molecular polarizability, and *q* is the vibrational coordinate. The intensity of Raman scattering is proportional to the incident light power, and the fourth power of the frequency of the incident light. The Boltzmann factor in the anti-Stokes formula accounts for the smaller (less intense) anti-Stokes signal compared to the Stokes signal, since anti-Stokes scattering results from molecules in the excited vibrational level which is less populated according to the Boltzmann distribution. Experimentally, the intensity of the Raman (Stokes) scattering is given by the expression:

$$I = KCI_{\circ}(\nu_{\circ} - \nu_{vib})^4 \qquad (2.24)$$

where *K* is a constant of the instrument, *C* is the concentration of the species responsible for the scattering, I_0 is the intensity of the incident beam. To summarize, in the "classical view" of the Raman effect light is considered an electromagnetic wave which induces a dipole moment in the molecule. The generation of this dipole moment by the incoming electric field is modulated by the molecular vibrations since α is a function of the vibrational coordinate, q. Therefore, the induced dipole oscillates not only at the frequency of the incoming field, but also at "side bands", at the sum and difference frequencies between the incoming light, and the molecular vibrations. This results in the appearance of Stokes and anti-Stokes "side bands" in the scattered light.

2.2.7.1. *Raman Cross-Section*

The Raman scattering cross-section for a molecular vibrational mode is defined as the number of scattered photons per unit time per unit solid angle divided by the incident laser flux (number of photons per unit time per unit area). For a totally symmetric mode, the expression for the cross-section for parallel incident and scattered light polarization is given by the following expression:

$$\frac{d\sigma}{d\Omega} = \frac{\omega_L \omega_s^3}{c^4} \frac{\hbar}{2\omega_f} \left(\langle n_f \rangle + 1 \right) \left| \alpha_f \right|^2 L \qquad (2.25)$$

where ω_L is the incident light angular frequency, ω_S the scattered light angular frequency, c the speed of light, ω_f the angular vibrational frequency of the Raman mode, and $<n_f>$ its mean occupation number. The factor L is a local field correction. The key molecular parameter which determines the Raman cross-section of a totally symmetric mode is the average α_f of the Raman tensor, which in the off-resonance limit can be written in terms of polarizability derivatives:

$$\alpha_f = \frac{1}{3}\left(\alpha_{xx,f} + \alpha_{yy,f} + \alpha_{zz,f} \right) \qquad (2.26)$$

The differential Raman scattering cross-section calculated from equation (2.25) is as follows:

$$\frac{d\sigma}{d\Omega} \approx 10^{-29} - 10^{-31} cm^2 \qquad (2.27)$$

Raman scattering is typically 14 orders of magnitude weaker than fluorescence; therefore, Raman signals are, in most cases, several orders of magnitude weaker than fluorescence emission[19].

To varying degrees Raman scattering is sensitive to all the excited electronic states of a molecule. If the incident photon energy approaches the transition energy of an excited electronic state, the Raman scattering changes from normal Raman scattering to resonance Raman scattering. The general theory of Raman scattering takes into account this complexity. One is the far-from-resonance (FFR) limit. This is a common situation for colourless samples that have no electronic states in close proximity to the incident photon energy. The other is the single-electronic state (SES) limit of strong resonance with a single electronic state of the molecule, and the resulting resonance Raman scattering is dominated by the properties of this resonant electronic state.

A closely related phenomenon to the Raman effect is fluorescence (Figure 2.6). Here the transition from ground to excited state is almost instantaneous (10^{-15} sec) and, to a good approximation, does not allow time for atomic nuclei to move during excitation (Franck-Condon principle).

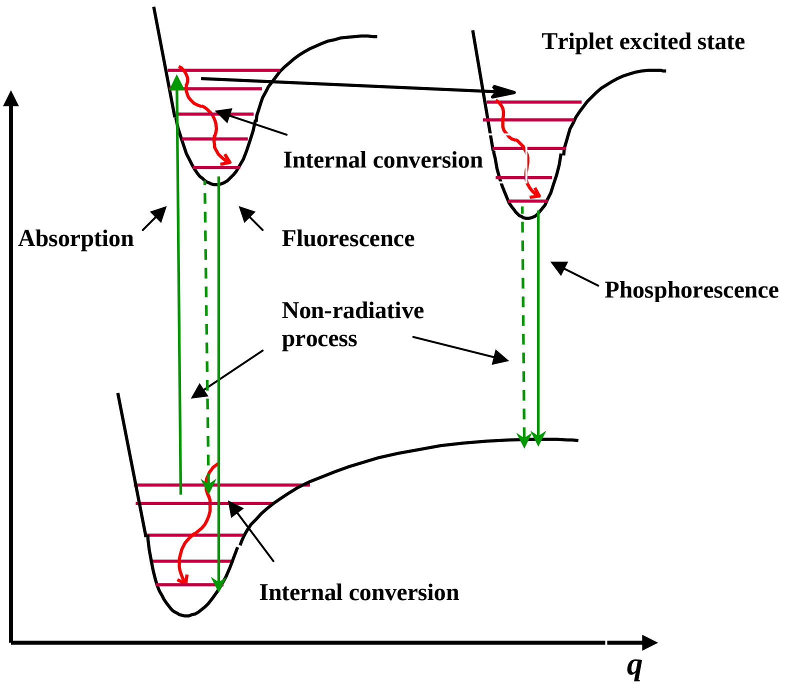

Figure 2.6. Physical basis of fluorescence and related phenomena.

Depending on the configuration of the molecule at the moment of excitation, any one of the several different vibrational levels in the excited state may be populated. Usually one of the upper vibrational levels of the excited state is excited rather than the lowest lying levels, and the electron relaxes to the lowest vibrational level within a few picoseconds of the absorption event; this process is called internal conversion (10^{-12} sec). Once the lowest vibrational level of the excited state is reached, one of several competing processes can ensue. These include: (1) decay to the ground state by emission of a photon (fluorescence, $\geq 10^{-10}$– 10^{-7}sec); (2) decay to the ground state by non-radiative process; and (3) intersystem crossing to the first excited triplet state, followed by decay back to the ground state (phosphorescence, $\geq 10^{-4}$sec). Because both fluorescence and phosphorescence result in the emission of a photon, they are collectively referred to as luminescence. [10,11,18,20,21]

2.2.8. Summary of Selection Rules for Vibrational Spectroscopy

As already described in order to determine whether a vibration is observed, either in IR or Raman spectra, selection rules must be applied to each normal vibration. Since the origins of infrared and Raman spectra are markedly different, their selection rules are also distinctly different. According to quantum mechanics a vibration is IR active if the dipole moment changes during the course of the vibration. Whereas a vibration is Raman active if the polarizability changes during the vibration.

Table 2.1. Comparison of infra-red and Raman spectroscopies

Parameter	**IR spectroscopy**	**Raman spectroscopy**
Interaction	Absorption	Scattering
Excitation of vibration	Polychromatic IR radiation	Monochromatic radiation (ν_o) usually in the visible range.
Frequency measurement	Absolute	Relative to the excitation frequency ν_o
Requirement for the activity of a vibration	$\left(\partial\mu/\partial Q\right) \neq 0$	$\left(\partial\alpha/\partial Q\right) \neq 0$
Band intensity	$I \propto \left(\partial\mu/\partial Q\right)^2$	$I \propto \left(\partial\alpha/\partial Q\right)^2$
Representation of the spectrum	Absorption logarithmic ‘downwards’	Intensity linear ‘upwards’
Advantageous spectroscopic technique for:	Routine analysis, gas analysis	Investigation of aqueous solutions, single crystals, polymers

2.2.9. Raman versus Infrared Spectroscopy

Despite the fact that Raman and IR spectroscopies are similar, in that they provide information on vibrational frequencies, each has its advantages and disadvantages.

2.2.9.1. *Advantages*

- Some vibrations are only Raman active while others are only IR active[9]. The extreme case of this is for molecules having a centre of symmetry, for which the rule of mutual exclusion applies. In general a vibration is IR active, Raman active or active in both; however, totally symmetric vibrations are only Raman active in molecules with high symmetry.
- Some vibrations are inherently weak in IR and strong in Raman spectra. Examples are the stretching vibrations of C≡C, C=C, P=S, S−S, and C−S bonds. In general, vibrations are strong in Raman if the bond is non-polar and strong in IR if the bond is polar. Bending vibrations are generally weaker than stretching vibrations, because, stretches are of higher energy resulting in larger dipole moments or polarizibility.
- In Raman spectra, Measurement of depolarization ratios may provide additional information about the symmetry of a normal vibration in solution by Raman spectroscopy. However, such information can not be obtained from IR spectra.
- Using the resonance Raman effect it is possible to selectively enhance vibrations of a particular chromophoric group in a molecule which is particularly interesting in vibrational studies of large biological molecules containing chromophoric groups, such as haemoglobin.
- Raman spectroscopy requires very little sample preparation and the sample size can be very small, although care must be taken not to thermally degrade the sample due to the intense laser. IR sample preparation is more tedious, *e.g.* preparation of KBr discs.
- Raman spectra of samples in aqueous solution can be obtained without major interference from water vibrations because of its poor scattering effect. Therefore, Raman spectroscopy is ideal for the studies of biological compounds in aqueous solution. In contrast, IR spectroscopy suffers from strong absorption of water. Raman spectra of hygroscopic and or air-sensitive compounds can be obtained by placing the sample in sealed glass tubing. Indeed the Raman spectra of samples in opaque containers can be obtained directly. In IR spectroscopy this is not possible since glass absorbs IR radiation.[11,18,20]

2.2.9.2. *Disadvantages*

- A laser source is needed to observe (weak) Raman scattering (only a very small quantity (*ca.* 1 in 10^5-10^7) of photons of shifted frequency are observed.); this intense source may cause local heating and/or photodecomposition, especially in resonance Raman studies where the laser frequency is deliberately tuned to the absorption band of the molecule.
- A major disadvantage of Raman spectroscopy is that many compounds fluoresce when irradiated by the laser beam. Intense fluorescence swamps the weak Raman signal.
- Raman scattering is not very sensitive for solutions (high concentrations of solute required).
- It is more difficult to obtain rotational and rotation-vibration spectra with high resolution in Raman than in IR spectroscopy. This is because Raman spectra are observed in the visible region where high resolving power is more difficult to obtain.
- A state-of-the-art Raman system costs substantially more than a conventional FT-IR spectrophotometer although less expensive versions have appeared which are smaller (miniaturized), portable and suitable for process applications.[11,18,20]

2.2.10. Depolarisation Measurements

As stated in the previous section, depolarisation ratios of Raman bands of aqueous or liquid samples, can give useful information regarding the symmetry of particular modes. For example modes can be either non-totally symmetric or totally symmetric with respect to the symmetry of the molecule. This is a valuable tool in assessing band assignments[10-13]. Polarisation ratios are obtained by the use of a polarisation analyser, as indicated in Figure 2.7.

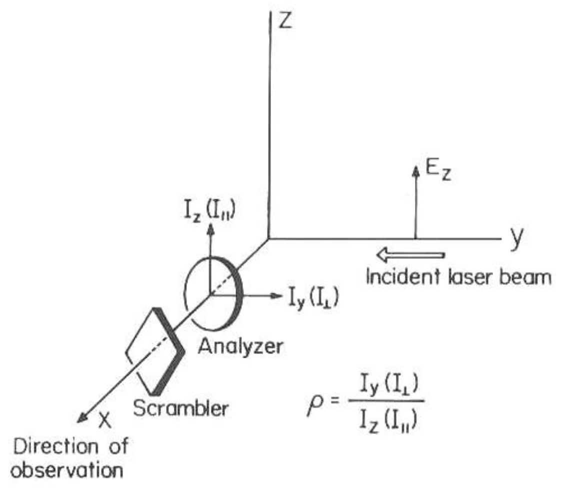

Figure 2.7. Diagram indicating solution polarisation studies.

As stated earlier, Raman scattering is due to an interaction between the radiation of plane polarised laser light, and the change in polarisability of a normal mode during vibration. From this interaction it is possible for some of the scattered radiation to be no longer plane polarised. Subsequently there may be a distinct difference between the intensity of a signal which is polarised parallel ($I_{\parallel}$) to the laser beam or polarised perpendicular to the laser beam ($I_{\perp}$). Raman signals can individually be observed using a polarisation analyser. Turning the analyser through 90° can change the observation of $I_{\parallel}$ to $I_{\perp}$. The depolarisation ratio ρ is calculated as given in equation (2.28), where I_0 is the intensity of the baseline[10-13.]

$$\rho = (I - I_0)_{\perp} / (I - I_0)_{\parallel} \qquad (2.28)$$

Vibrational modes which are symmetric with respect to the symmetry elements can have depolarisation ratios values between 0 and 0.75, whereas for asymmetric vibrational modes the depolarisation ratio = 0.75. It is clear as to how useful the measurement of depolarisation ratios are, with respect to assigning symmetric and asymmetric vibrations in the Raman spectra of aqueous samples[13].

2.2.11. Molecular Symmetry

The symmetry of a molecule is a valuable tool to gain insight into molecular vibrations. For example, symmetric vibrations give rise to the intense Raman bands, whereas asymmetric modes are usually weak and sometimes unobservable. According to the rule of mutual exclusion, if a molecule has a centre of symmetry then Raman active vibrations are IR inactive, and *vice versa*. If there is no centre of symmetry then some (but not necessarily all) vibrations may be both Raman and IR active. Molecular symmetry can be classified in terms of symmetry operations, which are movements of the atoms which leave the molecule indistinguishable from the original. There are five symmetry operations.

1. The identity (E) is possessed by every molecule no matter how unsymmetrical it is, the corresponding operation being to leave the molecule unchanged. This operation represents a rotation of 360° and is the equivalent of doing nothing to the object.
2. An n-fold rotation axis (C_n) generates n symmetry operations corresponding to rotations through multiples of ($360°/n$), each of which leaves the resulting molecule indistinguishable from the original.
3. The reflection operation takes place with respect to a mirror plane, both of which are given the symbol σ. There are three types of mirror plane that need to be distinguished. A horizontal mirror plane σ_h is one which is perpendicular to the principal rotation axis. If the mirror plane contains the principal rotation axis it is called a vertical plane and is given the symbol σ_v. Vertical planes which bisect bond angles are called dihedral planes, and labelled σ_d.
4. The operation of inversion is carried out with respect to a centre of inversion (also referred to as centre of symmetry) and involves moving every point (x, y, and z) to the corresponding inverted position ($-x$,$-y$, and $-z$). Both the symmetry element and the symmetry operation are given the symbol i. Molecules which contain an inversion centre are described as being centrosymmetric.
5. The rotation reflection axis (S_n), is a two step operation. The molecule is rotated $360°/n$ and then reflected in a plane which is perpendicular to the axis, resulting in a configuration indistinguishable to that of the starting point.

A point group is a collection of symmetry elements. A simple method to classify point groups is illustrated in Fig. 2.5. Group theory can be used to determine the number of vibrational modes of the molecule, and the symmetry group to which these vibrational modes belong. For example, the *trans* structure of N, N'–dicyclohexylcarbodiimide exhibits C_s symmetry[23].

The character table for C_s symmetry is shown in Fig. 2.6.[10,11,18,22]

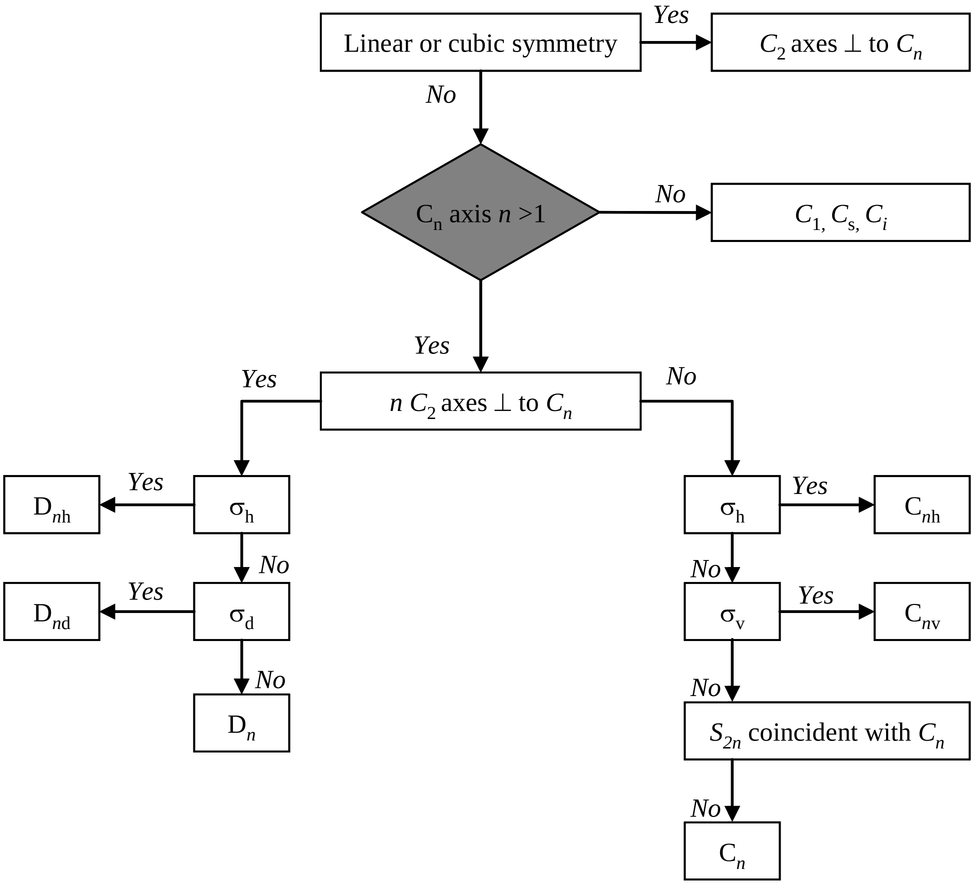

Figure 2.8. Flow chart showing the key decisions in point group assignment.

Symmetry elements I, σ(xy)				
Symmetry types and Characters				
$C_{1v}=C_{1h}=C_s$	I	$\sigma(xy)$		
A'	1	1	$T_x, T_y; R_z$	α_{xx}, α_{yy}, α_{zz}, α_{xy},
A''	1	-1	$T_z; R_x, R_y$	α_{yz} ,α_{xz},

Figure 2.9. Character table representing C_{1v}, C_{1h}, or C_s point group.

2.3. Computational Chemistry

Computational chemistry is defined as the application of mathematical and theoretical principles to the solution of chemical problems, and used as a research tool by chemists to help them investigate molecular structure, properties, kinetics and reactivity. Computational techniques allow chemists to study chemical phenomena by simulation *in* *silico* using computers rather than and/or complementary to examining compounds and/or reactions experimentally. Calculations can be used both to predict the results of experiments and to aid in the interpretation of existing results. The basis for most computational chemistry calculations is quantum mechanics.[24-26]

2.3.1. Molecular Mechanics

Molecular mechanics (MM) is a computational method that uses an extensive amount of experimentally derived parameterization. MM depends upon the laws of classical physics to predict the chemical properties of molecules and neglects the explicit treatment of electrons. Therefore, MM calculations cannot be used to understand electronic spectroscopy and photochemistry. MM models are system-dependent and do not predict energy values as absolute quantities; therefore they are generally useful for comparative studies. However, MM bridges the gap between quantum and continuum (classical) mechanics. In recent years, MM has evolved into techniques used extensively by chemists to quantitate the role that steric-strain plays in determining molecular structure, conformation, the energy differences between the conformations of a molecule, and binding interactions between molecules. Applications include modelling reactions and dissociation phenomenon on classical potential energy surfaces[27,28] and studies of crystal properties (*e.g.* density, packing, specific heats).[29,30]

2.3.2. Electronic Structure Methods

Electronic structure methods use the laws of quantum mechanics rather than classical physics for computations. The Schrödinger equation is the cornerstone of quantum mechanics. Solutions of the equation provides wave functions, ψ, which describe the behaviour of electrons in atoms and molecules, as well as the eigenvalues *viz* their associated energies, E:

$$H\Psi = E\Psi \qquad (2.29)$$

Because:

$$\frac{\partial^2\Psi}{\partial x^2}+\frac{\partial^2\Psi}{\partial y^2}+\frac{\partial^2\Psi}{\partial z^2}+\frac{8\pi^2 m}{h^2}(E-V)\Psi=0 \qquad (2.30)$$

There are two major classes of electronic structure methods.

2.3.3. *Ab Initio* Electronic Structure Methods

Ab initio molecular orbital methods are the most accurate and consistent because they provide the most rigorous mathematical approximation to an actual experimentally meaningful system. The term *ab initio* implies that the computations are based solely on the laws of quantum mechanics, the masses and charges of electrons and atomic nuclei, and the values of fundamental physical constants, such as the speed of light (c = 2.998×10^8 m/s) or Planck's constant (h = 6.626×10^{-34} Js^{-1}), and ideally contain no approximations other than mathematically tested ones. Molecular orbital methods solve Schrödinger's equation for defined chemical systems using a basis set of functions, which approximate the wave function(s) of the system. *Ab initio* molecular orbital calculations are approximated by model chemistry. The model chemistry includes the choice of method and basis set, the general structure and electronic state of the molecular system under study (*e.g.* charge and spin states), and the treatment of electron spin. Molecular properties can be assessed from a user-specified input (single-point energy calculation), or the molecule can be allowed to relax to a minimum energy configuration (geometry optimization).[24,26]

2.3.4. Semi-Empirical Methods

Semi-empirical methods are used to study larger molecules. In general, they are a combination of *ab initio* methods together with data from empirical studies, *e.g.* spectroscopic measurements and heats of formation. The results obtained are typically less accurate than that of *ab initio* methods, but they are generated more quickly and can be applied to larger molecules. Semi-empirical methods increase the speed of computation by using approximations of *ab initio* techniques (*e.g.* by limiting choices of molecular orbitals or considering only valence electrons) which have been fitted to experimental data (for example structures and formation energies of organic molecules).[30] Semi-empirical methods have been designed for typical organic or biological systems and tend to be inaccurate for problems involving hydrogen-bonding, chemical transitions or nitrated compounds which generally lack parameterization. Several semi-empirical methods are available and appear in commercially available computational chemistry software packages such as HyperChem.[31]

2.3.5. Density Functional Methods

Density functional theory (DFT) has emerged during the past few decades as a powerful method for the simulation of chemical systems. The underlying concept of DFT is based on the assumption that the energy of an electronic system can be defined in terms of its electron probability density, ρ. For a system comprising n electrons, $\rho(r)$ represents the total electron density at a particular point in space (r). According to DFT, the electronic energy (E) is regarded as a function of the electron density $E(\rho)$ in the same sense that a given function [$\rho(r)$] corresponds to a single energy, *i.e.*, a one-to-one correspondence between the electron density of a system and its energy exists. While the complexity of the wave function increases with the number of electrons, the electron density maintains the same number of variables independently of the system size.

In 1965 Kohn and Sham[32] developed a formalism, with the introduction of atomic orbitals, which is the basis of the current applications of DFT methods. This is a practical way to solve the Hohenberg-Kohn theorem[33] for a set of interacting electrons from a virtual system of non-interacting electrons with an overall ground-state density equal to the density of a real chemical system. The main problem behind initial DFT formalisms was the difficulty in representing the kinetic energy of the system. The major principle of the Kohn-Sham approach is that the kinetic energy functional of a system can be split into two parts; one part that can be calculated exactly, considering electrons as non-interacting particles, and another small correction term accounting for interactions between electrons.

Following the Kohn-Sham formalism the electronic energy of the ground state of a system comprising n electrons and N nuclei within an orbital formulation can be written as:

$$E[\rho] = -\frac{1}{2}\sum_{i-1}^{n}\int \psi_{i}^{*}(r_i)\nabla_i^2\psi_i(r_1)dr_1 - \sum_{X=1}^{N}\int \frac{Z_X}{r_{Xi}} - \rho(r_1)dr_1 + \frac{1}{2}\iint \frac{\rho(r_1)\rho(r_2)}{r_{12}}dr_1 dr_2 + E^{XC}[\rho] \quad (2.31)$$

In equation 2.31, ψ_i (1,2,…,n) are the Kohn-Sham orbitals, the first term represents the kinetic energy of the non-interacting electrons, the second term accounts for the nuclear-electron interactions, and the third term corresponds to the Coulombic repulsions between the total charge distributions at r_1 and r_2. Finally, the fourth and last term, known as the exchange-correlation term, represents the correction to the kinetic energy arising from the interacting nature of the electrons, and all non-classic corrections to the electron-electron repulsion energy. The ground state electron density $\rho(r)$ at a location r can be written as a set of one-electron orbitals (the Kohn-Sham orbitals), given by:

$$\rho(r) = \sum_{i=1}^{n} \psi_i(r)^2 \qquad (2.32)$$

The Kohn-Sham orbitals are determined by solving the Kohn-Sham equations. These can be derived by applying variational principles to the electronic energy $E(\rho)$, with the charge density given by equation 2.32:

$$\hat{h}_i \psi_i(r_1) = \varepsilon_i \psi_i(r_1) \qquad (2.33)$$

In equation 2.33, $\hat{h}_i$ represents the Kohn-Sham Hamiltonian and ε_i is the associated Kohn-Sham orbital energy. The Kohn-Sham Hamiltonian can be written as:

$$\hat{h}_i = -\frac{1}{2}\nabla_1{}^2 - \sum_{X=1}^{N} \frac{Z_X}{r_{Xi}} + \int \frac{\rho(r_2)}{r_{12}} dr_2 + V^{XC}(r_1) \qquad (2.34)$$

In equation 2.34, V^{XC} is the functional derivative of the exchange-correlation energy, given by:

$$V^{XC}[\rho] = \frac{\delta E^{XC}[\rho]}{\delta_\rho} \qquad (2.35)$$

Once E^{XC} is known, V^{XC} can be readily obtained. The importance of the Kohn-Sham orbitals is that they allow the electron density to be calculated, using equation 2.35. The resolution of the Kohn-Sham equation is processed in a self-consistent fashion, starting from a tentative charge density which, for a molecular system, can be derived from the superposition of the atomic densities of the constituent atoms. An approximate form for the functional that describes the dependence of E^{XC} on the electron density is then used to calculate V^{XC}. The entire process is repeated until the density and the exchange-correlation energy have satisfied a certain convergence. The electronic energy can then be calculated using equation 2.34.

Kohn-Sham orbitals are normally expressed in terms of a set of basis functions. Therefore, the solution of Kohn-Sham equations corresponds to determining the coefficients in a linear combination of the basis functions. The exchange-correlation energy is generally divided into two separate terms: an exchange term (E^X) and a correlation term (E^C). The exchange term is associated with interactions between electrons of the same spin, whereas the correlation term represents interactions between electrons of opposite spin. These two terms are themselves functionals of the electron density and are known as the exchange functional and the correlation functional, respectively. These functionals can be of two distinct types: local functionals depending on the electron density only; and gradient-corrected functionals which depend on both ρ and its gradient, $\Delta\rho$.

DFT calculations fall into three general categories:

- local density approximations (LDA),
- generalized gradient approximations (GGA), and
- hybrid density functional methods (H-GGA).

2.3.5.1. *Local Density Approximations*

The local density (LDA) is the simplest approach corresponding to the exchange-correlation functional. In general, LDA assumes that the exchange-correlation energy at any point in space is a function of the electron density at that point in space, and can be approximated by the electron density of a homogeneous electron gas of the same density. The first LDA for the exchange-correlation energy was proposed by Dirac in 1930[34] and was used together with the Thomas-Fermi model [35, 36]

$$E_{LDA}^{X.Dirac}[\rho] = -C_X \int \rho^{4/3} dr \qquad (2.36)$$

where the constant C_X is given by:

$$C_X = -\frac{3}{4} \bullet \left(\frac{3}{\pi}\right)^{1/3} \qquad (2.37)$$

Significant improvements were obtained with the Thomas-Fermi-Dirac-Weizsacker model, [37] which included gradient corrections to the Thomas-Fermi *K.E.* functional. The local spin density approximation (LSDA), initially proposed by Slater,[28] represents a more general application of LDA solving several of the conceptual problems inherent to the early LDA approaches for systems that are subject to an external magnetic field;

systems that are polarized and where relativistic effects have to be accounted for are important. Within the LSDA approach, the exchange functional is given by:

$$E^{X}_{LXDA}[\rho] = -2^{1/3} C_X \int \left(\rho_\alpha{}^{4/3} + \rho_\beta{}^{4/3} \right) dr \qquad (2.38)$$

In equation 2.38 α and β represent spin up and spin down densities, respectively. For closed shell systems α and β are equal, and LSDA becomes virtual identical to LDA.

2.3.5.2. *Generalized Gradient Approximations (GGA)*

Real molecular systems are very different from a homogeneous electron gas. In fact any chemical system is spatially inhomogeneous due to varying spatial density $\rho(r)$. The development of GGAs take this effect into account, by making the exchange and correlation energies dependent not only on ρ, but also on the gradient of the density, $\Delta\rho$. GGA methods signify a noteworthy improvement over local methods and give better values of atomization energies, structural energy differences, and energy barriers. However the accuracy of GGA methods is still not enough for a correct description of many chemical aspects of molecule.

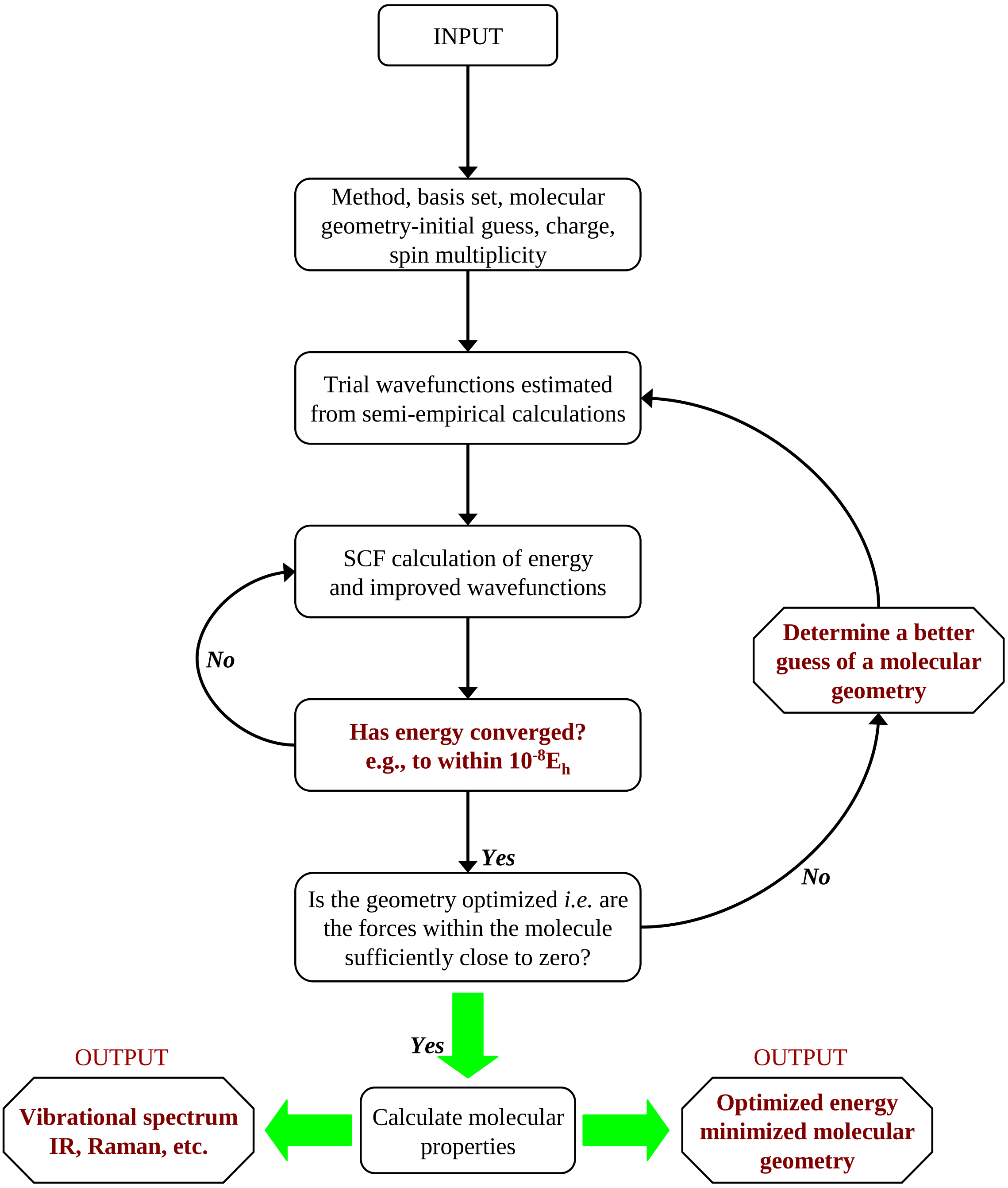

Figure 2.10. Flowchart illustrating the steps involved in quantum chemical calculations of molecular structures and properties.[40]

Although GGA methods give reliable results for covalent, ionic, metallic and hydrogen bonds, they typically fail for van der Waals interactions and bond dissociation. In the case of the solid state, GGA functionals do not yield significantly better results than LDA, nor in the calculation of the ionization potentials and electron affinities.

2.3.5.3. *Hybrid Density Functional Methods (H-GGA)*

H-GGA methods combine the exchange correlation of a conventional GGA method with a percentage of Hartree-Fock (HF), exchange. A certain degree of empiricism is used in optimizing the weight factor for each component and the functionals that are mixed. Hybrid functionals have allowed a significant improvement over GGAs for many molecular properties. For this reason they have become a very popular choice in quantum chemistry and are now widely used. Examples of hybrid functionals include B3LYP, and B3P86 *etc*. However, B3LYP is by far the most popular density functional in chemistry, representing 80% of the total usage of density functionals in the literature, in the period 1990-2010.[39]

2.3.6. Basis Sets

In quantum chemical calculations, the term "basis set" is the mathematical description of the electronic orbitals within a system which in turn combine to approximate the total electronic wave functions used to perform theoretical calculation. However, according to the quantum mechanical treatment, electrons have a finite probability of existing anywhere in space. Standard basis sets for electronic structure calculations use linear combinations of Gaussian functions to form the orbitals. Basis sets can be classified by the number and type of basis functions that they contain.

2.3.7. Single-Point Energy Calculation

Single point energy gives a prediction of the energy of a molecule with a specific geometry. This is usually followed by a Mulliken population analysis which is used to estimate the charge distribution. Electrostatic moments are also calculated, which then allow dipole moments to be calculated. A single-point energy calculation can be performed at any level of theory, with small or large basis sets.

2.3.8. Potential Energy Surface (PES)

A potential energy surface represents the way in which the energy of a molecular system varies over a set of variables, *e.g.* with small changes in its structure. In actual practice, a PES is a mathematical relationship linking molecular structure and the resultant potential energy.

For a diatomic molecule, it is a 2D plot with the inter-nuclear separation on the x axis (the only way that the structure of such a molecule can vary), and the energy at that bond distance on the *y* axis, producing a curve. For larger systems the surface has many dimensions, as molecules have different degrees of freedom.

2.3.9. Geometry Optimization

Optimization of molecular geometry is a first step in any quantum chemical calculation. This is mostly done on an isolated molecule, assumed to be in the gas phase, and not interacting with any other molecules. Geometry optimization is performed to locate the lowest energy molecular structure in close proximity to the specified starting structure.

A geometry optimization will adjust the atomic arrangements in a molecule until an energy minimum is reached. This is the lowest position on the potential energy surface. It is generally a reasonable practice to use experimental data, whenever possible, as a starting point for geometry optimization. In the absence of experimental data construction of models is based on intuitively reasonable values for bond distances, inter-bond angles and dihedral angles. Figure 2.10 shows a typical flow chart explaining the geometry optimization process[40].

2.3.10. Frequency Calculations

Vibrational spectra of molecules in their ground and excited states can be computed by employing the program Gaussian. However, because of the nature of the computations involved, frequency calculations are valid only at stationary points on the potential energy surface, for this reason, it is necessary to run a geometry optimization prior to doing a frequency calculation. In addition to predicting the frequencies and intensities of spectra, the program can also describe the displacements a system undergoes in its normal modes.

Molecular frequencies depend on the second derivative of energy with respect to the position of nuclei. Analytic second derivatives are provided for the Hartree-Fock, density functional theory (B3LYP), Møller-Plesset (MP2) and CASSCF theoretical procedures. An optimized energy is used as input for the frequency calculation. The frequency calculations should be performed using the same theoretical model and basis set as the one that was used to obtain the optimised geometry of the molecule.[24-26, 41-44]

2.4. References

[1] A.S. Raymond and W.J. Jewett, *Physics for Scientists and Engineers*, 6th Ed., Thomson Brooks/Cole (2004).

[2] P. Tipler, W.H. Freeman, *Physics for Scientists and Engineers: Electricity, Magnetism, Light, and Elementary Modern Physics*, 5th Ed., Thomson Brooks/Cole (2004).

[3] W.W. Coblentz, *Investigation of Infrared Spectra*, Carnegie, Washington, 1905, reprinted 1962.

[4] A. Smeckel, *Naturewissenschafften*, 1923, **43**, 873.

[5] C.V. Raman, K.S. Krishnan, *Nature*, 1928, **121**, 501.

[6] J.M. Brown, *Molecular Spectroscopy*, Oxford, Oxford University Press, 2003.

[7] L.M. Harwood, T. D. W. Claridge, *Introduction to Organic Spectroscopy*, Oxford, Oxford University Press, 1997.

[8] M.J. Hollas, *Modern Spectroscopy*, 2nd Ed, Chichester, Wiley, 1992.

[9] C.N. Banwell, E.M. McCash, *Fundamentals of Molecular Spectroscopy*, 4th Ed, London, McGraw-Hill, (1994).

[10] E. Bright Wilson Jr., J.C. Decius, P.C. Cross, *Molecular Vibrations. The Theory of Infrared and Raman Vibrational Spectra*, New York, Dover, 1980.

[11] J.R. Ferraro, K. Nakamoto, *Introductory Raman Spectroscopy*, San Diego, Academic Press, 1997.

[12] N.B. Colthup, L.H. Daly and S.E. Wiberley, *Introduction to Infrared and Raman Spectroscopy*, 3rd Ed, Academic Press, (1999).

[13] J.B. Lambert, H.F. Shurvell, D.A. Lightner, R.G. Cooks, *Organic Structural Spectroscopy*, London, Prentice-Hall, 1998.

[14] P.W. Atkins, R.S. Friedman, *Molecular Quantum Mechanics*, 3rd ed., Oxford University Press Inc., New York 1997.

[15] I. Lewis, H. Edwards, *Handbook of Raman Spectroscopy: from the research laboratory to the process*, Marcel Dekker, NY & Basel 2001.

[16] C.Y. Huang, G. Balakrishnan, T.G. Spiro, J. *Raman Spectr*., 37, 1-3, 2006, 277.

[17] B. Schrader and D.S. Moore, *Pure & Appl. Chem*., **69**, 1997, 1451.

[18] E. Smith and G. Dent, *Modern Raman Spectroscopy*, John Wiley & Sons, Chichester , (2005).

[19] J.R. Nestor and E.R. Lippincott, *J. Raman. Spectrosc*., 1973, **1**, 305-318.

[20] A. Fadini, F.M. Schnepel, *Vibrational Spectroscopy Methods and Applications*, Ellis Horwood LTD. John Wiley & Sons, New York, 1989.

[21] G. Herzberg, *Infra-red and Raman spectra of polyatomic molecules*, NewYork; Van Nostrand, 1945.

[22] G.W. King, *Spectroscopy and Molecular Structure*, Holt, Rinehart and Winston, New York, 1964.

[23] K.C. Molloy, *Group Theory for Chemists*, Harwood, (2004).

[24] J.B. Foresman, C. Frisch, *Exploring Chemistry with Electronic Structure Methods*, 2nd ed., Gaussian Inc., Pittsburgh, PA 1996.

[25] S. Bell, B.Z. Chowdhry, R. Withnall, T.J. Dines, *J. Chem. Ed*., 2007, **84**, 1364.

[26] J.B. Foresman, *Ab initio techniques in chemistry: Interpretation and visualization*, ACS Books, Washington, D.C., 1996.

[27] C.C. Chambers, D.L. Thompson, *J. Phys. Chem*., 1995, **99**, 15881.

[28] D.V. Shalashilin, D.L. Thompson, *J. Phys. Chem*. A 1997, **101**, 961.

[29] K. Yohno, K. Ueda, A. Imamura, *J. Phys. Chem*., 1996, **100**, **4701**.

[30] D.C. Sorescu, B.M. Rice, D.L. Thompson, *J. Phys.Chem. A* 1998, **102**, 8386 & 948.

[31] HyperChem 5.0 user manuals, Hypercube, Inc., Gainesville FL, 1996.

[32] W. Kohn, L.J. Sham, *Phys. Rev*., 1965, **140**, A1133.

[33] P. Hohenburg, W. Kohn, *Phys. Rev*., 1964, **136**, B864.

[34] P.A.M. Dirac, *Proc. Camb. Phil. Soc*., 1930, **26**, 376.

[35] E. Fermi, *Phys*. 1928; **48**: 73.

[36] L.H. Thomas, *Proc. Camb. Phil. Soc*., 1927; **33**: 542.

[37] R.G. Parr, Y. Weitao, Density *Functional Theory of Atoms and Molecules*, Oxford University Press, US, 1989: 333. [28]

[38] J.C. Slater, *Phys. Rev*., 1951, **81**, 385.

[39] S.F. Sousa, P.A. Fernandes, M.J. Ramos, *J. Phys. Chem*., 2007, **111**, 10439.

[40] S. Bell, B.Z. Chowdhry, T.J. Dines, R. Withnall, *J. Chem. Ed*. 2006.

[41] D.B. Cook, *Handbook of Computational Quantum Chemistry*, New York: Oxford University Press 1998.

[42] I. Levine, *Quantum Chemistry*, Chapter 14. Allyn and Bacon Inc., Boston 1970.

[43] J. Simons, J. Nichols, *Quantum Mechanics in Chemistry*, Oxford University Press, Oxford, UK 1997.

[44] P.W. Atkins, R.S. Friedman, *Molecular Quantum Mechanics*, 3rd ed., Oxford University Press Inc., New York 1997.

3. Experimental and Instrumentation

3.1. Chemical Reagents

The chemical reagents used in the experimental studies are listed in Table 3.1. Unless otherwise stated all chemical reagents were analar grade, purchased from Sigma-Aldrich (Dorset, UK) and used as received.

Table 3.1. Chemical reagents.

Abbreviated Chemical Name	Chemical Formula	Mol. Wt	Purity (%)
Urazole	$C_2H_3N_3O_2$	101.07	99.98
4-methylurazole	$C_3H_5N_3O_2$	115.09	99.98
N,N'dicyclohexylcarbodiimide (DCC)	$C_6H_{11}N{=}C{=}NC_6H_{11}$	206.33	99.0
Potassium persulphate	$K_2S_2O_8$	270.32	99.0
2,2′-azobis(2methyl propionamidine) dihydrochloride	$C_8H_{18}N_6$ 2HCl	271.19	99.0
N, N′-Methylenebisacrylamide	$C_7H_{10}N_2O_2$	154.17	99.0
N-isopropylacrylamide (NIPAM)	$C_6H_{11}NO$	113.16	99.0
4-Vinylpyridine	C_7H_7N	105.14	99.0
Chloroform	$CHCl_3$	119.38	99.5
Chloroform-d	$CHCl_3$	120.38	99.5
Deuterium oxide	D_2O	20.03	99.9
Phosphorous pentoxide	P_2O_5	141.94	98.0
Sodium hydroxide	NaOH	39.99	99.0
Sodium deuteroxide	NaOD	41.00	99.0
Hydrochloric acid	HCl	36.46	99.0

Where required, in-house produced double-deionised water was used.

3.1.1. Deuteration

Deuterated isotopomers and derivatives were prepared by dissolving ~10 mg of sample in 10 mL of deuterium oxide (D_2O). Solid, dry material was recovered by placing frozen samples (-20°C) into an Edwards freeze drying apparatus (Edwards 8, dual stage vacuum pump). Samples were left 'on the pump' for ~ 4 hours or until completely dry. This deuteration process was repeated at least an additional two times, in order to improve the percentage yield of the deuterated product.

Urazole and 4-methylurazole were obtained from Aldrich (Dorset, UK) and used without further purification. Spectroscopic grade deuterium oxide (99.98 atom %) were obtained from Sigma-Aldrich Ltd (Poole, Dorset, UK). *N*-deuterated isotopomers were prepared from solutions in D_2O and the powdered isotopomers were recovered using a Birchover freeze-drying apparatus. The pH of the samples in the aqueous state was varied using μL quantities of 1.0 mol dm^{-3} HCl or NaOH. This was measured directly using a digital pH meter (Jenway, 3305).

Anion sodium salts (non-deuterated and deuterated) were synthesized using 0.1 mol dm^{-3} NaOH or NaOD followed by rotary evaporator drying. These samples were extremely hygroscopic and were stored, prior to examination by Raman and FT-IR, in a dessicator containing P_2O_5.

3.1.2. Microgel Preparations

Microgel samples poly(NIPAM) and poly(4-VP) as well as poly(NIPAM/4-VP) microgel dispersions (the last ranging in percentage starting composition of 4-VP of 7.5 – 90%, w/w, *relative* to the NIPAM monomer) were prepared (by surfactant-free emulsion polymerisation and purified (by filtration followed by extensive dialysis, centrifugation and re-dispersion) as described previously[1]. Microgels were synthesized using fixed concentrations of initiator (10 wt% $K_2S_2O_8$ for the synthesis of poly(NIPAM); 10 wt% 2, 2′-azobis(2-methylpropionamidine) dihydrochloride for the synthesis of poly(NIPAM/4-VP) and cross-linker (10 wt% of N, N′-methylenebisacrylamide (BA)) for all microgels. Dry weight (gravimetric) analysis of the solid content (wt %) of the microgels was undertaken and typical reaction yields were calculated to be ~95 %. In addition, the microgel samples synthesized were characterized, as previously described,[1] by TEM and PCS. The aqueous microgel stock dispersions were stored in the fridge at 4°C, until they were required. From these, freeze-dried samples were prepared in the normal (standard) manner using an Edwards freeze-dryer.

3.2. Vibrational Spectroscopy

3.2.1. Dispersive-Raman Spectroscopy

Raman spectra of all samples were carried using a LabRam Raman spectrometer (Horiba Jobin Yvon Ltd, Figures 3.1, 3.2, and 3.3). The spectrometer is equipped with an 1800 groove/mm holographic grating, a hololographic notch filter, a Spectrum One Peltier-cooled CCD (MPP1 chip) for detection and an Olympus BX40 microscope. A helium-neon laser provided exciting, monochromatic radiation of wavelength (λ_o) at 632.8 nm and an argon-ion laser at 514.5 nm. In both cases the unattenuated power at the sample was 8 mW. Raman measurements largely consisted of acquiring multiple spectral windows in the range 50-4000 cm^{-1} (Stokes shifts). The Raman instrument was calibrated using the ν_1 line of silicon at 520.7 cm^{-1}. The centring of the silicon line was checked by using the frequencies of the principal lines of a neon lamp.

Figure 3.1. Photograph of the ISA laser Raman spectrometer system

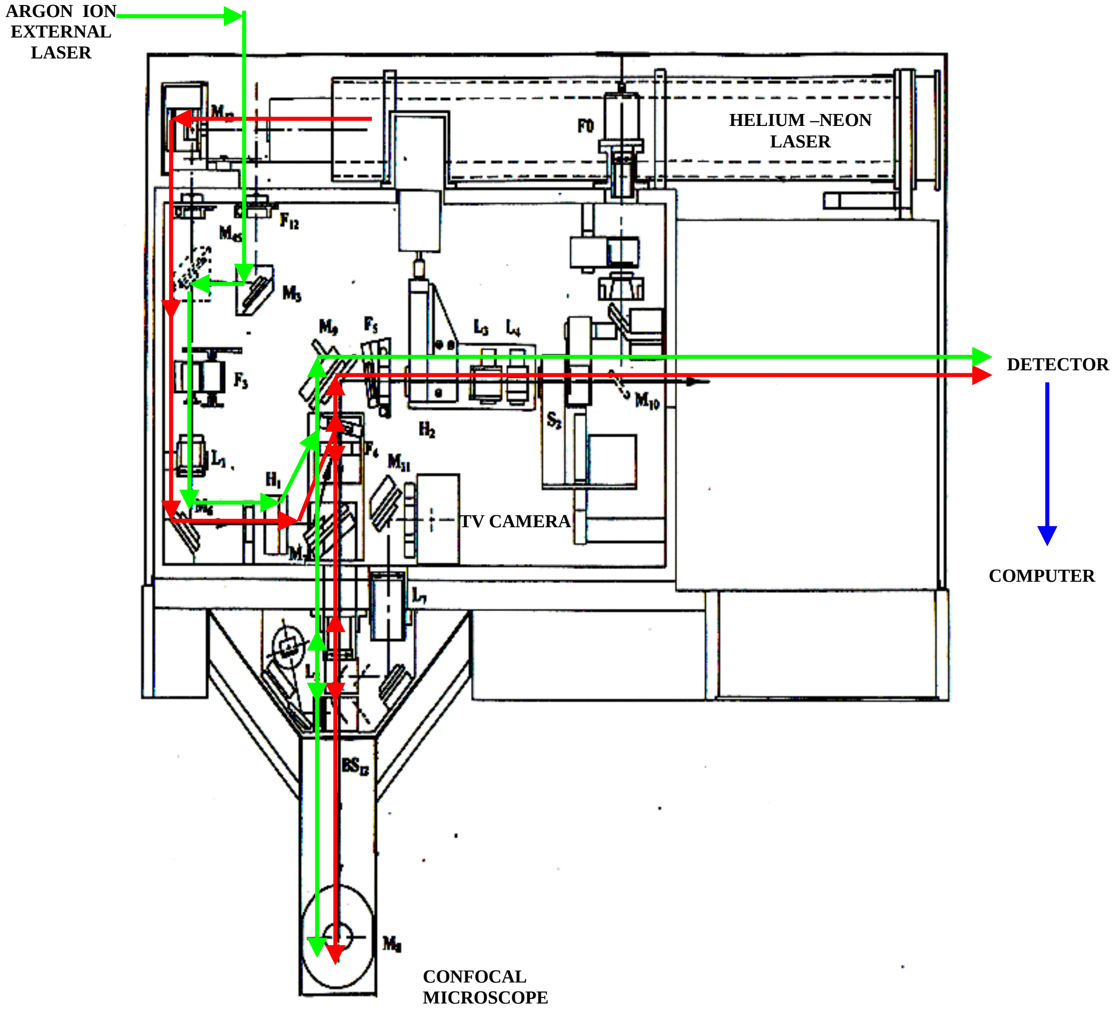

Figure 3.2. Optical arrangement of the internal components of the ISA laser Raman spectrometer employed in all experiments.

The laser paths are highlighted in red (λ_o = 632.8 nm) and green (λ_o = 514.5 nm).

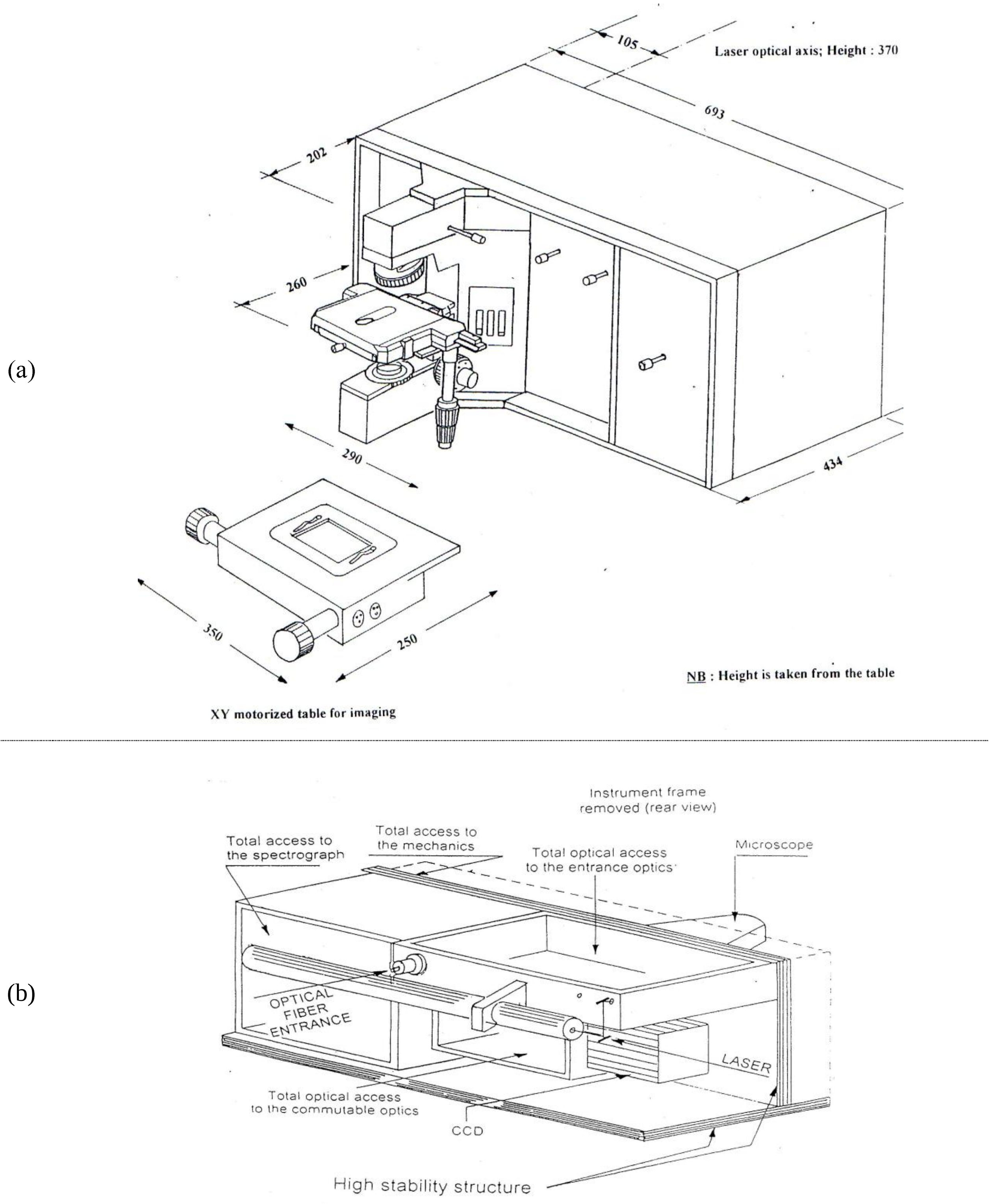

Figure 3.3. Schematic diagram of the ISA laser Raman spectrometer (a) front view, (b) rear view

Figure 3.2 illustrates that the laser beam is directed by two mirrors, M_{12} in order to pass through two irises, located before the interference filter F_{12} (used to filter out laser plasma lines) and the laser lens L_1 (focuses the laser onto the pinhole H_1). The pinhole is used as a reference for alignment and is conjugated with the spot on the sample. F_3 represents the filter wheel comprises of six different filters with different optical densities to reduce the power of the incident laser beam, for instance when laser causes thermal degradation. The laser beam from H_1 is then reflected by the mirror M_7, onto the angle-tuned holographic notch filter (F_4), which enables the laser beam to be reflected towards the sample. A confocal microscope objective is used to focus the laser onto the sample. A 180° back scattering configuration allows to the collection of Rayleigh and Raman scattered radiation, which follows the same path back to the notch filter. The notch filter filters the Rayleigh radiation and allows only Raman radiation to pass through. The lens L_2 directs the laser spot onto the confocal hole H_2. The lenses L_3 and L_4 (polarisation analysers and scramblers may be placed between L_3 and L_4) image the confocal hole onto entrance slit S_2. The image of the hole is reduced by a factor of five on the entrance slit. A shutter is installed after the slit, enabling the Raman scattered radiation to enter the spectrometer. A beam splitter BS_{12} can be placed in the optical beam from the sample, to allow observation on a TV camera, which can be used for instance, to facilitate the focusing of the sample using the confocal microscope. The spectrometer is equipped with a motorised holographic grating (1800 groove/mm), which disperses the Raman signal to the CCD detector. The spectral resolution depends on the number of grooves per millimetre, the larger the number of grooves/mm, the better the spectral resolution.

The spectrum One CCD detector is a solid state photodetector array made of silicon[3]. The CCD area is divided into a two dimensional matrix of pixels. When illuminated with light, by opening the shutter, each pixel gains a charge from the photoelectric effect. The charges of the neighbouring pixels are kept separated by a grid of electrodes that confine the charges. After data acquisition when shutter is closed, the charges of the pixels are analysed row by row, to the edge of the chip into a read out register, after processing signal is converted into the digital data for software manipulation. The CCD is equipped with a Peltier cooler to reduce the dark noise and hence improve the *S/N* ratio[2,3]. The detector is cooled to -37°C.

3.2.1.1. *Solid State Raman Spectra*

Raman spectra of solid state (powdered) urazole/ methyl urazole samples which were normally solid at room temperature were collected on a microscope slide using a microscope objective of ×50 magnification to focus the helium-neon laser beam. If there appeared to be a problem from polarisation effects of the solid state sample, the spectra were re-collected using a ×10 microscope objective to focus the laser beam. Ten scans each of 10 s were collected.

N,N'dicyclohexylcarboximide (DCC) solid state samples were collected using a helium–neon laser and x100 magnification, but with a 10% neutral density filter so as to reduce the laser power to 0.8 mW to minimise thermal degradation of sample. All Raman measurements involved acquisition of multiple spectral windows in the range 100-3500 cm^{-1} (Stokes shifts only). Polarization studies involved insertion of a plane polarizing analyzer in the path of the scattered radiation, enabling the separate measurement of Raman scattering with polarization either parallel or perpendicular to the electric vector of the incident radiation.

3.2.1.2. *DCC Melting Studies – Solid–Liquid Phase Transition*

Raman experiments were also carried out at temperatures in the range 20-60 °C (at 2 °C intervals throughout the solid-liquid phase transition and at 5 °C intervals elsewhere), using a Linkam temperature controlled cell, with a microscope objective of ×50 magnification.

3.2.1.3. *Solution State Raman Spectra*

Solution phase spectra were acquired using a 1 cm^{-1} path length quartz cuvettes where the back scattered radiation was collimated by a 40 mm focal length macro lens. A back-scattering (180° excitation and collection) geometry was used in all experiments.

3.2.1.3.1. Solution Concentrations

Solution Raman spectra of urazole and 4-methylurazole, *N*-deuterated derivatives and their mono-anions; were acquired at concentrations of 60 mg mL^{-1}.

Solution Raman spectra of DCC in $CHCl_3$ and $CDCl_3$ were acquired at concentrations of 80 mg mL^{-1}. Solution spectra consisted of 20 scans, each of 30 s duration.

3.2.1.4. *Raman Spectroscopy of Urazole and 4-Methylurazole*

The Raman spectra of urazoles and derivatives, including their *N*-deuterated derivatives, were investigated in both solid and solution states. Subsequently, the Raman spectra of the mono-anions of both, in aqueous solution at high pH and in the solid state were investigated.

3.2.1.5. *Raman Studies of Microgel Samples*

A helium-neon laser provided exciting radiation of 632.8 nm and a laser power of 8 mW at the sample. Raman spectra of freeze-dried samples, placed on a microscope slide, were collected by using a 180º back-scattering geometry. The Raman instrument was calibrated using the ν_1 line of silicon at 520.7 cm^{-1}. The centring of the silicon line and wavenumber calibration was checked by using the frequencies of the principal lines of a neon lamp. Relative intensities of selected vibrational bands, of primary analytical interest, were estimated (from their band areas) using the software provided by the Raman instrument manufacturer.

3.2.2. FT-Infrared Spectroscopy Instrumentation

Figure 3.4 displays the internal components of a typical Perkin-Elmer FT infrared spectrometer[4,5]. The excitation source, an infrared globar source, (1) splits the light into parallel beam, which is directed towards the interferometer. The interferometer comprises of a beam splitter (1) and two mirrors (one of them is fixed, while the second is moving mirror (2)). The former (1) is a plate of potassium bromide (KBr), which is angled and transparent enough to allow 50% of the radiation falling on it to be reflected and 50% to pass straight through. This arrangement allows the half of the infrared beam to fall onto the fixed mirror and other half falls onto a moving mirror. The moving mirror is the integral part of the interferometer and is used to produce an interferogram for the infrared beam. The incident radiation reflected from the moving mirror passes through another KBr window (7), and focussed onto the sample (6). An interferogram is then collected and passed to the detector (8). The detector is a photoconductivity cell, which is made out of deuterated triglycine sulphate (DTGS). The interferogram can be converted into the original frequencies emitted by the source by computing the Fourier transform. For the sample positioning, a pre-aligned laser (9) determines the path of the infrared beam. All the internal optics are encased in a hard plastic cover (10, 4) to protect from the ingress of moisture, dust, and other vapours. The optical chamber is kept dry by molecular desiccant (11). Owing to the single beam mode of the instrument, it is important to run a background spectrum with the sample compartment (5) empty to subtract from the infrared spectrum of the sample. To further limit errors in the background subtraction due to moisture and CO_2 in the atmospheric air, dry nitrogen can be purged in the sample compartment.

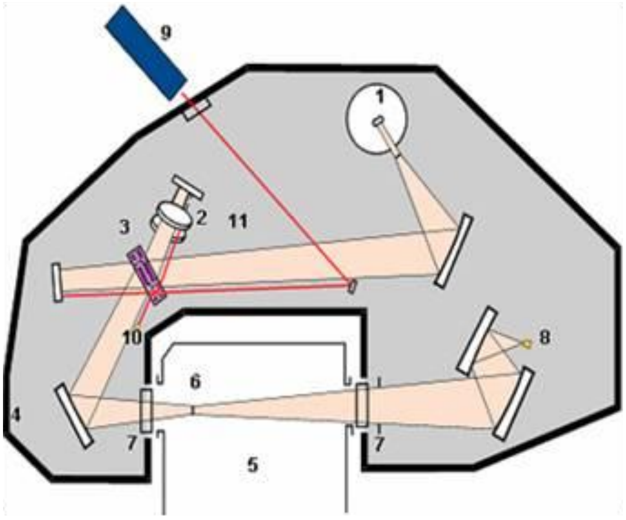

Figure 3.4. Schematic of the internal components of a typical Perkin-Elmer FT infrared spectrometer.

3.2.2.1. *Solid State FT-Infrared Spectroscopy*

Thin hydraulically pressed discs; containing approximately 1 mg of each sample, dispersed in 100 mg of KBr were used for the FT-IR measurements. The FT infrared solid state spectra of urazole, 4-methyl urazoles and DCC were recorded on a Perkin Elmer Paragon 1000 FT-IR spectrophotometer in the 450–4000 cm^{-1} range, recorded at room temperature. Collection Parameters are shown in Table 3.2. In order to minimize the effects of traces of atmospheric water vapour and CO_2 the sample compartment of the spectrometer was purged with dry N_2. This also facilitated a simpler background subtraction.

Table 3.2. Collection parameters.

Reagent	**No. of scans**	**Spectral resolution – cm^{-1}**
Urazole/4-methylurazole	40	1
DCC (FT-IR)	30	2
DCC (ATR-IR)	16	2

3.2.2.2. *Solution FT-Infrared Spectroscopy*

FT-IR measurements of ‘urazoles’ in solution and DCC (in $CDCl_3$ /$CDCl_3$) were conducted using a Perkin Elmer 1710 FT-IR and 1000 FTIR respectively. Samples were placed in solution cells, with calcium fluoride or zinc selenide windows, and the spectra recorded within the range 450-4000 cm^{-1}.

3.2.2.3. *The ATR Spectra of DCC*

The ATR-IR spectrum of a powder sample of DCC was measured using a Thermo Nicolet Nexus FTIR spectrometer equipped with an MCT liquid nitrogen-cooled detector, KBr beam splitter and a 45° ZnSe ATR plate. Wavenumber resolution was 2 cm^{-1} and 16 scans were accumulated, in the range 530-4000 cm^{-1}. A background spectrum was measured on the ATR plate without a sample (signal intensity I_0), then the sample spectrum was measured using a thin layer of solid DCC on the ATR plate (signal intensity I). The spectrum was plotted as the signal intensity ratio $-\log(I/I_0)$.

3.3. Density Functional Theory (DFT) Calculations

Initial DFT calculations on urazole, methyl urazole, *N*-deuterated derivatives of the mono-anions and DCC were performed using the *Gaussian03* program[6]. These calculations were undertaken using the hybrid SCF-DFT method B3-LYP, which incorporates Becke’s three parameter hybrid functional[7] and the Lee, Yang and Parr correlation functional[8], in conjunction with the cc-pVTZ basis set[9].

3.3.1. Computational Methods – Normal Coordinate Analysis (NCA)[10]

Where known, the geometry obtained from the molecules crystal structures, or structures of closely related molecules, was used as the initial estimate for optimisation.

The vibrational spectra were calculated at the optimised geometry[11,12]. For computation of the potential energy distributions (PEDs) associated with the vibrational modes, the Cartesian force (c.f) constants obtained from the *Gaussian 03* output were converted to force constants expressed in terms of internal coordinates. Scaling factors may be applied to the force constants before input to a normal coordinate analysis program derived from those of Schachtsneider[13]. IR and Raman intensities were computed from the dipole and polarizability derivatives of the *Gaussian 03* output. Since the dipole and polarizability derivatives are expressed in terms of Cartesian coordinates they were transformed to internal coordinates and subsequently to normal coordinates[14]. The simulated IR spectrum was obtained by convolution of computed band intensities with a Lorentzian lineshape function (f.w.h.m. = 10 cm^{-1}).

Scaling is used to match the calculated harmonic vibrations with the observed vibrations, which are anharmonic. Scaling of force constants, expressed in internal coordinates, was applied according to the formula $f_{ij}^{scaled} = f_{ij}^{calc}\sqrt{s_i s_j}$ where s_i and s_j are scale factors relating to internal coordinates *i* and *j*, respectively, following the Pulay SQM-FF method[14]. In the present work scaling was applied to the computed vibrational spectrum of DCC, but not for urazole, 4-methylurazole and their anions

3.3.2. Further Computational Methodology for Urazole and 4-Methylurazole and Derivatives

Calculations involving implicit and explicit solvation with hydrogen bonded water molecules were carried out using 'Polarizable Continuum Models' (PCM) and are fully described in the further experimental descriptions,.

3.3.3. Further Computational Details for DCC

DFT calculations were performed as described before (3.3., 3.3.1.), using the *Gaussian03* program[15]. In the absence of crystal structure data, models and spectra were calculated with structures with C_2 and C_i symmetry, respectively, and axial or equatorial cyclohexyl rings. The geometries of these four structures were optimised again using the hybrid SCF-DFT method B3-LYP, which incorporates Becke's three parameter hybrid functional[7] and the Lee, Yang and Parr correlation functional[8], in conjunction with the cc-pVTZ basis set[9]. The computational procedures and calculations are fully described in further experimental descriptions.

3.4. References

[1] V.T. Pinkrah, M.J. Snowden, J.C. Mitchell, B.Z. Chowdhry, J. Siedel, G. R. Fern, *Langmuir*, 2003, **19**, 585.

[2] Labram User Manual, ISA, Dilor, Jobin Yvon, France, 1998.

[3] CCD Detection User Manual, Spectrum One, 1996.

[4] Text, courtesy of Perkin-Elmer, UK.

[5] Photo and diagram courtesy of Perkin-Elmer, UK.

[6] M.J. Frisch, G.W. Trucks, H.B. Schlegel, G.E. Scuseria, M.A. Robb, J.R. Cheeseman, J.A. Montgomery, Jr., T. Vreven, K.N. Kudin, J.C. Burant, J.M. Millam, S.S. Iyengar, J. Tomasi, V. Barone, B. Mennucci, M. Cossi, G. Scalmani, N. Rega, G.A. Petersson, H. Nakatsuji, M. Hada, M. Ehara, K. Toyota, R. Fukuda, J. Hasegawa, M. Ishida, T. Nakajima, Y. Honda, O. Kitao, H. Nakai, M. Klene, X. Li, J.E. Knox, H.P. Hratchian, J.B. Cross, C. Adamo, J. Jaramillo, R. Gomperts, R.E. Stratmann, O. Yazyev, A.J. Austin, R. Cammi, C. Pomelli, J.W. Ochterski, P.Y. Ayala, K. Morokuma, G.A. Voth, P. Salvador, J.J. Dannenberg, V.G. Zakrzewski, S. Dapprich, A.D. Daniels, M.C. Strain, O. Farkas, D.K. Malick, A.D. Rabuck, K. Raghavachari, J.B. Foresman, J.V. Ortiz, Q. Cui, A.G. Baboul, S. Clifford, J. Cioslowski, B.B. Stefanov, G. Liu, A. Liashenko, P. Piskorz, I. Komaromi, R.L. Martin, D.J. Fox, T. Keith, M.A. Al-Laham, C.Y. Peng, A. Nanayakkara, M. Challacombe, P.M.W. Gill, B. Johnson, W. Chen, M.W. Wong, C. Gonzalez, J.A. Pople, *Gaussian 03, Revision E.01, Gaussian, Inc.*, Pittsburgh PA, 2007.

[7] A.D. Becke, *J. Chem., Phys.* 1993, **98**, 5648.

[8] C. Lee, W.Yang, R.G. Parr, *Phys. Rev.* B 1988, **37**, 785.

[9] T.H. Dunning Jr., *J. Chem. Phys.* 1989, **90**, 1007.

[10] J.B. Foresman, *Exploring Chemistry with Electronic Structure Methods*, 2nd Edition, Gaussian, Inc. Pittsburgh, PA 1996.

[11] N.S. Myshakina, S.A. Asher, *J. Phys. Chem.* B 2007, **111**, 4271.

[12] S. Ghosh, S. Mondal, A.Misra, S.Dalai, J. Mol. *Struct. Theochem*. 2007, 805, 133.

[13] J.A. Schachtschneider, *Vibrational Analysis of Polyatomic Molecules*, Parts V and VI, Technical Report Nos. 231 and 57, Shell Development Co., Houston TX, 1964 and1965.

[14] P.Pulay, G.Fogarasi, F.Pang, J.E. Boggs, A.Vargha, *J. Am. Chem.* Soc. 1983, **105**, 7037.

[15] *Gaussian 03*, Revision E.03, M.J. Frisch, G.W. Trucks, H.B. Schlegel, G.E. Scuseria, M.A. Robb, J.R. Cheeseman, J.A. Montgomery, Jr., T. Vreven, K.N. Kudin, J.C. Burant, J.M. Millam, S.S. Iyengar, J. Tomasi, V. Barone, B. Mennucci, M. Cossi, G. Scalmani, N. Rega, G.A. Petersson, H. Nakatsuji, M. Hada, M. Ehara, K. Toyota, R. Fukuda, J. Hasegawa, M. Ishida, T. Nakajima, Y. Honda, O. Kitao, H. Nakai, M. Klene, X. Li, J.E. Knox, H.P. Hratchian, J.B. Cross, V. Bakken, C. Adamo, J. Jaramillo, R. Gomperts, R.E. Stratmann, O. Yazyev, A.J. Austin, R. Cammi, C. Pomelli, J.W. Ochterski, P.Y. Ayala, K. Morokuma, G.A. Voth, P. Salvador, J.J. Dannenberg, V.G. Zakrzewski, S. Dapprich, A.D. Daniels, M.C. Strain, O. Farkas, D.K. Malick, A.D. Rabuck, K. Raghavachari, J.B. Foresman, J.V. Ortiz, Q. Cui, A.G. Baboul, S. Clifford, J. Cioslowski, B.B. Stefanov, G. Liu, A. Liashenko, P.

Piskorz, I. Komaromi, R.L. Martin, D.J. Fox, T. Keith, M.A. Al-Laham, C.Y. Peng, A. Nanayakkara, M. Challacombe, P.M.W. Gill, B. Johnson, W. Chen, M.W. Wong, C. Gonzalez, J.A. Pople, *Gaussian, Inc.*, Wallingford CT, 2004.

4. Vibrational Spectra and Structures of Urazole and 4-Methylurazole: DFT Calculations of the Normal Modes in Aqueous Solution and the Solid State, and the Influence of Hydrogen Bonding

4.1. Introduction

Urazole (1,2,4-triazolidine-3,5-dione, Figure 4.1) is a 5-membered ring species which is found in a large number of organic compounds. There have been suggestions that it may have been a prebiotic compound acting as the precursor to uracil.[1,2] Due to its structural "simplicity", urazole is an excellent candidate for detailed vibrational spectroscopic study and the examination of the influence of hydrogen bonding in aqueous solution and in the solid state. The IR and Raman spectra of urazole have been previously reported[3-6] and, more recently, Jensen[7] has reported *ab initio* calculations of the vibrational spectra using HF-SCF, MP2 and DFT methods. Of these three methods the DFT calculations (B3-LYP/6-311G**) gave the closest fit to experimental data, although rather severe scaling factors were necessary to obtain a satisfactory fit to some vibrations, in particular the ν(CO) and ν(CN) and modes i.e. 0.92 and 1.0406, respectively. Comparing the calculated geometry with experimental data from a crystal structure analysis[8] reveals that the computed CO distance is too short and the CN distance is too long, which is reflected in the poor fit to the stretching vibrations. The crystal structure indicates that there is strong intermolecular hydrogen bonding. This was not accounted for in the calculations, reported by Jensen, which were based upon the assumption of an isolated molecule in the gas phase.

The published crystallographic study of urazole[8] indicates that it has approximately C_2 symmetry, although not exactly so because of intermolecular hydrogen bonding; the structure of 4-methylurazole has no symmetry.[9] DFT calculations were performed using the *Gaussian 03* program[10], with the hybrid SCF-DFT method B3-LYP, which incorporates Becke's three parameter hybrid functional[11] and the Le, Yang and Parr correlation functional.[12] The triple-zeta cc-pVTZ basis set[13] was chosen in preference to Pople-style split-valence basis sets which are of triple-zeta quality on valence orbitals only. Furthermore, Dunning basis functions contain primitive Gaussian functions with small zeta values, such that additional diffuse functions are not usually needed for atoms with lone pairs.

4.2. Calculations

4.2.1. Computing Methodology for Solvated Molecules

Calculations involving implicit solvation were carried out using either the Integration Equation Formalism Polarizable Continuum Model (IEF-PCM),[14] the default *Gaussian 03* PCM method or the conductor-like polarizable continuum model (CPCM).[15] The CPCM model has been shown to be computationally more efficient for larger molecules[16] than the IEF-PCM model, and was therefore used for calculations involving clusters of either urazole or 4-methylurazole molecule with hydrogen-bonded water molecules. In all cases the molecular cavity was defined using the "united atom topological model",[17] *i.e.* by including a sphere around each solute heavy atom with hydrogen atoms enclosed in the sphere of the heavy atom to which they are bonded.

4.2.2. Methodology for Comparing Solvated Molecules

In order to compare the effects of implicit versus explicit solvation the modelling of urazole in aqueous solution involved the following computations: (i) PCM calculation of urazole alone (model I), (ii) gas-phase cluster calculation of urazole with five hydrogen-bonded H_2O molecules (model II), and (iii) CPCM calculation of urazole with five hydrogen-bonded H_2O molecules (model III). Models II and III were constructed such that all oxygen and hydrogen atoms are hydrogen-bonded, with O•••••H distances initially set at 1.75 Å. For urazole the symmetry of models II and III was constrained to be C_2, as for the isolated molecule. Calculations on 4-methylurazole followed the same protocol, except that only four water molecules are required to occupy all the hydrogen bonding sites.

The vibrational spectra of the isolated molecules and hydrogen-bonded models were calculated at their optimised geometries using the B3-LYP method with the cc-pVTZ basis set. For computation of the potential energy distributions associated with the vibrational modes, the Cartesian force constants obtained from the *Gaussian 03* output were converted to force constants expressed in terms of internal coordinates and input to a normal coordinate analysis program derived from those of Schachtschneide[18]. This procedure enabled, for the hydrogen-bonded models, the force constants associated with the water molecules to be removed. Symmetry-adapted linear combinations of internal coordinates were constructed according to the symmetry elements of the C_2 point group, even though 4-methylurazole does not, strictly, have C_2 symmetry. IR and Raman spectra were calculated using the Cartesian-based dipole and polarizability derivatives from the B3-LYP/cc-pVTZ calculations, which were transformed to internal coordinates and subsequently to normal coordinates. Simulated spectra were calculated by convolution with a Lorentzian lineshape (full-width-half-maximum = 10 cm^{-1}).

4.2.3. DFT Calculations of Urazole and 4-Methylurazole in the Solid State

Calculations were carried out using the PSPW CASTEP v4.3 program,[19] employing the generalized gradient approximation (GGA) functional PW91.[20] We used norm-conserving pseudopotentials optimised for GGA DFT methods with a basis set cut off energy of 816 eV. Brillouin zone integrations were performed with a 2,2,2 Monkhorst-Pack[21] grid and the Broyden-Fletcher-Goldfarb-Shanno optimisation scheme was used. Lattice parameters and atomic positions were optimised according to the following criteria: total energy convergence $< 2 \times 10^{-5}$ eV/atom, maximum force on any atom < 0.05 eV/Å, stress < 0.1 GPa and atomic displacements $< 10^{-3}$ Å. DFT calculations of the vibrational spectrum of urazole in the solid state were carried out at the optimised geometry, for the gamma-point only, and assignments were verified by visualisation of the phonon eigenvectors using the Moldraw program[22] The simulated IR spectrum was obtained by convolution of computed band intensities with a Lorentzian lineshape function (f.w.h.m. = 10 cm^{-1}).

4.3. Results and Discussion

4.3.1. DFT Calculations

The atomic numbering scheme for urazole and 4-methylurazole are show in Figure 4.1.

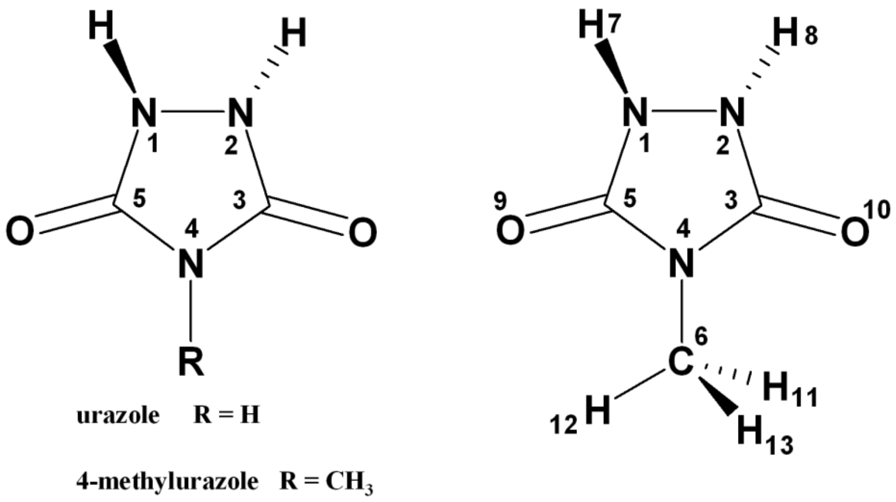

Figure 4.1. The atomic numbering scheme for urazole and 4-methylurazole

4.3.1.1. *Geometry Optimization*

The molecular geometries of models I, II and III for urazole and 4-methylurazole are optimised, with the symmetry constrained to be C_2 for urazole. The optimised geometries of the isolated molecules are shown in Figures 4.2 and 4.3, and the calculated bond lengths and interbond angles are listed in Tables 4.1 and 4.2, together with experimental data obtained from x-ray crystallographic measurements[8,9]. The results obtained from the solid-state DFT calculations on urazole and 4-methylurazole are also included in Tables 4.2 and 4.2, in both cases the geometries were optimised starting from the x-ray crystal structure[8,9]. Urazole was optimised with space group $P2_1/n$ and four molecules per unit cell, leading to an optimised geometry with unit cell parameters a = 5.4856 Å, b = 8.4386 Å, c = 11.2307 Å, $\alpha = \gamma = 90.0^\circ$ and $\beta = 103.53^\circ$ (c.f. experimental values a = 3.462 Å, b = 9.513 Å, c = 10.995 Å and $\beta = 95.06^\circ$). 4-methylurazole was optimised starting from the x-ray crystal structure[9] with point group *Pbca* and eight molecules per unit cell, leading to an optimised geometry with unit cell parameters a = 9.6327 Å, b = 7.8224 Å, c = 16.0223 Å, $\alpha = \beta = \gamma = 90.0^\circ$ (c.f. experimental values a = 9.891 Å, b = 6.492 Å and c = 14.840 Å).

The calculated structures provide accurate molecular shapes, especially in terms of the pyramidal geometry at N1 and N2 and planar geometry at N4, and reasonable values for bond distances and angles. The discrepancies for the N-H bond distances are attributed to the difficulty in determining hydrogen atom positions by x-ray crystallography, which in this case were constrained, and the computed distances should be regarded as more accurate. The best test of the various models employed is to compare the computed *r*(CO), *r*(NN) and *r*(CN) distances with the experimental values. Although the *r*(CN) distances are well reproduced by the PSPW calculation of the solid, the other distances are not and this is attributed to the poorer performance of the pure DFT method PW91 than the hybrid B3-LYP method used for the solution phase models. Although hybrid DFT methods can be used with PSPW methods this represents a huge computational problem which was not considered to be justified.

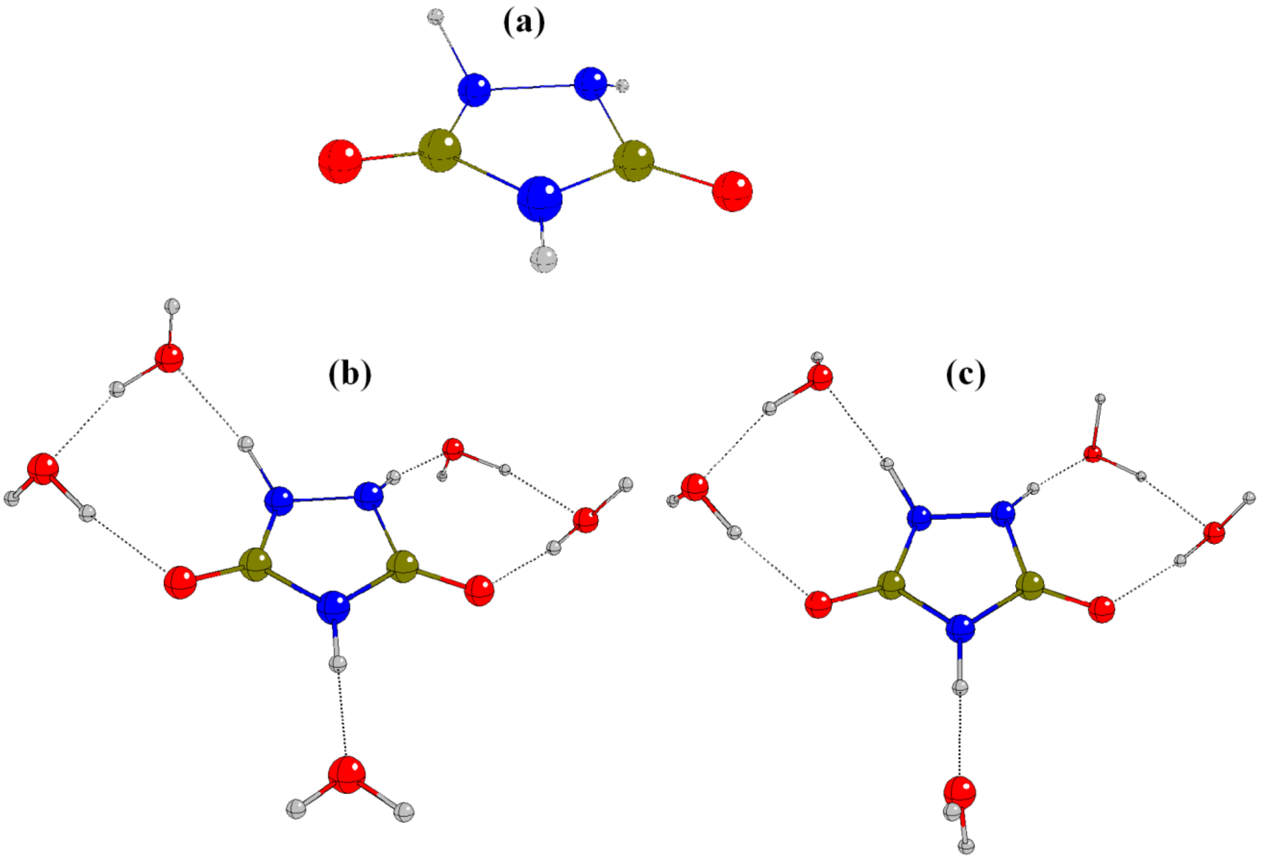

Figure 4.2. Calculated structures of urazole

(a) implicit solvation with PCM model only (model I), (b) explicit solvation only with five hydrogen-bonded water molecules (model II), and (c) implicit and explicit solvation with five hydrogen-bonded water molecules in conjunction with the CPCM solvation model (model III).

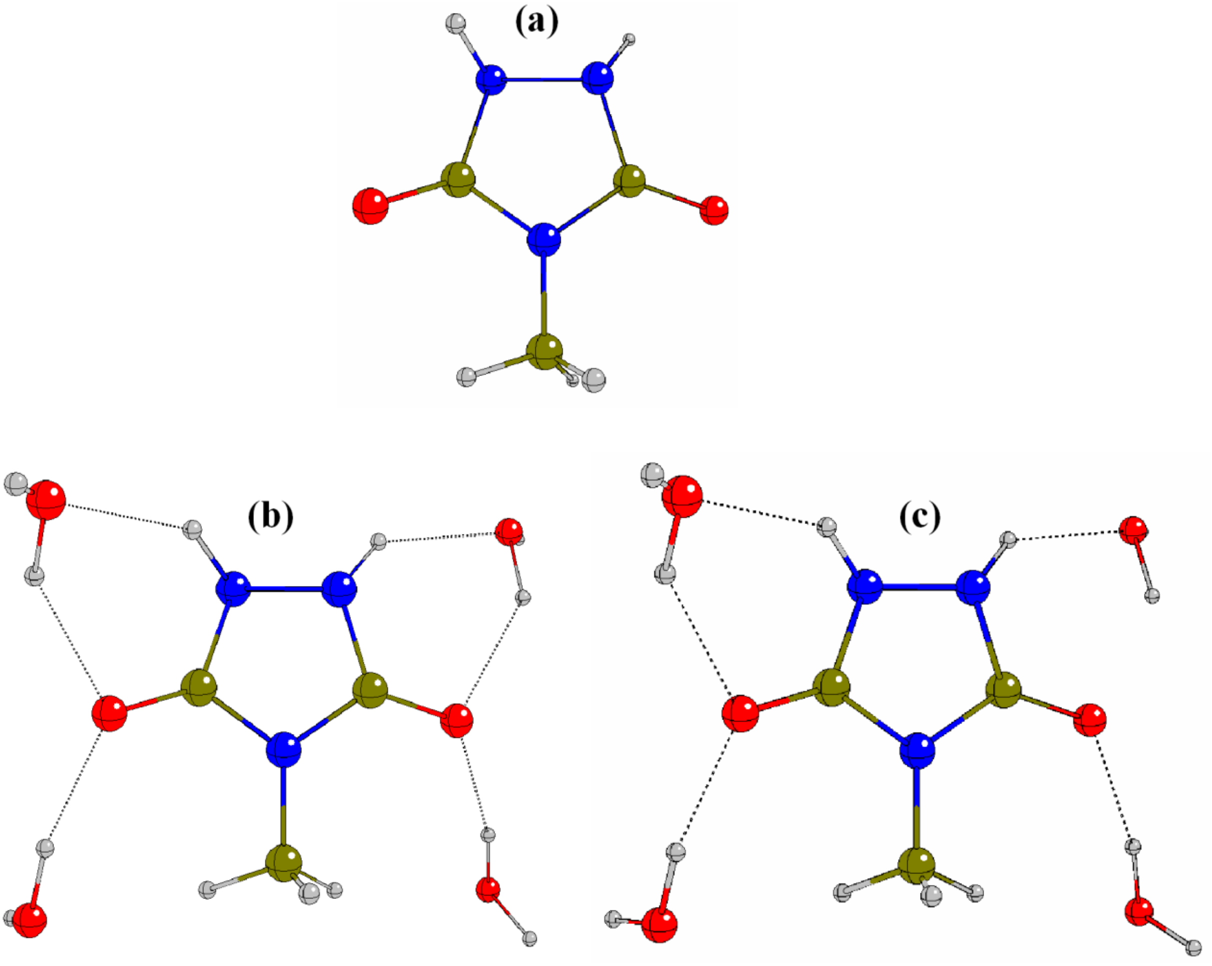

Figure 4.3. Calculated structure of 4-methylurazole:

(a) implicit solvation with PCM model only (model I), (b) explicit solvation only with four hydrogen-bonded water molecules (model II), and (c) Implicit and explicit solvation with four hydrogen-bonded water molecules in conjunction with the CPCM solvation model (model III).

Table 4.1. Experimental and calculated structure of urazole (bond distances in Ångstrom units and bond angles in degrees)

	Expt.[ref]	Calculated			
		Solid	Model I	Model II	Model III
r(N1H)	1.020[a]	1.0417 1.0383	1.0269	1.0313	1.0340
r(N4H)	1.020[a]	1.0508	1.0237	1.0177	1.0268
r(NN)	1.410[b]	1.3816	1.4162	1.4085	1.4063
r(CN1)	1.361[b]	1.3638 1.3619	1.3822	1.3680	1.3653
r(CN4)	1.379[b]	1.3746 1.3926	1.3817	1.3812	1.3788
r(CO)	1.235[b]	1.2524 1.2407	1.2170	1.2262	1.2307
r(N1H····O)	1.803			1.7973	1.7874
	2.074				
	2.235				
r(N4H····O)	1.731			1.8642	1.7693
r(O····H)	2.155[b]			1.7658	1.8072
	1.767[b]				
θ(CN1H)	121.1[b]	123.82 121.69	117.04	120.42	120.73
θ(N2N1H)	117.8[b]	121.19 120.95	114.72	117.69	117.65
θ(CN4H)	124.9[b]	126.49 123.32	124.09	124.39	124.61
θ(N1N2C)	108.0[b]	108.66 109.11	107.91	108.25	108.14
θ(N1CN4)	106.4[b]	106.14 105.47	105.32	105.57	105.95
θ(CN4C)	110.2	110.19	111.81	111.22	110.78
θ(N1CO)	127.5[b]	126.60 127.50	126.98	127.96	127.36
θ(N4CO)	126.1[b]	127.26 127.03	127.70	126.47	126.69

a. constrained; b. average

Table 4.2 Experimental and calculated structure of 4-methylurazole (bond distances in Ångstrom units and bond angles in degrees)

	expt.	solid	Model I	Model II	Model III
r(N4-C3)	1.3726	1.3891	1.3848	1.3839	1.3864
r(N4-C5)	1.3745	1.3908	1.3866	1.3846	1.3850
r(C5-O9)	1.2295	1.2406	1.2172	1.2246	1.2274
r(N1-C5)	1.3539	1.3686	1.3805	1.3738	1.3653
r(N1-N2)	1.4188	1.3856	1.4154	1.4069	1.4079
r(N1-H7)	0.9826	1.0464	1.0272	1.0210	1.0315
r(C3-N2)	1.3476	1.3639	1.3810	1.3726	1.3653
r(N4-C6)	1.4575	1.4505	1.4502	1.4594	1.4537
r(H8-N2)	1.0315	1.0470	1.0275	1.0212	1.0315
r(O10-C3)	1.2304	1.2440	1.2172	1.2252	1.2265
r(H11-C6)	0.9565	1.0959	1.0885	1.0877	1.0877
r(H12-C6)	0.9482	1.0946	1.0863	1.0864	1.0859
r(C6-H13)	0.9569	1.0963	1.0894	1.0897	1.0902
r(H8····O)	1.8016	1.7047		1.9727	1.7963
r(O9····H)	1.8016	1.7047		1.9375	1.8776
r(O10····H)	1.8440	1.7209		1.9281	1.8559
r(H7····O)	1.8440	1.7209		1.9714	1.7917
θ(C3-N4-C5)	109.42	109.88	110.86	109.91	110.110
θ(N4-C3-N2)	107.27	105.86	105.97	106.52	106.17
θ(C3-N4-C6)	125.04	125.34	124.26	124.41	125.60
θ(N4-C3-O10)	125.71	126.33	126.75	127.25	127.24
θ(N4-C5-O9)	126.21	126.42	127.11	127.78	126.70
θ(N4-C5-N1)	107.22	105.87	105.84	106.34	106.34
θ(C5-N4-C6)	125.21	124.72	124.88	125.67	124.27
θ(O9-C5-N1)	126.56	127.71	127.05	125.87	126.96
θ(C5-N1-N2)	107.23	108.57	107.93	107.85	108.04
θ(C5-N1-H7)	120.98	120.67	116.77	115.66	119.11
θ(N2-N1-H7)	119.39	119.76	114.62	118.14	116.98
θ(N1-N2-C3)	107.58	108.99	107.72	107.72	108.21
θ(N1-N2-H8)	117.07	120.72	114.51	118.14	117.03
θ(C3-N2-H8)	127.37	121.80	116.75	115.65	119.53
θ(N2-C3-O10)	127.02	127.80	127.28	126.23	126.59
θ(H13-C6-N4)	109.88	110.53	110.57	109.97	110.43
θ(H13-C6-H11)	108.33	108.66	109.15	109.31	109.07
θ(H13-C6-H12)	109.00	109.42	109.64	109.11	109.13
θ(N4-C6-H11)	110.14	110.56	110.04	109.23	109.56
θ(N4-C6-H12)	110.44	107.62	107.75	108.68	108.50
θ(H11-C6-H12)	109.01	110.04	109.68	110.53	110.13

Table 4.3. Symmetry coordinates for the 5-membered ring system

δ_{ip}(ring-1) =	$^{2}/_{\sqrt{7}}\,[\theta(\mathrm{C3N4C5}) + a\theta(\mathrm{N2C3N4}) + b\theta(\mathrm{N1N2C3}) + b\theta(\mathrm{C5N1N2}) + a\theta(\mathrm{N4C5N1})]$
δ_{ip}(ring-2) =	$^{2}/_{\sqrt{p}}\,[(a - b)\theta(\mathrm{N2C3N4}) + (1 - a)\theta(\mathrm{N1N2C3}) - (1 - a)\theta(\mathrm{C5N1N2}) - (a - b)\theta(\mathrm{N4C5N1})]$
δ_{op}(ring-1) =	$^{2}/_{\sqrt{7}}\,[b\tau(\mathrm{C5N4C3N2}) + a\tau(\mathrm{N4C3N2N1}) + \tau(\mathrm{C3N2N1C5}) + a\tau(\mathrm{N2N1C5N4}) + b\tau(\mathrm{N1C5N4C3})]$
δ_{op}(ring-1) =	$^{2}/_{\sqrt{p}}\,[-(1 - a)\tau(\mathrm{C5N4C3N2}) - (a - b)\tau(\mathrm{N4C3N2N1}) + (a - b)\tau(\mathrm{N2N1C5N4}) + (a - b)\tau(\mathrm{N1C5N4C3})]$

where $a = \cos 144°$, $b = \cos 72°$ and $p = ½\,(7 - 5 \cos 144°)$

Comparison of the three solution phase models reveals that model III (explicit and implicit solvation) gives the best fit to the experimental geometry. This is in accord with recent studies of the amino acid Gly and L-Ala zwitterions[23] and the peptide L-Asp-L-Glu[24]. In both studies we showed that computation of the structures and vibrational spectra in aqueous solution requires both explicit and implicit solvation models in order to obtain accurate predictions of structures and vibrational spectra. All computed geometric parameters were substantially more accurate than those obtained by Jensen[7] using HF, B3-LYP and MP2 methods in conjunction with the 6-311G**. Those calculations were carried out for an isolated urazole molecule and no account was taken of hydrogen bonding.

4.3.2. Vibrational Assignments

Urazole has 24 vibrations, which transform as $12a + 12b$ in the C_2 point group, and 4-methylurazole, with no symmetry has 33 vibrations. However, in both cases symmetry coordinates were constructed assuming two-fold symmetry, resulting in symmetric and antisymmetric combinations for most internal coordinates. The in-plane and out-of-plane deformations of the 5-membered ring, listed in Table 4.3, were combined according to the recommendations of Pulay[25]. For solid urazole the factor group is C_{2h}, with four molecules per unit cell, each lying on an equivalent site of C_1 symmetry. This leads to 96 internal modes which transform as:

$$\Gamma_{\mathrm{int}} = 24a_g + 24b_g + 24a_u + 24b_u$$

Thus each of the 24 molecular vibrations is split into four components of which two are IR active (a_u and b_u) and two are Raman active (a_g and b_g), representing the four possible phase relationships between the internal vibrations of the molecules within the unit cell. The external vibrations consist of 9 lattice modes and 12 librational modes, which transform as:

$\Gamma_{\text{lattice}} = 3a_g + 3b_g + 2a_u + b_u$ $\Gamma_{\text{lib}} = 3a_g + 3b_g + 3a_u + 3b_u$

Thus there are 3 lattice modes and 6 librational modes active in IR, and 6 of each are Raman active. In the case of 4-methylurazole the PSPW calculation of the vibrational spectrum proved intractable due to the large number of atoms in the unit cell.

Experimental Raman (solid state and aqueous solution) and solid-state IR spectra of urazole are shown in Figures 4.4 and 4.5, and for 4-methylurazole in Figures 4.8 and 4.9, together with the spectra computed for various models. The corresponding spectra for urazole-d_3 are shown in Figures 4.6 and 4.7, and for 4-methylurazole-d_2 in Figures 4.10 and 4.11. Experimental and calculated band positions, with band assignments listed as potential energy distributions (p.e.d.s), are given in Table 4.4 for urazole, Table 4.5 for urazole-d_3, Table 4.6 for 4-methylurazole and Table 4.7 for 4-methylurazole-d_2. The inclusion of hydrogen bonding leads to much improved band assignments and many of those given here contradict the earlier assignments[7]. Discussion of the band assignments for all of these species is divided into consideration of the NH, C=O and ring modes.

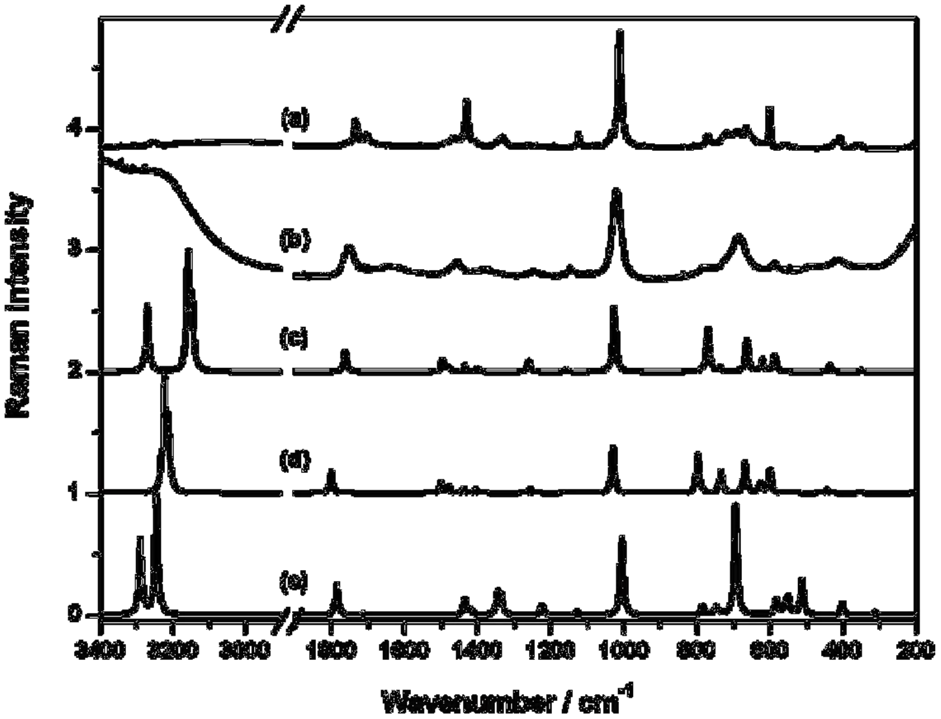

Figure 4.4. Experimental Raman spectra of (a) urazole (solid state) and (b) an aqueous solution of urazole, and calculated Raman spectra: (c) model III, (d) model II, and (e) model I.

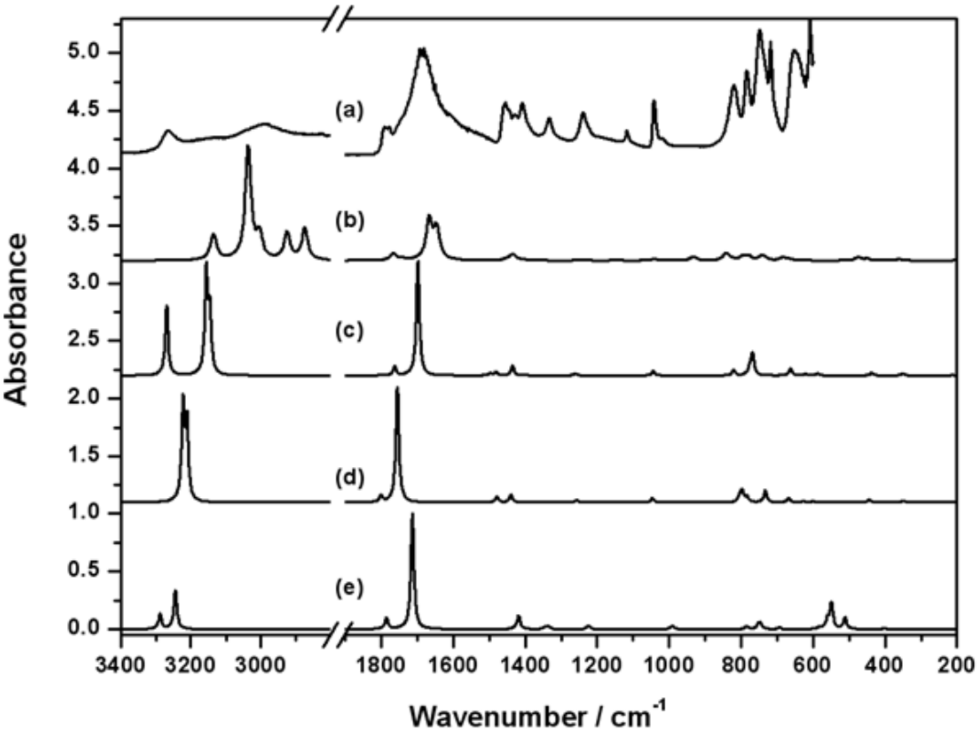

Figure 4.5. Experimental IR spectrum of urazole (solid state) (a), and calculated IR spectra: (b) from solid state calculation, (c) model III, (d) model II, and (e) model I.

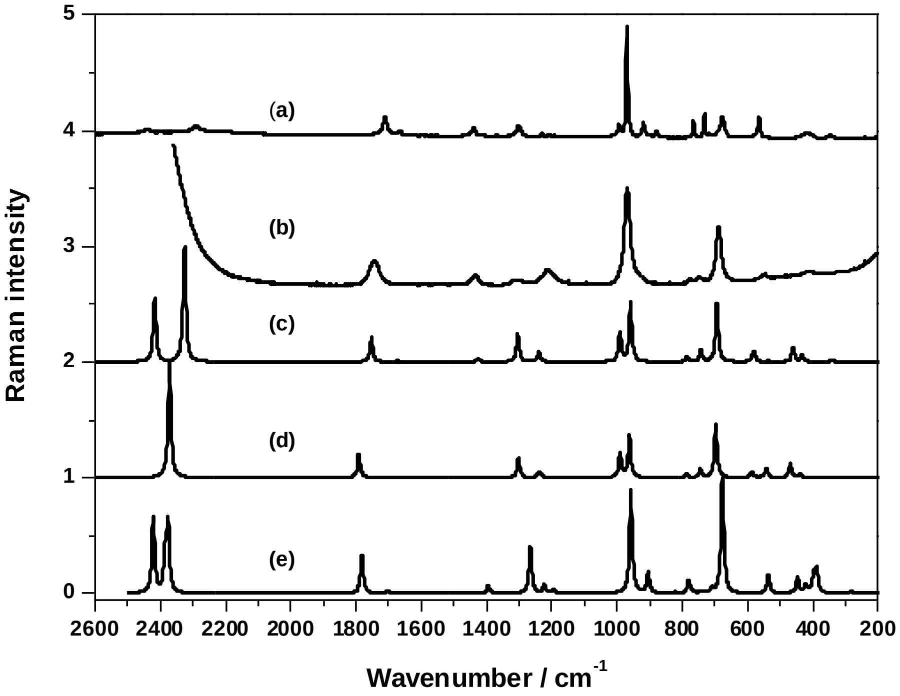

Figure 4.6. Experimental Raman spectra of (a) solid state urazole-d_3 and (b) an aqueous solution of urazole-d_3 in D_2O, and calculated Raman spectra: (c) model III, (d) model II, and (e) model I.

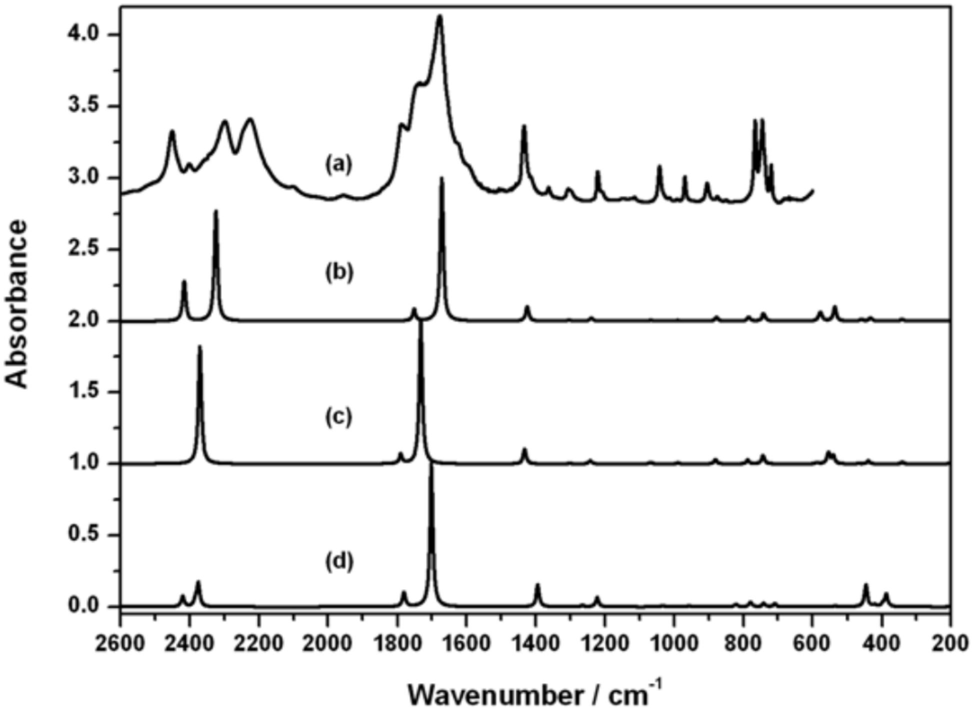

Figure 4.7. Experimental IR spectrum of solid state urazole-d_3 (a), and calculated IR spectra: (b) model III, (c) model II, and (d) model I.

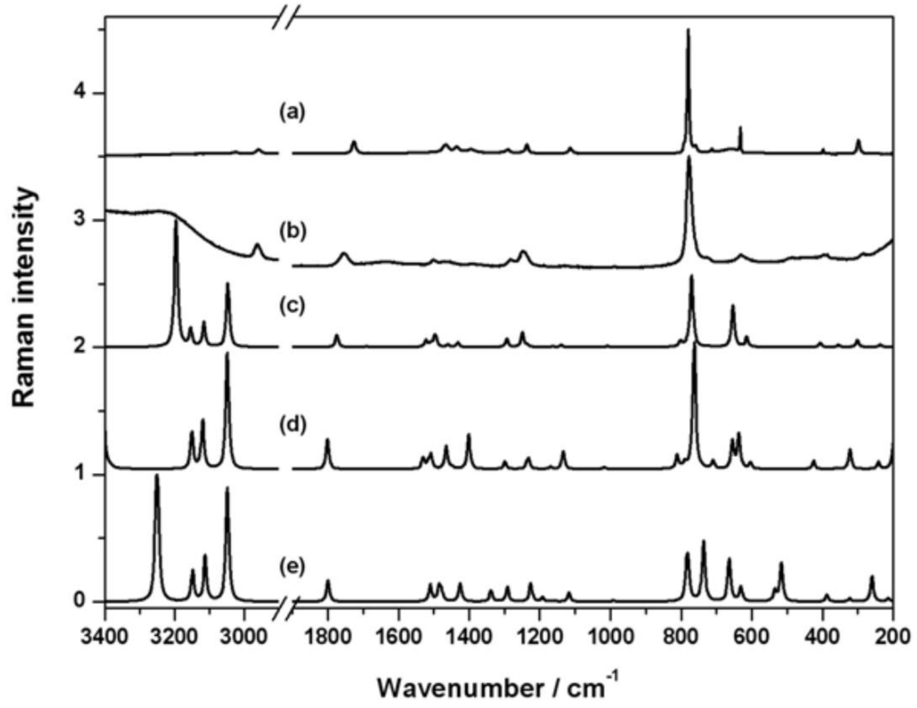

Figure 4.8. Experimental Raman spectra of (a) solid state 4-methylurazole and (b) an aqueous solution of 4-methylurazole, and calculated Raman spectra: (c) model III, (d) model II, and (e) model I.

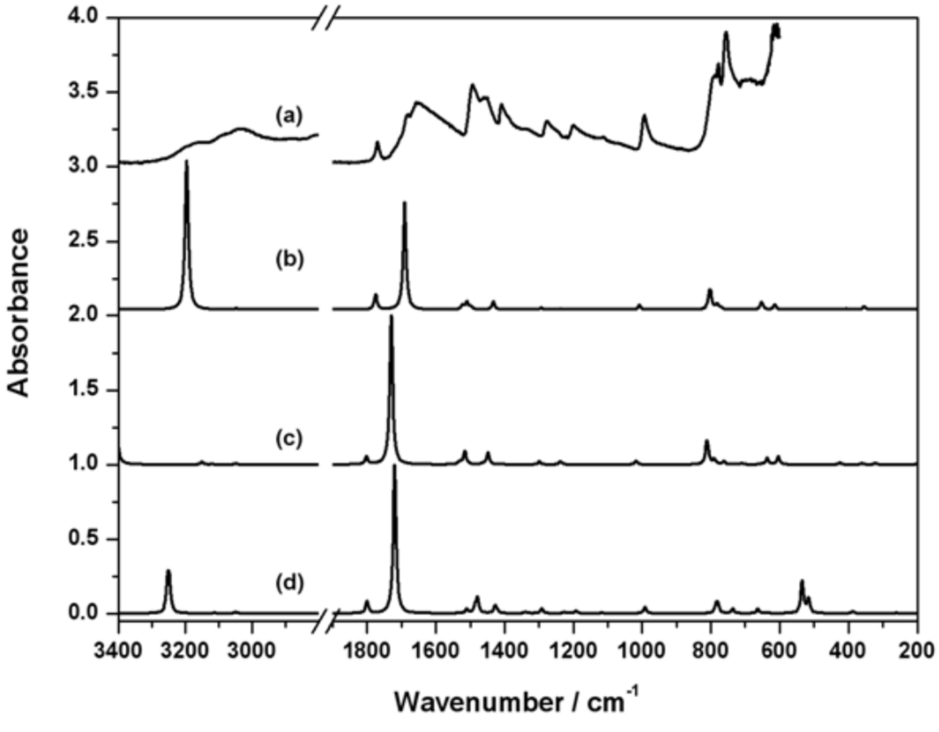

Figure 4.9. Experimental IR spectrum of solid state 4-methylurazole (a), and calculated IR spectra: (b) model III, (c) model II, and (d) model I.

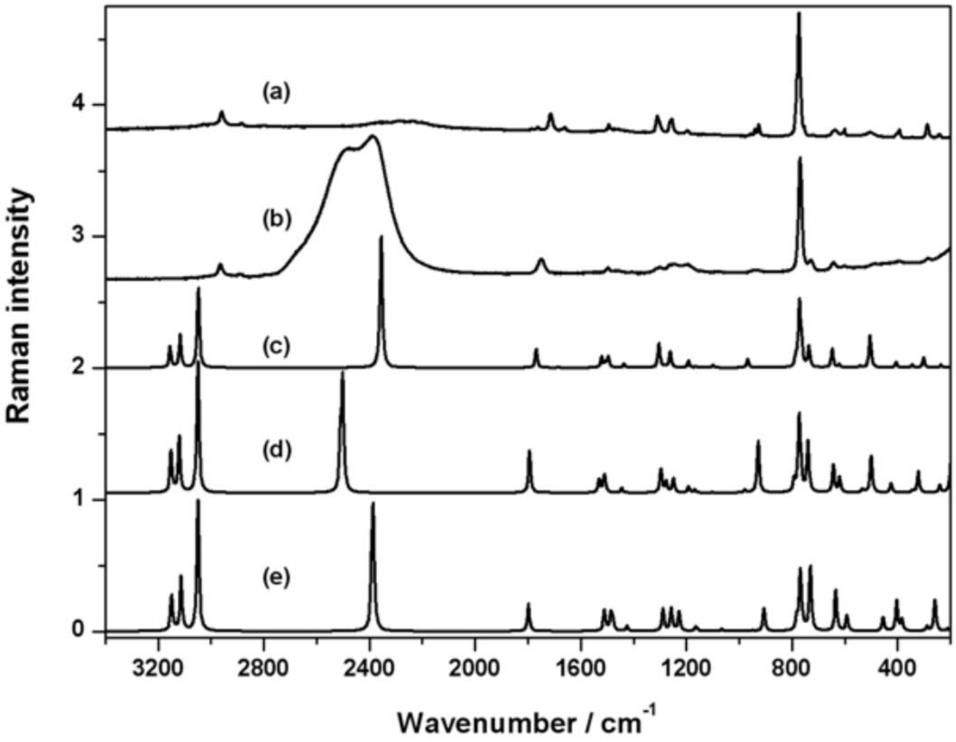

Figure 4.10. Experimental Raman spectra of (a) solid state 4-methylurazole-*d*$_2$ and (b) an aqueous solution of 4-methylurazole-*d*$_2$ in D2O, and calculated Raman spectra: (c) model III, (d) model II, and (e) model I.

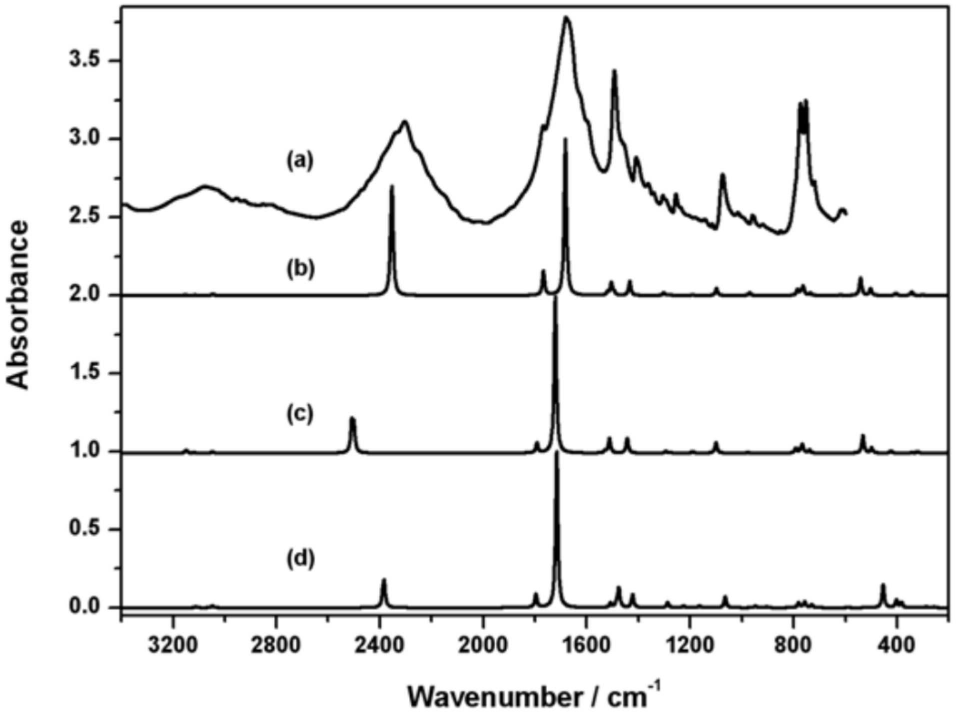

Figure 4.11. Experimental IR spectrum of solid state 4-methylurazole-*d*$_2$ (a), and calculated IR spectra: (b) model III, (c) model II, and (d) model I.

4.3.2.1. ***NH Vibrations***

ν(NH) vibrations are observed in the range 3100-3250 cm^{-1} for both urazole and 4-methylurazole, as expected for NH groups in strong hydrogen bonding. The ν(N4H) vibration, appearing only in urazole, is at lower wavenumber than the ν(N1H) modes. This is in accordance with the different bonding at the N4 atom where there is planar geometry, as opposed to the pyramidal geometry at the N1 atoms. The calculated values for ν(NH), and also ν(CH), are normally substantially higher than their observed positions due to the large anharmonic contribution to stretching vibrations involving hydrogen atoms. However, in the present case we have obtained computed values for model III (explicit and implicit solvation) that are in remarkably good agreement (within ca 20 cm^{-1}) with experimental values. This can be attributed to overcompensation of hydrogen bonding in the DFT methods employed here. In the PSPW calculations of solid urazole the computed ν(NH) values are actually substantially less than their observed positions, which can be attributed to the poorer performance of the pure DFT functional PW91, with respect to B3-LYP, when taking account of hydrogen bonds.

Calculated values for in-plane NH deformations are higher than their observed values for model III and closer agreement is actually found for model I (implicit solvation only), suggesting that NH----O hydrogen bonding is less well represented by the model involving both implicit and explicit solvation. By contrast, model III actually gives much better agreement for the deuterated species. Prediction of out-of-plane NH deformations is generally satisfactory for model III.

Table 4.4. Experimental and calculated vibrational spectrum of urazole

IR Solid	Raman solid	Raman soln.	PSPW				Model I	Model II	Model III	Assignments (% p.e.d.s)
a symmetry										
			a_g	b_g	a_u	b_u				
3259m	3254w		2826	2827	2874	2925	3288	3443	3269	ν(N4H) (99)
3120w,br			3067	3051	3136	3036	3244	3222	3156	ν_s(N1H) (99)
2742m										
1774m	1761sh 1733s	1757m	1702	1694	1739	1764	1785	1800	1762	ν_s(CO) (70), δ_{ip}(ring-1) (10)
1452m	1465m	1462w	1441	1440	1430	1449	1418	1478	1480	$\delta_{ip,s}$(N1H) (79)
1423w	1430s	1388w	1386	1399	1405	1399	1335	1438	1434	ν_s(CN4) (32), ν_s(CN1) (33), $\delta_{ip,s}$(N1H) (11), $\delta_{ip,s}$(CO) (14)
1116w	1124m	1151w	1145	1148	1147	1144	1127	1155	1157	ν(NN) (72)
1014w,sh	1011vs	1019s	1000	998	1005	998	1004	1029	1025	ν_s(CN4) (19), ν_s(CN1) (33), δ_{ip}(ring-1) (27), $\delta_{op,s}$(N1H) (10)
783m	771m	786w	825	848	827	841	745	797	769	$\delta_{op,s}$(N1H) (80), $\delta_{op,s}$(CO) (13)
718s	690m	689m	715	718	737	745	693	735	736	$\delta_{op,s}$(CO) (75), δ_{op}(ring-1) (17)
649s	664m	660sh	643	641	660	685	549	667	662	ν_s(CO) (13), δ_{ip}(ring-1) (49), $\delta_{op,s}$(N1H) (16)
	422sh 409m	422w	424	411	449	474	401	443	436	ν_s(CN4) (17), $\delta_{ip,s}$(CO) (71)
	364w 353w		346	356	359	360	312	350	350	$\delta_{op,s}$(CO) (10), δ_{op}(ring-1) (95)
b symmetry										
2980m			2989	3076	3004	3132	3245	3211	3146	ν_{as}(N1H) (99)
1682vs	1704m		1666	1706	1666	1645	1713	1755	1698	ν_{as}(CO) (58), ν_{as}(CN1) (11), δ_{ip}(N4H) (10)
1407m	1412sh		1485	1483	1480	1496	1434	1500	1496	ν_{as}(CO) (14), $\delta_{ip,as}$(N1H) (71)
1331m	1340sh 1330m		1420	1417	1441	1436	1344	1404	1401	ν_{as}(CO) (15), δ_{ip}(N4H) (74)
1237m	1257vw	1253w	1247	1250	1244	1235	1223	1256	1259	ν_{as}(CN4) (21), ν_{as}(CN1) (33), $\delta_{ip,as}$(N1H) (14), δ_{ip}(ring-2) (12)
1041s	1044sh 1033sh		1034	1042	1042	1040	990	1045	1043	ν_{as}(CN4) (62), ν_{as}(CN1) (18)
818m	801vw		909	909	928	934	784	804	820	δ_{ip}(ring-2) (11), δ_{op}(N4H) (37), $\delta_{op,as}$(N1H) (12), δ_{op}(ring-2) (19)
783m	771m		764	775	778	795	752	783	776	$\delta_{op,as}$(CO) (69)
748s	717w	720sh	735	736	733	734	582	733	767	δ_{ip}(ring-2) (47), $\delta_{op,as}$(N1H) (40)
	600s	589w	679	681	680	671	561	626	620	$\delta_{ip,as}$(CO) (88)
	558w	497vw	591	593	617	616	511	599	587	δ_{ip}(ring-2) (12), δ_{op}(N4H) (17), $\delta_{op,as}$(N1H) (68)
	202w 181w		219	215	208	207	185	209	212	$\delta_{op,as}$(CO) (17), δ_{op}(ring-2) (86)

Table 4.5. Experimental and calculated vibrational spectrum of urazole-d_3

IR solid	Raman solid	Raman soln.	Model I	Model II	Model III	Assignments (% p.e.d.s)
a symmetry						
2450m 2398w	2447w		2421	2537	2417	ν(N4D) (95)
2222m	2215sh		2376	2371	2324	ν_s(N1D) (96)
1782sh 1728sh	1712m	1746m	1781	1791	1752	ν_s(CO) (74), δ_{ip}(ring-1) (10)
1433s 1413sh	1441m 1425vw	1437w	1394	1432	1425	ν_s(CN4) (34), ν_s(CN1) (40), $\delta_{ip,s}$(CO) (20)
1221m	1231w	1217m	1194	1237	1239	ν(NN) (46), $\delta_{ip,s}$(N1D) (33)
970m	994w 970vs	968vs	957	990	991	ν_s(CN4) (17), ν_s(CN1) (24), $\delta_{ip,s}$(N1D) (40)
	919m		904	962	958	ν_s(CN1) (15), ν(NN) (32), $\delta_{ip,s}$(N1D) (24) , δ_{ip}(ring-1) (13)
745s	732m	751w	741	742	739	$\delta_{op,s}$(CO) (89)
	677m	689s	677	697	693	ν_s(CO) (14), ν_s(CN4) (13), δ_{ip}(ring-1) (52), $\delta_{op,s}$(N1D) (11)
522w		554w	447	555	537	$\delta_{op,s}$(N1D) (97)
	425w 416sh	415w	398	440	433	ν_s(CN4) (17), $\delta_{ip,s}$(CO) (70)
	351w		281	341	342	δ_{op}(ring-1) (100)
b symmetry						
2296m	2297w		2384	2371	2327	ν_{as}(N1D) (96)
1677vs	1668w	1690sh	1702	1733	1672	ν_{as}(CO) (73), ν_{as}(CN1) (10)
1362w 1298w	1376w 1302m	1313w	1265	1302	1304	ν_{as}(CN4) (11), ν_{as}(CN1) (46), $\delta_{ip,as}$(N1D) (20), δ_{ip}(ring-2) (11)
1206sh	1211vw		1223	1243	1240	ν_{as}(CO) (15), ν_{as}(CN4) (48), $\delta_{ip,as}$(N1D) (27)
1042m	1060vw		1034	1069	1068	δ_{ip}(N4D) (22), $\delta_{ip,as}$(N1D) (55), δ_{ip}(CO) (15)
904w 873vw 848vw	910vw 881w		822	881	878	ν(CN1) (33), δ_{ip}(N4D) (37), δ_{ip}(ring-2) (11)
766s	765m	778w	779	788	785	δ_{ip}(ring-2) (12), $\delta_{op,as}$(CO) (70), δ_{op}(ring-2) (19)
720m	725vw		710	744	743	ν_{as}(CN1) (21), δ_{op}(ring-2) (48)
			536	587	582	$\delta_{ip,as}$(CO) (70), δ_{op}(N4D) (12)
576m	565m		421	541	577	δ_{op}(N4D) (78), $\delta_{op,as}$(N1D) (14)
			388	469	460	δ_{op}(N4D) (18), $\delta_{op,as}$(N1D) (78)
			183	207	210	$\delta_{op,as}$(CO) (17), δ_{op}(ring-2) (88)

Table 4.6. Experimental and calculated vibrational spectrum of 4-methylurazole

IR solid	Raman solid	Raman soln.	Model I	Model II	Model III	Assignments (% p.e.d.s)
	3200br		3252	3414	3196	ν_s(NH) (99)
3149w			3247	3407	3193	ν_{as}(NH) (99)
3024m	3029w		3148	3150	3153	ν_{as}(CH$_3$) (98)
		2965m	3112	3119	3116	ν_{as}(CH$_3$) (93)
2873vw 2788w	2906v	2905w	3048	3048	3047	ν_s(CH$_3$) (91)
1758m	1727m	1758m	1800	1801	1774	ν_s(CO) (71), δ_{ip}(ring-1) (11)
1672sh 1646vs			1720	1730	1690	ν_{as}(CO) (71), ν_{as}(CN1) (12)
	1512vw	1505w	1510	1530	1522	δ_s(CH$_3$) (18), δ_{as}(CH$_3$) (40)
1492vs			1486	1516	1509	ν(CN4) (12), δ_s(CH$_3$) (19), δ_{as}(CH$_3$) (41)
	1469m	1477w	1478	1508	1498	$\delta_{ip,as}$(NH) (72)
			1427	1465	1495	δ_{as}(CH$_3$) (81)
1449sh	1438w		1424	1448	1460	$\delta_{ip,s}$(NH) (74), δ_s(CH$_3$) (21)
1408m	1401w	1402vw	1338	1401	1432	ν_s(CN4) (18), $\delta_{ip,s}$(NH) (10), δ_s(CH$_3$) (42)
1274m	1292w	1286w	1292	1299	1294	ν_{as}(CN4) (35), ρ_{ip}(CH$_3$) (13), ρ_{op}(CH$_3$) (16)
1247sh			1226	1237	1249	ν(N4C6) (32), ν_s(CN1) (44)
	1237m	1250m	1192	1231	1235	ν_{as}(CN1) (35), $\delta_{ip,as}$(NH) (12), $\delta_{ip,as}$(CO) (11), ρ_{ip}(CH$_3$) (12)
1196m 1161sh			1157	1169	1164	ρ_{ip}(CH$_3$) (46), ρ_{op}(CH$_3$) (42)
1108vw	1115m	1146w	1117	1134	1139	ν(NN) (69)
993s			992	1017	1008	ν_{as}(CN4) (44), ρ_{ip}(CH$_3$) (16), ρ_{op}(CH$_3$) (21)
783m	781vs	778vs	786	812	804	ν(N4C6) (10), $\delta_{op,s}$(NH) (44), $\delta_{op,s}$(CO) (12), δ_{ip}(ring-2) (15)
			783	809	800	δ_{op}(NH) (20), δ_{ip}(ring-2) (36)
			779	790	782	$\delta_{op,s}$(CO) (72), δ_{op}(ring-1) (10)
756vs	768sh	738sh	736	763	770	ν(N4C6) (13), ν_s(CN4) (23), ν_s(CN1) (19), ν(NN) (14), $\delta_{op,s}$(NH) (19)
	713w		664	710	723	$\delta_{op,s}$(CO) (71), δ_{op}(ring-1) (20)
682w	669w		631	655	653	$\delta_{ip,as}$(CO) (15), δ_{ip}(ring-2) (18), $\delta_{op,as}$(NH) (65)
	632s	635w	535	636	651	ν_{as}(CN1) (17), $\delta_{ip,as}$(CO) (58)
	621vw 587vw	494w	516	604	614	ν(N4C6) (15), δ_{ip}(ring-1) (61)
	399w	401w	387	425	406	ν_s(CN4) (23), $\delta_{op,s}$(CO) (62)
			323	360	354	$\delta_{op,s}$(CO) (10), δ_{op}(ring-1) (92)
	299m	285w	259	322	301	δ_{ip}(N4C6) (74), $\delta_{ip,as}$(CO) (12)
	271vw	289w	214	241	236	δ_{op}(N4C6) (91)
	193vw		156	199	181	$\delta_{op,as}$(CO) (11), δ_{op}(ring-2) (79)
	130m		36	190	154	τ(N4C6) (94)

Table 4.7. Experimental and calculated vibrational spectrum of 4-methylurazole-d_2

IR solid	Raman solid	Raman soln.	Model I	Model II	Model III	Assignments (% p.e.d.s)
3175w,br 3070m,br 3015sh	3037w 3010vw	3030sh,br	3148	3150	3153	$\nu_{as}(CH_3)$ (98)
2949w 2915w	2960m	2966m	3112	3119	3116	$\nu_{as}(CH_3)$ (93)
2842w 2809w	2890w 2808w	2898w 2804vw	3048	3048	3047	$\nu_{s}(CH_3)$ (91)
2330sh 2301s	2373w 2298w		2389	2509	2358	$\nu_{as}(ND)$ (96)
2251sh 2200sh 2151sh	2248vw 2211vw		2384	2500	2353	$\nu_{s}(ND)$ (97)
1765sh	1788w 1766w	1751m	1797	1793	1768	$\nu_{s}(CO)$ (74), δ_{ip}(ring-1) (11)
1675vs 1627sh 1595sh	1714m 1662w	1680vw	1716	1722	1683	$\nu_{as}(CO)$ (75), $\nu_{as}(CN1)$ (11)
1493s	1494m	1501w	1510	1530	1520	$\delta_{s}(CH_3)$ (14), $\delta_{as}(CH_3)$ (54)
			1485	1513	1506	$\nu(CN4)$ (15), $\delta_{s}(CH_3)$ (30), $\delta_{as}(CH_3)$ (28)
1465sh	1467w,br	1472vw,br	1477	1508	1495	$\delta_{as}(CH_3)$ (83)
1408m 1361vw	1372vw	1419vw	1424	1444	1435	$\nu_{s}(CN4)$ (18), $\delta_{s}(CH_3)$ (54)
1339vw 1304w	1310m	1311w	1288	1295	1303	$\nu_{as}(CN4)$ (16), $\nu_{\alpha\sigma}(CN1)$ (39), $\delta_{ip,as}(ND)$ (17), δ_{ip}(ring-2) (11)
1291sh		1267sh	1256	1275	1281	$\nu_{as}(CO)$ (11), $\nu_{as}(CN4)$ (17), $\rho_{ip}(CH_3)$ (16), $\rho_{op}(CH_3)$ (17)
1255m 1235sh	1256m	1250w	1227	1249	1260	$\nu(N4C6)$ (16), $\nu_{s}(CN1)$ (33), $\nu(NN)$ (29), $\delta_{ip,s}(ND)$ (11)
1175vw	1201w	1210w	1165	1191	1191	$\nu(N4C6)$ (22), $\nu_{s}(CN1)$ (13), $\nu(NN)$ (19), $\delta_{ip,s}(ND)$ (24), δ_{ip}(ring-2) (10)
1138vw	1134vw	1140sh,br	1156	1168	1164	$\rho_{ip}(CH_3)$ (49), $\rho_{op}(CH_3)$ (39)
1114vw 1072m	1090vw	1088vw	1065	1101	1099	$\nu_{as}(CN4)$ (18), $\delta_{ip,as}(ND)$ (44), $\rho_{op}(CH_3)$ (11)
1012w 993sh	960vw		948	978	971	$\nu_{as}(CN4)$ (28), $\nu_{as}(CN1)$ (11), $\delta_{ip,as}(ND)$ (23), $\rho_{ip}(CH_3)$ (11), $\rho_{op}(CH_3)$ (14)
953w 911vw	941w 926m	950w	905	927	967	$\nu(NN)$ (33), $\delta_{ip,s}(ND)$ (59)
846vw 772vs	773vs	770vs	781	792	785	δ_{ip}(ring-2) (15), $\delta_{op.as}(CO)$ (67), δ_{op}(ring-2) (12)
	758sh		768	772	771	$\nu(N4C6)$ (18), $\nu_{s}(CN4)$ (21), $\nu_{s}(CN1)$ (12), $\delta_{op,s}(CO)$ (14), δ_{ip}(ring-2) (10)
752vs			757	766	763	δ_{ip}(ring-2) (45), $\delta_{op,as}(CO)$ (12)
718sh	732vw	732w	730	739	735	$\delta_{op,s}(NH)$ (11), $\delta_{op,s}(CO)$ (70)
	643w	646m	633	643	647	$\nu(N4C6)$ (19), δ_{ip}(ring-1) (51), $\delta_{op,s}(NH)$ (17)
608w 604w	603w	607w	591	619	621	$\nu_{as}(CN1)$ (18), $\delta_{ip,as}(CO)$ (64)
			455	533	542	δ_{ip}(ring-1) (15), $\delta_{op,s}(ND)$ (80)
499m	511w	496vw	403	499	503	$\delta_{op,as}(ND)$ (94)
	407sh 394w	407vw	383	424	405	$\nu_{s}(CN4)$ (22), $\delta_{ip,s}(CO)$ (62)
	357vw		289	344	345	δ_{op}(ring-1) (100)
	288m	291w	258	321	301	$\delta_{ip}(N4C6)$ (74), $\delta_{ip,as}(CO)$ (12)
	245w		211	240	235	$\delta_{op}(N4C6)$ (91)
	181w		153	198	181	$\delta_{op}(N4C6)$ (10), $\delta_{op,as}(CO)$ (10), δ_{op}(ring-2) (79)
			36	190	153	$\tau(N4C6)$ (93)

4.3.2.2. *C=O Vibrations*

The ν(CO) vibrations calculated using model III are in much better agreement with the observed IR and Raman spectra than models I and II, and give values mostly within 20 cm^{-1} of the observed positions. It appears that modelling of C=O---H hydrogen bonds is better represented by the B3-LYP functional than are the NH---O hydrogen bonds, and that inclusion of both implicit and explicit solvation is necessary. The PSPW calculation of the vibrational spectra of solid state urazole accurately predicts that the IR-active components are at higher wavenumber than the Raman-active ones. Solvation model III also gives an accurate prediction of the in-plane and out-o-plane C=O deformations, and gives an accurate prediction of the shifts observed for all C=O vibrations upon deuteration.

4.3.2.3. *Triazolidine Ring Vibrations*

The stretching and in-plane deformation modes of the triazolidine ring give rise to the strongest bands in the Raman spectra of both urazole and 4-methylurazole. In view of the dissimilarity of the bonds within the triazolidine ring it was not considered appropriate to take linear combinations of all five bond stretches and instead we combined the CN stretches in accordance with C_2 symmetry. This procedure was also used for 4-methylurazole, although it does not have a 2-fold axis of symmetry. For ring deformations (in-plane and out-of-plane) it was considered appropriate to take linear combinations in order to remove the 3 in-plane and 3 out-of-plane redundancies. The triazolidine ring vibrations predicted by solvation model III are mostly in very good agreement with experimental band positions and satisfactorily account for the observed deuterium shifts.

Relatively small shifts of the ν(CN) vibrations are observed on deuteration but the ν(NN) vibration appears to shift upwards by ca. 100 cm^{-1} on deuteration. In urazole and 4-methylurazole the ν(NN) coordinate is not significantly mixed with other types of motion and can be attributed to a medium intensity band in the solid state Raman spectra, at 1124 cm^{-1} for urazole and 1115 cm^{-1} for 4-methylurazole. However, upon deuteration NN stretching becomes mixed with other motions, contributing significantly to bands at 1213 and 919 cm^{-1} for urazole, and 1256, 1201 and 941/926 cm^{-1} in 4-methylurazole. The exocyclic ν(NC) vibration in 4-methylurazole does not give rise to a characteristic band and this coordinate is distributed over several vibrations.

4.4. Conclusions

New IR and Raman spectra of urazole and their interpretation using DFT calculations, reveal an excellent fit to the experimental data when hydrogen bonding is taken into account. In order to achieve a satisfactory interpretation of the vibrational spectrum of urazole in aqueous solution the DFT calculations were carried out using a model in which urazole is surrounded by five water molecules, in an endeavour to accurately reproduce the experimental structural and spectroscopic data.

It was ascertained that five water molecules are the minimum required in order to ensure that all of the oxygen and hydrogen atoms of urazole are hydrogen-bonded. The vibrational spectrum of urazole in the solid state, has been modelled using a pseudopotential-plane-wave (PSPW) DFT method. Significantly, for the first time the IR and Raman spectra of 4-methylurazole have been recorded in both the solid state and in aqueous solution, and subsequently, these spectra have also been modelled by DFT calculations.

B3-LYP/cc-pVTZ calculations of urazole and 4-methylurazole provide an excellent fit to the observed IR and Raman spectra obtained in the solid and solution states, provided that hydrogen bonding is taken into account. The assessment of different solvation models indicates that the structure and vibrational spectra of these molecules are best represented by a model incorporating both implicit and explicit solvation. Normal coordinate analysis using the DFT force field has provided detailed band assignments in terms of potential energy distributions. These assignments differ significantly from those published previously, reflecting the importance of hydrogen bonding for both molecules in the solid state and in aqueous solution.

4.5. References

[1] V.M. Kolb, J. P. Dworkin and S. L. Miller, *J. Mol. Evol.*, 1994, **38**, 549.

[2] S.L. Miller, *Orig. Life Evol B.*, 1993, **23-24**, 107.

[3] Y.Y. Kharitonov, B.M. Baloyan and D. G. Batyr, *Russ. J. Inorg. Chem.*, 1982, **27**, 173

[4] Y.Y. Kharitonov, B.M. Baloyan and D. G. Batyr, *Zh. Neorg. Khim.*, 1982, **27**, 305.

[5] R. Gomper, *Chem. Ber.*, 1960, **97**, 198.

[6] M.J. Bausch, B. David, P. Kobrowolski and C. Guadalupe-Fasano, *J. Org. Chem.*, 1991, **56**, 5643.

[7] J. O. Jensen, Spectrochim Acta, 2003, **59A**, 637.

[8] F. Belaj, *Acta Cryst.*, 1992, **C48**, 1088.

[9] J. A. Tenon, M. Carles and J.-P. Aycard, *Acta Cryst.*, 1995, **C51**, 1440.

[10] Gaussian 03, Revision A.1, M. J. Frisch, G. W. Trucks, H. B. Schlegel, G. E. Scuseria, M. A. Robb, J. R. Cheeseman, J. A. Montgomery, Jr., T. Vreven, K. N. Kudin, J. C. Burant, J. M. Millam, S. S. Iyengar, J. Tomasi, V. Barone, B. Mennucci, M. Cossi, G. Scalmani, N. Rega, G. A. Petersson, H. Nakatsuji, M. Hada, M. Ehara, K. Toyota, R. Fukuda, J. Hasegawa, M. Ishida, T. Nakajima, Y. Honda, O. Kitao, H. Nakai, M. Klene, X. Li, J. E. Knox, H. P. Hratchian, J. B. Cross, C. Adamo, J. Jaramillo, R. Gomperts, R. E. Stratmann, O. Yazyev, A. J. Austin, R. Cammi, C. Pomelli, J. W. Ochterski, P. Y. Ayala, K. Morokuma, G. A. Voth, P. Salvador, J. J. Dannenberg, V. G. Zakrzewski, S. Dapprich, A. D. Daniels, M. C. Strain, O. Farkas, D. K. Malick, A. D. Rabuck, K. Raghavachari, J. B. Foresman, J. V. Ortiz, Q. Cui, A. G. Baboul, S. Clifford, J. Cioslowski, B. B. Stefanov, G. Liu, A. Liashenko, P. Piskorz, I. Komaromi, R. L. Martin, D. J. Fox, T. Keith, M. A. Al-Laham, C. Y. Peng, A. Nanayakkara, M. Challacombe, P. M. W. Gill, B. Johnson, W. Chen, M. W. Wong, C. Gonzalez, and J. A. Pople, Gaussian, Inc., Pittsburgh PA, 2003.

[11] A.D. Becke, *J. Chem. Phys.*, 1993, **98**, 5648.

[12] C. Lee, W. Yang and R.G. Parr, Phys. Rev. B, 1988, **37**, 785.

[13] N. Godbout, D.R. Salahub, J. Andzelm and E. Wimmer, *Can. J. Chem.*, 1992, **70**, 560.

[14] M.T. Cances, V. Mennucci and J. Tomasi, *J. Chem. Phys.*, 1997, **107**, 3032.

[15] M. Cossi, N. Rega, G. Scalmani and V. Barone, *J. Comput. Chem.*, 2003, **24**, 669.

[16] Y. Takano and K.N. Houk, *J. Chem. Theory Comput.*, 2005, **1**, 70

[17] V. Barone, M. Cossi, B. Mennucci and J. Tomasi, *J. Chem. Phys.*, 1997, **107**, 3210.

[18] J. A. Schachtschneider, *Vibrational Analysis of Polyatomic Molecules*, Parts V and VI, Technical Report Nos. 231 and 57, Shell Development Co., Houston TX, 1964 and 1965.

[19] S.J. Clark, M.D. Segall, C.J. Pickard, P.J. Hasnip, M.J. Probert, K. Refson, M.C.Z. Payne, *Krist.*, 2005, **220**, 567.

[20] J.P. Perdew, J.A. Chevary, S.H. Vosko, K.A. Jackson, M.R. Pederson, D.J. Singh, C. Fiolhais, *Phys. Rev. B*, 1992, **46**, 6671.

[21] H. J. Monkhorst, J. D. Pack, *Phys. Rev. B*, 1976, **13**, 5188.

[22] P. Ugliengo, D. Viterbo, G. Chiari Z. *Kristallogr.*, 1993, **207**, 9

[23] P. Pulay, G. Fogarasi, F. Pang and J. E. Boggs, *J. Am. Chem. Soc.*, 1979, **101**, 2550.

[24] B.Z. Chowdhry, T.J. Dines, S. Jabeen and R. Withnall, *J. Phys. Chem. A*, 2008, **112**, 10333.

[25] N. Kausar, T.J. Dines, B.Z. Chowdhry and B.D. Alexander, *Phys. Chem. Chem. Phys.*, 2009, **11**, 6389.

5. Vibrational Spectra and Structures of the Anions of Urazole and 4-Methylurazole: DFT Calculations of the Normal Modes and the Influence of Hydrogen Bonding

5.1. Introduction

In the previous chapter the IR and Raman spectra of urazole and 4-methylurazole[1] were interpreted in terms of DFT models taking into account the effects of hydrogen bonding. This Chapter investigates measurements of the IR and Raman spectra of the mono-anions of these species at high pH in aqueous solution, and in the solid state.

The acidic properties of urazole and numerous substituted urazoles, have been reported by Bausch *et al.*[2,3] who established that the pK_a for both urazole and 4-methylurazole is 5.8 in aqueous solution but in DMSO, the $pK_a = 13.1$ for urazole and 12.3 for 4-methylurazole. This being attributed to the much smaller pK_a values in aqueous solution for the stabilization of urazole anions via hydrogen-bonding interactions. Significantly, in the case of urazole the possibility exists of deprotonation at either the N1 or N4 nitrogen atoms; using ^{13}C NMR spectroscopy, Bausch *et al.*[4] show that deprotonation occurs preferentially at N1.

Using a combination of IR and Raman spectroscopy, in conjunction with DFT calculations, the influence of hydrogen bonding on the structures of the urazole and 4-methylurazole anions is investigated, with a view to demonstrating that the vibrational spectra of the urazole anion are consistent with deprotonation at the N1 nitrogen atom, in agreement with the NMR evidence, although the presence of the second tautomer (i.e. deprotonation at N4) is also apparent. Previously, in the study of the parent neutral molecules it was shown that the structures and vibrational spectra were best reproduced by models involving both implicit and explicit solvation, this same procedure has been used in the DFT calculations of the anions.

A literature search, revealed no crystallographic data for the anions of urazole and 4-methylurazole so models were based upon the structures of the parent neutral molecules.[5,6] DFT calculations were performed using the *Gaussian 03* program[7], using the hybrid SCF-DFT method B3-LYP. This incorporates Becke's three parameter hybrid functional8 and the Lee, Yang and Parr correlation functional.[9] As for the neutral molecules, the triple-zeta cc-pVTZ basis set[10] was chosen in preference to Pople-style split-valence basis.

5.2. Calculations

5.2.1. Computing Methodology for Solvated Molecules

Implicit solvation was modelled using the Conductor-like Polarizable Continuum Model (CPCM)[11] and the molecular cavity was defined using the "united atom topological model",[12] *i.e.* by including a sphere around each solute heavy atom with hydrogen atoms enclosed in the sphere of the heavy atom to which they are bonded. Explicit solvation was modelled by the inclusion of five hydrogen-bonded H_2O molecules for the urazole anion and four for the 4-methylurazole anion, such that all the hydrogen bonding sites are occupied. In these models the O•••••H and N•••••H distances were initially set at 1.75 Å prior to geometry optimisation.

The vibrational spectra of these hydrogen-bonded models were calculated at their optimised geometries using the B3-LYP method with the cc-pVTZ basis set. For computation of the potential energy distributions associated with the Vibrational modes, the Cartesian force constants obtained from the *Gaussian 03* output were converted to force constants expressed in terms of internal coordinates and scaled before input to a normal coordinate analysis program derived from those of Schachtschneider[13]. This procedure enabled the force constants associated with the hydrogen-bonded water molecules to be removed. Symmetry-adapted linear combinations of internal coordinates were constructed according to the symmetry elements of the C_2 point group, even though the anions do not actually have C_2 symmetry. IR and Raman spectra were calculated using the Cartesian-based dipole and polarizability derivatives from the B3-LYP/cc-pVTZ calculations, which were transformed to internal coordinates and subsequently to normal coordinates. Simulated spectra were calculated by convolution with a Lorentzian lineshape (f.w.h.m).

5.3. Results and Discussion

5.3.1. DFT Calculations

The atomic numbering scheme for urazole and 4-methylurazole are show in Figure 5.1.

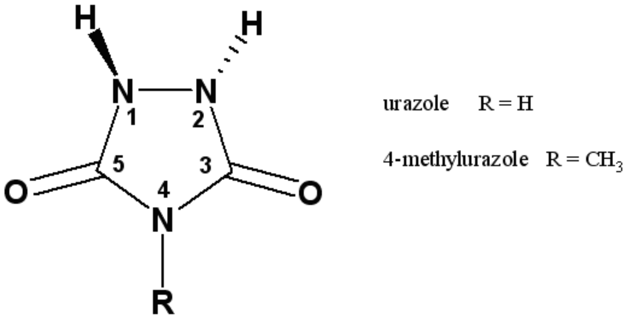

Figure 5.1 The atomic numbering scheme for urazole and 4-methylurazole

B3-LYP/cc-pVTZ calculations on the anions of urazole and 4-methylurazole were performed on hydrogen-bonded models, with urazole deprotonated at either N1 or N4, and 4-methylurazole deprotonated at N1.

5.3.1.1. *Geometry Optimization*

The optimised molecular geometries of the urazole and 4-methylurazole anions with hydrogen-bonded water molecules are shown in Figure 5.2 and the calculated bond lengths and interbond angles are listed in Tables 5.1 and 5.2, together with experimental data. For the two tautomers of the urazole anion it is found that deprotonation is favoured at nitrogen atom N1, with respect to N4, by 2.24 kJ mol^{-1}. This is in accord with the ^{13}C NMR evidence of Bausch *et al*.[4].

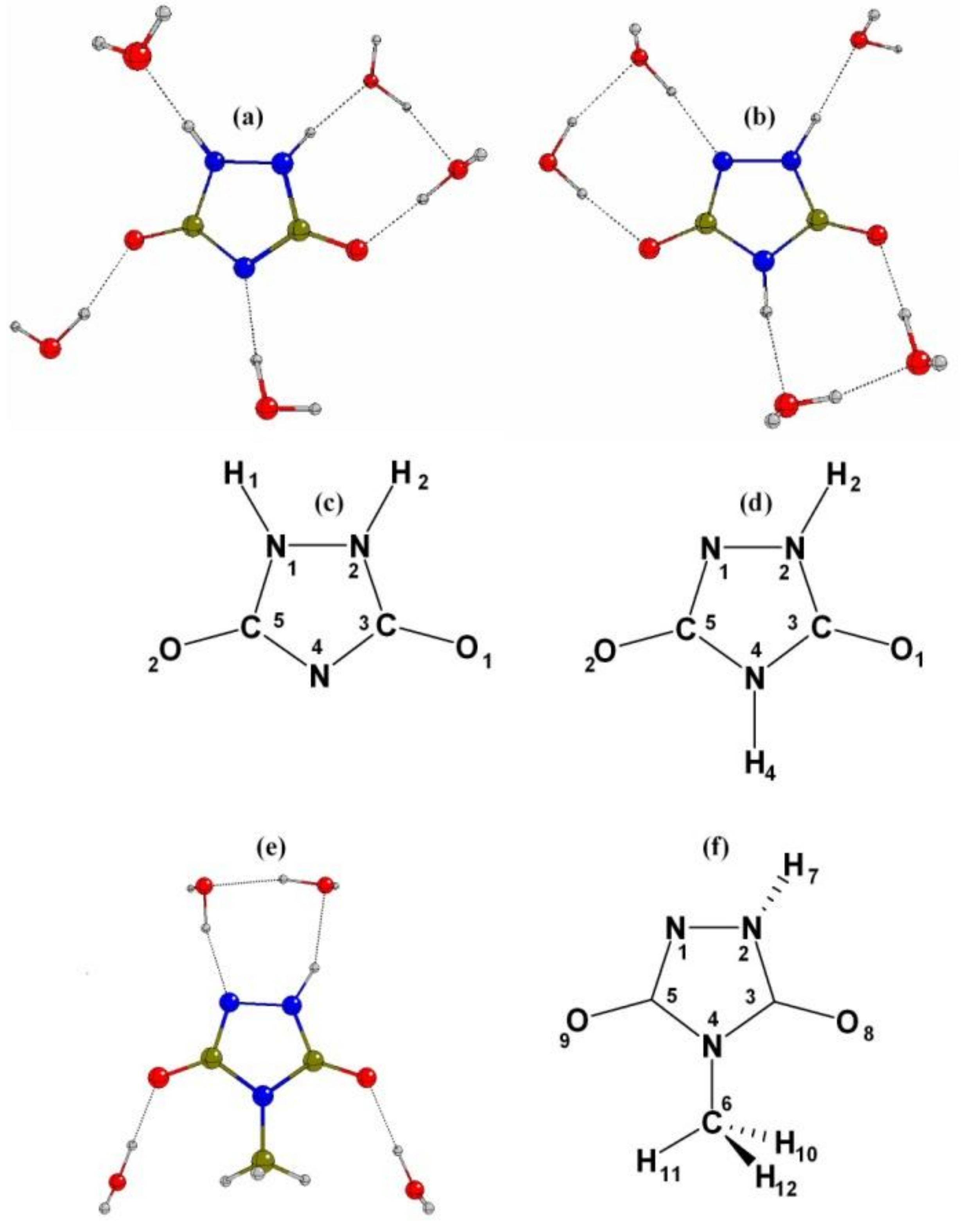

Figure 5.2. Calculated structures of anions and atom numbering schemes.

Table 5.1. Calculated energies and molecular geometries for the urazole anion with five hydrogen-bonded water molecules, deprotonated at either N4 or N1

	deprotonated at N4	deprotonated at N1
E / H	-774.826282156	-774.834706564
Δ*E* / kJ mol^{-1}	2.24	0
r(C3N4)	1.3568	1.3723
r(C3O1)	1.2478	1.2521
r(N1N2)	1.4154	1.4042
r(C3N2)	1.3914	1.3434
r(N2H2)	1.0238	1.0187
r(C5N1)	1.3978	1.3335
r(C5N4)	1.3583	1.4039
r(N1H1)	1.0235	---
r(O1···H)	1.7160	1.7150
r(N4···H)	1.8810	---
r(O2···H)	1.8140	1.8121
r(O···H2)	1.9455	1.8820
r(O2C5)	1.2423	1.2585
r(O···H1)	1.9258	---
r(O···H4)	---	1.9096
r(N4H4)	---	1.0213
r(N1···H)	---	1.8118
θ(N4C3O2)	126.64	128.03
θ(N4C3N2)	110.23	104.27
θ(C3N4C5)	107.04	109.51
θ(O8C3N2)	123.12	127.70
θ(N1N2C3)	105.69	112.65
θ(N1N2H2)	115.00	120.84
θ(N2N1C5)	105.43	105.00
θ(N2N1H1)	113.98	---
θ(C3N2H2)	117.63	126.44
θ(N4C5N1)	110.06	108.56
θ(C5N1H1)	116.06	---
θ(N1C5O2)	121.87	128.41
θ(N4C5O2)	128.07	123.03
θ(C3N4H4)	---	124.81
θ(C5N4H4)	---	125.68

Table 5.2. Calculated molecular geometry for the 4-methylurazole anion with four hydrogen-bonded water molecules, deprotonated at N1

r(C3N4)	1.3805
r(N4C5)	1.4281
r(C3N2)	1.3698
r(N1N2)	1.4223
r(C5N1)	1.3433
r(C6H12)	1.0968
r(C6N4)	1.4444
r(H7N2)	1.0177
r(O8C3)	1.2478
r(O9C5)	1.2546
r(H10C6)	1.0959
r(H11C6)	1.0927
r(O8···H)	2.0008
r(N1···H)	1.6275
r(O9···H)	1.9326
θ(C3N4C5)	109.56
θ(N4C3N2)	104.33
θ(C3N4C6)	125.14
θ(N4C3O8)	127.46
θ(N4C5N1)	108.05
θ(C5N4C6)	124.95
θ(N4C5O9)	122.76
θ(C3N2N1)	111.56
θ(C3N2H7)	120.53
θ(N2C3O8)	128.21
θ(N2N1C5)	105.76
θ(N1N2H7)	115.96
θ(N1C5O9)	129.18
θ(H12C6N4)	111.11
θ(H12C6H10)	108.35
θ(H12C6H11)	109.57
θ(N4C6H10)	110.90
θ(N4C6H11)	107.04
θ(H10C6H11)	109.85

In the absence of X-ray crystallographic structures for these anions the emphasis is on comparison of the computed structures with the corresponding neutral molecules[1]. In the case of urazole the CO distances are lengthened in the anion (from ca. 1.23 to ca. 1.25 Å), while the CN1 and CN2 distances are shortened (from ca. 1.37 to ca. 1.34 Å), reflecting increased double bond character, but the NN distance remains essentially unchanged. The two CN4 distances are markedly different in the anion (1.3723 and 1.4039 Å), for which the latter represents a significant lengthening with respect to neutral urazole. In the case of the 4-methylurazole anion similar behaviour is seen for the CO and CN distances but the NN distance is lengthened with respect to the neutral molecule (from 1.4079 to 1.4223 Å).

The other important differences in the structures of the anions are the planarity of the triazolidine ring, and the planar geometry at nitrogen atoms N2 and N4. The computed ring dihedral angles for both anions are $\leq 0.7^{o}$ whereas the triazolidine ring is calculated to be significantly puckered in the neutral molecules, in agreement with crystal structure data[14,15]. In the neutral molecules there is essentially planar geometry at N4 but pyramidal geometry at N1 and N2, with their hydrogen atoms, respectively, above and below the triazolidine ring. However, for the anions all nitrogen atoms exhibit planar coordination. These observations, together with the differences in bond distances, suggest an increased π contribution to the bonding within the triazolidine ring in the anions, which is supported by the spectroscopic data (*vide infra*).

Table 5.3. Experimental and calculated vibrational spectra of the urazole anion

Experimental			**Calculated**		**Assignments (% p.e.d.s)**
IR solid	**Raman solid**	**Raman soln.**	**deprot. N4**	**deprot. N1**	
3353vw	3417w,br		3344	3395	ν(N2H) (99)
3185w 3046vw	3210w,br		3334	3358	ν(N4H) (99)
2901w					
2976w					
	2834w				
	2732vw				
2672w					
1707m	1705w		1710	1698	ν_{s}(CO) (52), ν_{s}(CN1) (16), δ_{ip}(ring-1) (11)
1622vs 1532sh	1625w,br		1592	1637	ν_{as}(CO) (39), ν_{as}(CN1) (15), δ_{ip}(N4H) (15)
1436s	1439m	1458w	1466	1458	δ_{ip}(N2H) (59)
1409sh	1416w		1439	1430	ν_{s}(CO) (11) ν_{s}(CN4) (28), ν_{s}(CN1) (26), δ_{ip}(N2H) (12), $\delta_{ip,s}$(CO) (12)
1378s 1344w	1368sh 1358sh 1344vs	1391vw	1387	1375	ν_{as}(CO) (26), δ_{ip}(N4H) (67)
1278m	1270w,br	1274m	1262	1275	ν_{as}(CN4) (45), δ_{ip}(N2H) (11), δ_{ip}(ring-2) (14)
1184w 1151sh	1190w 1145w	1103s	1142	1112	ν_{s}(CN4) (14), ν_{s}(CN1) (14), ν(NN) (43)
1097w	1079vs	1082s	1082	1049	ν_{as}(CN4) (56), ν(NN) (14)
1054w	1036vs	1043s			
1007s	1006m,br	1012vs	1019	1004	ν_{s}(CN4) (15), ν_{as}(CN4) (22), ν_{s}(CN1) (15), ν(NN) (21) , δ_{ip}(ring-1) (19)
877m	890vw		820	811	ν_{as}(CO) (15), ν_{as}(CN1) (13), δ_{ip}(ring-2) (67)
833sh 801vs 791sh	845vw 835vw 787w	804w	806	796	$\delta_{op,as}$(CO) (47), δ_{op}(ring-2) (44)
755s 738sh	771w		793	728	$\delta_{op,s}$(CO) (62), δ_{op}(ring-1) (29)
715s 696s	705w	697s	756	701	δ_{op}(N4H) (61), δ_{op}(N2H) (22), $\delta_{op,s}$(CO) (19), $\delta_{op,as}$(CO) (28)
679sh	667w		663	692	ν_{s}(CO) (19), ν_{s}(CN1) (11), δ_{ip}(ring-1) (56)
	633 w	610w,br	636	631	$\delta_{ip,as}$(CO) (89)
	596w				
	537w,br		626	533	δ_{op}(N4H) (30), δ_{ip}(N2H) (61)
	489w	496sh,br			
		435m,br	451	433	ν_{s}(CN1) (20), $\delta_{ip,s}$(CO) (70)
	325w,br		351	341	δ_{op}(N2H) (11), $\delta_{op,s}$(CO) (11), δ_{op}(ring-1) (75)
	247w		226	212	$\delta_{op,as}$(CO) (17), δ_{op}(ring-2) (84)

a. Assignments refer to the model with deprotonation at N1, except for any enclosed in square brackets, which refer to the model with deprotonation at N4.

Table 5.4. Experimental and calculated vibrational spectra of the urazole-*d*$_2$ anion

Experimental		**Calculated**		**Assignments (% p.e.d.s)**[a.]
IR solid	**Raman solid**	**deprot. N4**	**deprot. N1**	
2564w 2513w		2456	2505	ν(N2D) (95)
2486w 2388w	2475w,br 2375w,br	2448	2475	ν(N4D) (95)
2355vw				
2282w				
1711sh 1696s	1677w	1702	1689	ν_s(CO) (60), ν_s(CN1) (19), δ_{ip}(ring-1) (12)
1623sh 1593sh 1585vs	1512w	1583	1608	ν_{as}(CO) (57), ν_{as}(CN1) (18)
1426s	1436vw,br 1372sh	1385	1424	ν_s(CN4) (33), ν_s(CN1) (38), $\delta_{ip,s}$(CO) (17)
1314m	1348s 1331s		1317	ν_{as}(CN4) (53), δ_{ip}(N2D) (11), δ_{ip}(ring-2) (16)
	1276m 1270sh	1264		[ν_{as}(CN1) (44), ν_{as}(CN4) (28), δ_{ip}(N1D) (11)]
1241vw 1218w 1198vw 1191vw	1182vw	1198	1213	ν_{as}(CO) (12), ν_{as}(CN4) (31), ν(NN) (17), δ_{ip}(N4D) (14), δ_{ip}(N2D) (13)
1142w	1080vs 1069sh	1183	1171	ν_{as}(CN4) (13), ν(NN) (27), δ_{ip}(N4D) (24)
	1038w 1013m	984	1003	ν_s(CN4) (26), ν_s(CN1) (25), δ_{ip}(N2D) (16), δ_{ip}(ring-1) (21)
995sh 990m 955s	991s 975w,sh	982	966	ν(NN) (34), δ_{ip}(N4D) (14), δ_{ip}(N2D) (27)
896w 877m	919vw	968	892	ν_{as}(CN4) (34), δ_{ip}(N4D) (27), δ_{ip}(N2D) (13), δ_{ip}(ring-2) (17)
780s	817w	813	786	ν_{as}(CO) (13), ν_{as}(CN1) (17), δ_{ip}(ring-2) (53)
760s	763w	781	775	$\delta_{op,as}$(CO) (76), δ_{op}(ring-2) (30)
690s	707s	765	722	$\delta_{op,s}$(CO) (82), δ_{op}(ring-1) (20)
		715	687	ν_s(CO) (19), ν_s(CN1) (10), δ_{ip}(ring-1) (58)
		606	598	$\delta_{ip,as}$(CO) (81)
		562	521	δ_{op}(N4D) (81), δ_{op}(N2D) (27)
		493	430	ν_s(CN1) (20), $\delta_{ip,s}$(CO) (69)
		449	413	δ_{op}(N4D) (25), δ_{op}(N2D) (36), δ_{op}(ring-1) (31)
		330	333	δ_{op}(N2D) (37), δ_{op}(ring-1) (48)
		226	209	$\delta_{op,as}$(CO) (16), δ_{op}(ring-2) (85)

a. Assignments refer to the model with deprotonation at N1, except for any enclosed in square brackets, which refer to the model with deprotonation at N4.

Table 5.5. Experimental and calculated vibrational spectra of the 4-methylurazole anion

IR solid	**Raman solid**	**Raman soln.**	**calc.**	**Assignments (% p.e.d.s)**
3100m,br 2950w,br	3280w,br		3423	$\nu(N1H)$ (99)
			3141	$\nu_{as}(CH_3)$ (100)
	2955m	2964m	3103	$\nu_s(CH_3)$ (21), $\nu_{as}(CH_3)$ (79)
	2882w	2880w,br	3026	$\nu_s(CH_3)$ (79), $\nu_{as}(CH_3)$ (17)
1678m			1708	$\nu_s(CO)$ (56), $\nu_s(CN1)$ (18), δ_{ip}(ring-1) (12)
1626sh 1598vs	1590w		1623	$\nu_{as}(CO)$ (49), $\nu_{as}(CN1)$ (21)
1541vs			1521	$\delta_{as}(CH_3)$ (75)
			1505	$\delta_s(CH_3)$ (33), $\delta_{as}(CH_3)$ (35)
1481vs	1495w	1489w	1493	$\delta_s(CH_3)$ (18), $\delta_{as}(CH_3)$ (60)
1460sh	1451vw	1460vw,br	1451	$\nu_s(CO)$ (13), $\delta_{ip}(N1H)$ (65)
1418sh 1396sh	1384w	1409vw	1423	$\nu(NMe)$ (10), $\nu_s(CN4)$ (21), $\delta_s(CH_3)$ (38)
1295m	1285m	1288m	1297	$\nu(NMe)$ (17), $\nu_s(CN4)$ (34)
1268m	1254s	1265s	1259	$\nu(NMe)$ (15), $\nu_{as}(CN4)$ (19), $\rho_{ip}(CH_3)$ (20)
1223m			1251	$\delta_{ip}(N1H)$ (11), $\nu_{as}(CN1)$ (33)
1164sh 1122m	1150vw		1161	$\rho_{ip}(CH_3)$ (35), $\rho_{op}(CH_3)$ (55)
1066w 1029m	1085vw 1040w	1082w	1078	$\nu(NN)$ (72)
980w	981w	985w	992	$\nu_{as}(CN4)$ (55), $\rho_{ip}(CH_3)$ (19), $\rho_{op}(CH_3)$ (14)
898m,sh 877m	816m	817sh	820	$\delta_{as}(CO)$ (14), δ_{ip}(ring-2) (70)
813vs	810s		785	$\nu(NMe)$ (26), $\nu_s(CN4)$ (26), $\nu_s(CN1)$ (14), $\nu(NN)$ (10)
796m	779vs	786vs	776	$\delta_{op,as}(CO)$ (72), δ_{op}(ring-2) (25)
761s 723m 696w	718vw	746vw	724	$\delta_{op,as}(CO)$ (77), δ_{op}(ring-1) (25)
645vs	658m		669	$\delta_{ip,as}(CO)$ (69)
	634w 627w	637w	637	$\nu(NMe)$ (14), $\nu_s(CO)$ (11), δ_{ip}(ring-1) (60)
			569	$\delta_{op}(N1H)$ (90), $\delta_{op,s}(CO)$ (13)
	415vw 393vw	408w	405	$\nu_s(CN4)$ (24), $\delta_{ip,s}(CO)$ (63)
	300vw		349	$\delta_{op}(N1H)$ (11), δ_{op}(ring-1) (72)
	286vw		313	$\delta_{ip}(NMe)$ (67), $\delta_{ip,s}(CO)$ (11)
			229	$\delta_{op}(NMe)$ (44), $\delta_{op,s}(CO)$ (13), δ_{op}(ring-2) (40)
			172	$\tau(NMe)$ (85)
			163	$\delta_{op}(NMe)$ (46), δ_{op}(ring-2) (42)

Table 5.6. Experimental and calculated vibrational spectra of the 4-methylurazole anion-d_1

IR solid	Raman solid	Calc.	Assignments (% p.e.d.s)
		3141	ν_{as}(CH$_3$) (100)
2930w	2956m	3103	ν_{s}(CH$_3$) (21), ν_{as}(CH$_3$) (79)
2880vw,br	2880w,br	3027	ν_{s}(CH$_3$) (79), ν_{as}(CH$_3$) (17)
2510w 2460w,br 2360w	2520w 2488w 2455w 2385w	2523	ν(N1D) (99)
1673s	1726vw 1687vw	1704	ν_{s}(CO) (59), ν_{s}(CN1) (19), δ_{ip}(ring-1) (13)
1599vs	1587w	1618	ν_{as}(CO) (55), ν_{as}(CN1) (20)
1550sh	1548vw	1521	δ_{as}(CH$_3$) (75)
		1505	δ_{s}(CH$_3$) (32), δ_{as}(CH$_3$) (36)
1475s	1494w	1493	δ_{s}(CH$_3$) (20), δ_{as}(CH$_3$) (58)
1426sh 1400w	1435vw 1403vw	1423	ν(NMe) (10), ν_{s}(CN4) (23), δ_{s}(CH$_3$) (41)
	1314sh	1323	ν_{as}(CN1) (48), δ_{ip}(N1D) (10), δ_{ip}(ring-2) (16)
1307m	1309s	1287	ν(NMe) (21), ν_{s}(CN1) (34)
1240w	1254vs 1248sh	1258	ν_{as}(CN4) (18), ρ_{ip}(CH$_3$) (27), ρ_{op}(CH$_3$) (14)
		1163	ρ_{ip}(CH$_3$) (22), ρ_{op}(CH$_3$) (48)
1139w	1146w	1153	ν(NN) (29), δ_{ip}(N1D) (17), ρ_{ip}(CH$_3$) (13)
1066w 1038w 998sh 991m	990w	1006	ν(NN) (16), ν_{as}(CN4) (42), ρ_{ip}(CH$_3$) (14), ρ_{op}(CH$_3$) (10)
913w 891 m 879sh	904vw	934	ν(NN) (19), δ_{ip}(N1D) (46), ν_{as}(CN4) (11)
800vs	810s	811	δ_{as}(CO) (13), δ_{ip}(ring-2) (71)
770sh	799s	780	ν(NMe) (24), ν_{s}(CN4) (25), ν_{s}(CN1) (14)
758vs	779vs 773sh	773	$\delta_{op,as}$(CO) (71), δ_{op}(ring-2) (22)
723vw	711w	720	$\delta_{op,as}$(CO) (83), δ_{op}(ring-1) (19)
648vs	654m	651	ν(NMe) (11), $\delta_{ip,as}$(CO) (43), δ_{ip}(ring-1) (24)
	619w 609m	632	$\delta_{ip,as}$(CO) (26), δ_{ip}(ring-1) (43)
		429	δ_{op}(N1D) (59), $\delta_{op,s}$(CO) (10), δ_{op}(ring-1) (31)
		404	ν_{s}(CN4) (24), $\delta_{ip,s}$(CO) (63)
		340	δ_{op}(N1D) (40), δ_{op}(ring-1) (43)
	306w 289vw	312	δ_{ip}(NMe) (65), $\delta_{ip,s}$(CO) (10)
		229	δ_{op}(NMe) (46), $\delta_{op,s}$(CO) (13), δ_{op}(ring-2) (38)
		172	τ(NMe) (85)
		163	δ_{op}(NMe) (45), δ_{op}(ring-2) (42)

5.3.2. Vibrational Assignments

The urazole anion has 21 vibrations and the 4-methylurazole anion has 33 vibrations. Although both anions have C_1 symmetry, symmetry-adapted coordinates were constructed assuming two-fold symmetry, resulting in symmetric and antisymmetric combinations for most internal coordinates. The in-plane and out-of-plane deformation coordinates of the 5-membered ring (see Table 4.3 previous chapter), were combined according to the recommendations of Pulay[16].

Experimental Raman (solid state and aqueous solution) and solid-state IR spectra of urazole are shown in Figures 5.3 and 5.4, together with the spectra computed for the two alternative models (i.e. deprotonation at N1 or N4), and for 4-methylurazole in Figures 5.7 and 5.8. The corresponding spectra for the urazole-d_2 anion are shown in Figures 5.5 and 5.6, and for the 4-methylurazole-d_1 anion in Figures 5.9 and 5.10. Experimental and calculated band positions, with band assignments listed as potential energy distributions (p.e.d.s), are given in Table 5.3 for the urazole anion, Table 5.4 for the urazole-d_2 anion, Table 5.5 for the 4-methylurazole anion and Table 5.6 for the 4-methylurazole-d_1 anion. Discussion of the band assignments for all of these species is divided into consideration of the NH, CO and ring modes. In the case of the urazole anion we focus attention on the differences between the computed spectra for the two models (i.e. deprotonation at either N1 or N4), and show that the experimental spectra provide confirmation that deprotonation occurs at N1, see Figure 5.3.

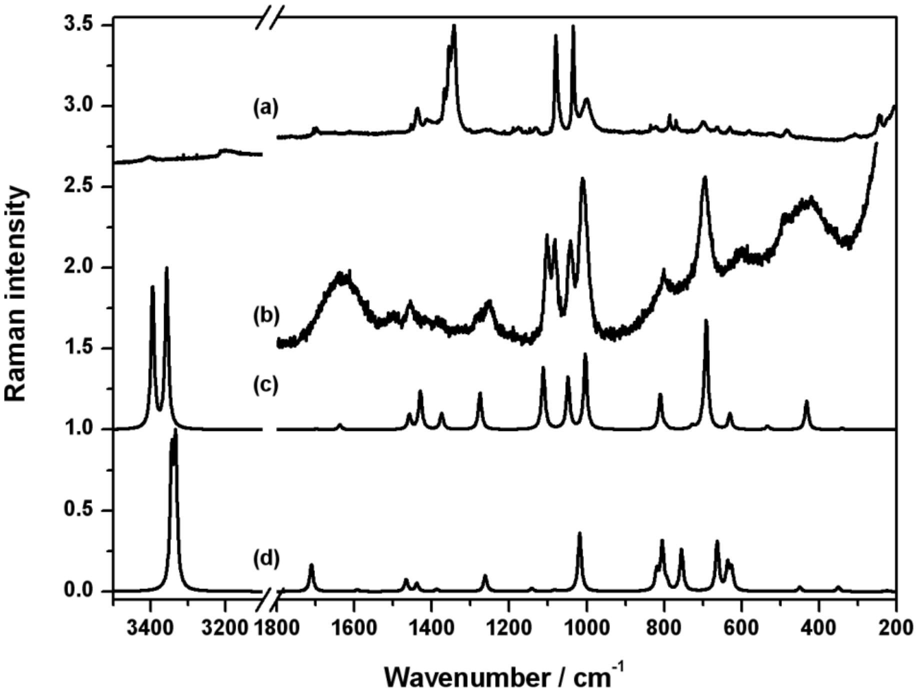

Figure 5.3. Experimental Raman spectra of (a) the urazole anion (solid state) and (b) an aqueous solution of the urazole anion, and calculated Raman spectra: (c) deprotonated at N1 and (d) deprotonated at N4.

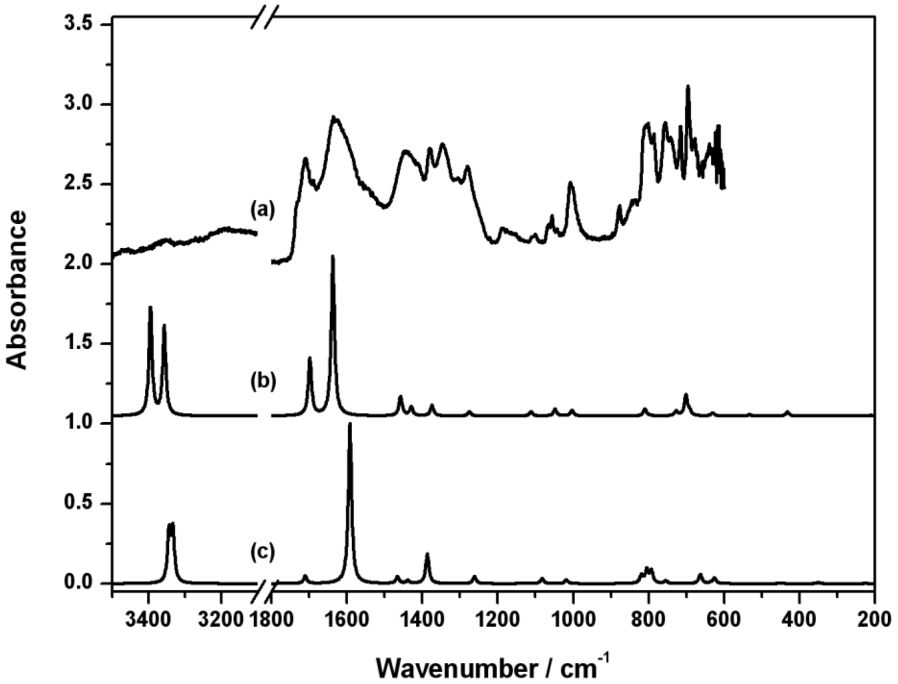

Figure 5.4. Experimental IR spectrum the urazole anion (solid state) (a), and calculated IR spectra: (b) deprotonated at N1 and (c) deprotonated at N4.

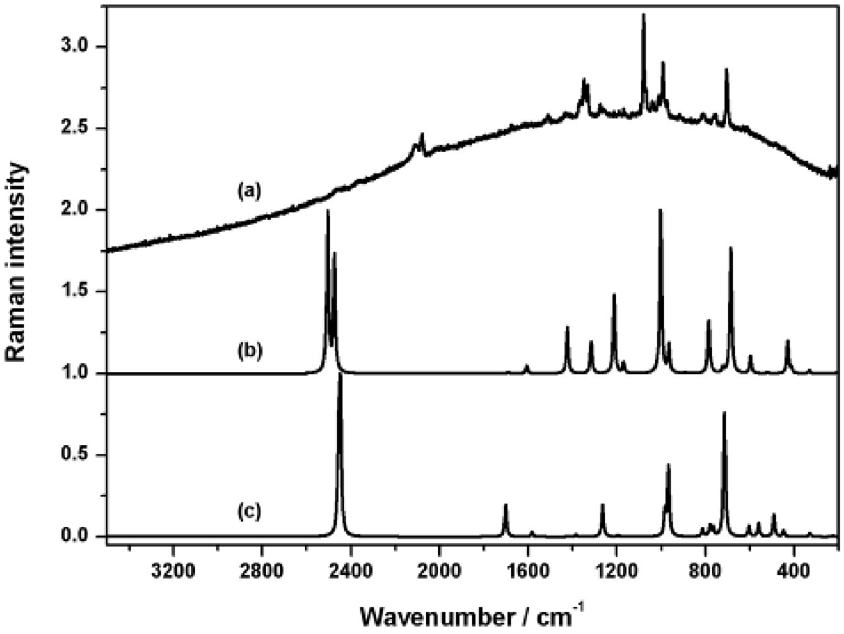

Figure 5.5. Experimental Raman spectrun of the urazole anion-d$_2$ (solid state) (a) and calculated Raman spectra: (b) deprotonated at N1 and (c) deprotonated at N4.

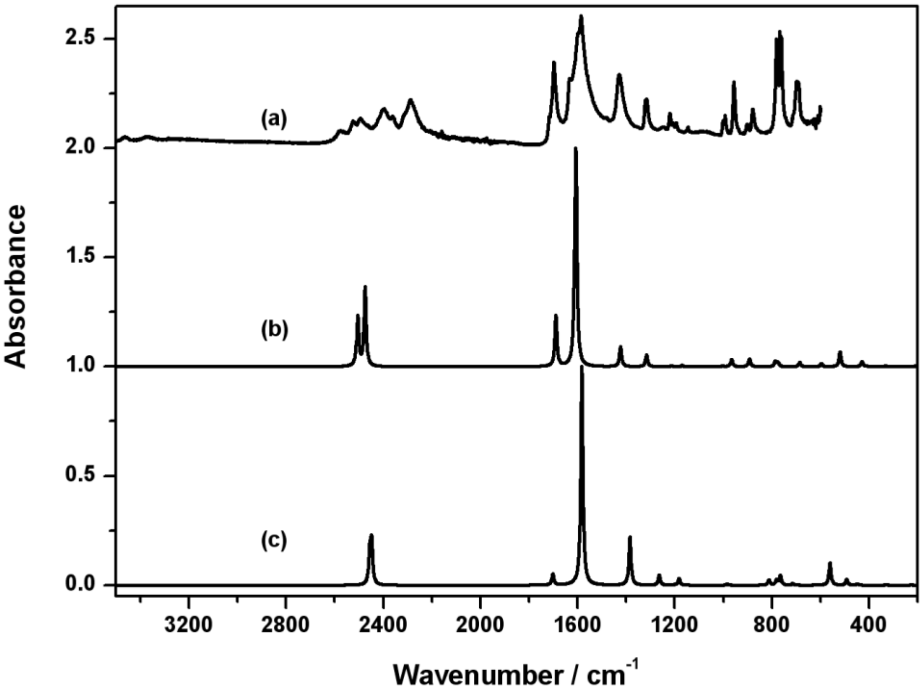

Figure 5.6. Experimental IR spectrum the urazole anion-d$_2$ (solid state) (a), and calculated IR spectra: (b) deprotonated at N1 and (c) deprotonated at N4.

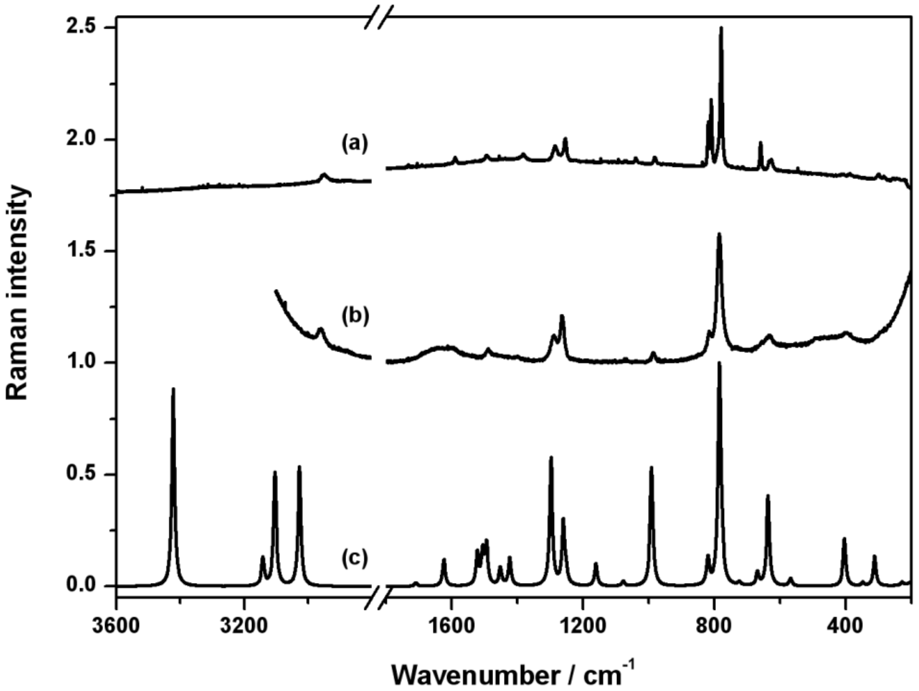

Figure 5.7. Experimental Raman spectra of (a) the 4-methylurazole anion (solid state) and (b) an aqueous solution of the urazole anion, and (c) calculated Raman spectrum.

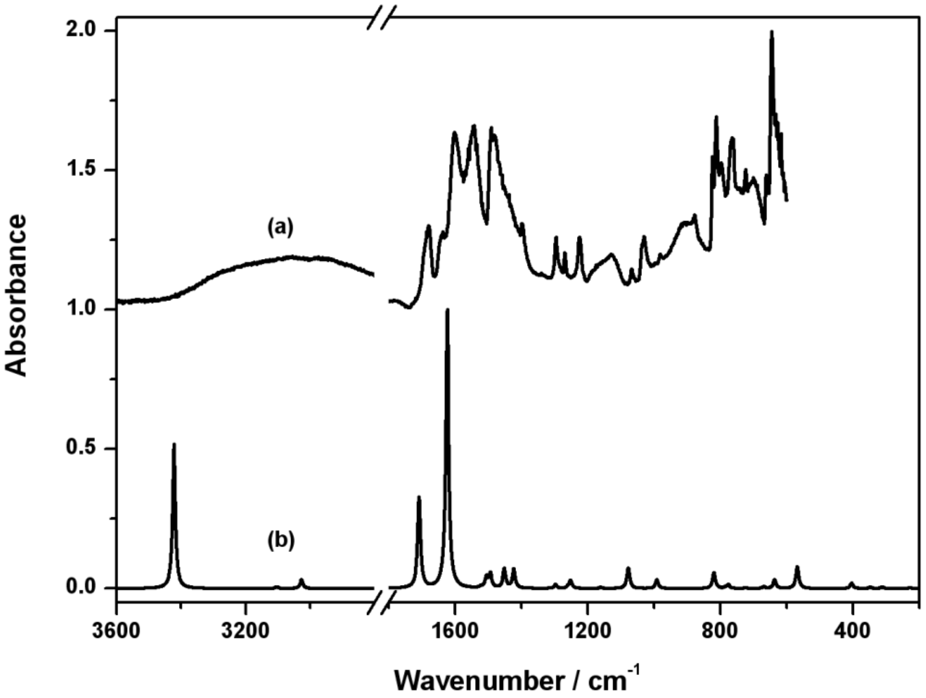

Figure 5.8. Experimental IR spectrum of the 4-methylurazole anion (solid state) (a), and (b) calculated IR spectrum.

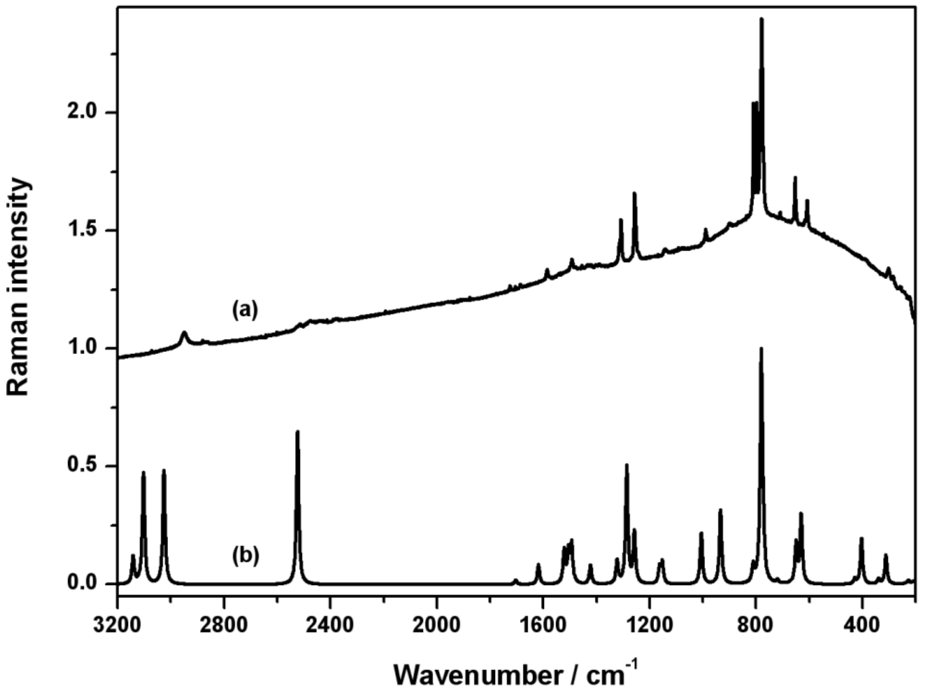

Figure 5.9. Experimental Raman spectrun of the 4-methylurazole anion-d_2 (solid state) (a) and (b) calculated Raman spectrum.

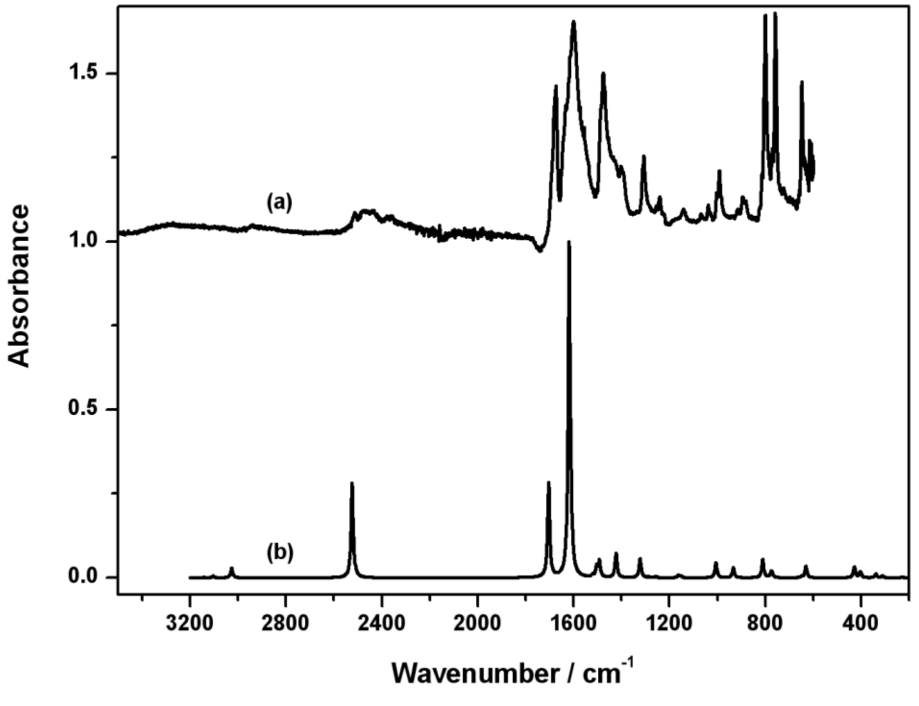

Figure 5.10. Experimental IR spectrum of the 4-methylurazole anion-d_2 (solid state) (a) and (b) calculated IR spectrum.

5.3.2.1. *NH Vibrations*

The ν(NH) vibrations are observed to span the range 3100-3400 cm^{-1} in the solid-state spectra for both anions, as expected for NH groups in strong hydrogen bonding, shifting to 2375-2520 cm^{-1} upon *N*-deuteration. These could not be observed in the aqueous solution Raman spectra, due to their weakness and breadth. For the two models of the urazole anion it is found that the two ν(NH) modes are more widely spaced for deprotonation at N1, in contrast to N4, in agreement with experimental data, although the observed wavenumber difference is significantly larger than the computed value. Surprisingly, the computed value for the higher wavenumber ν(NH) mode, i.e. ν(N2H), is comparable with the experimental band position, notwithstanding that the computed value refers to the harmonic vibration and that ν(NH) vibrations typically have anharmonicities of around 200 cm^{-1}. It appears therefore that the lowering of ν(N2H) attendant upon hydrogen bonding has actually compensated for the anharmonicity of this mode, suggesting that the computed N2H••••O hydrogen bond strength, admittedly for an aqueous solution model, is stronger than occurs in the solid state.

Calculated values for in-plane and out-of-plane NH deformations are in good agreement with experimental data for the N1-deprotonated urazole anion model and for the 4-methylurazole anion. Although the N1- and N4-deprotonated urazole anion models show little difference for the in-plane NH modes, it is found that for the N4-deprotonated model the predicted δ_{op}(NH) band wavenumbers are much higher than their experimental values. For both anions, upon deuteration the ND deformation motions become distributed over several normal coordinates.

5.3.2.2. *C=O Vibrations*

We have combined the CO stretching and deformation coordinates into symmetric and antisymmetric combinations; the justification for this is the similarity in the two CO bond distances, i.e. within 0.006 Å for the urazole anion, and within 0.007 Å for the 4-methylurazole anion. Their distances are marginally longer than those for the neutral molecules, reflecting slightly less than double bond character. The predictions of the ν(CO) vibrations are in good agreement with experimental data and the calculations indicate that these modes are not sensitive to the position of deprotonation in the case of the urazole anion. For both anions ν_s(CO) is about 80 cm^{-1} higher than ν_{as}(CO) and these vibrations are little altered upon deuteration.

The predicted values of the in-plane and out-of-plane CO deformations are also in good agreement with the observed IR and Raman spectra. The symmetric and antisymmetric δ_{ip}(CO) modes are separated by around 200 cm^{-1} and their predicted positions are not sensitive to the position of deprotonation in the case of the urazole anion. However, for the δ_{ip}(CO) vibrations the separation between the symmetric and antisymmetric modes is much smaller for deprotonation at N4 (13 cm^{-1}, increasing to 16 cm^{-1} on deuteration), whereas the predicted separation for deprotonation at N1 is 68 cm^{-1} (decreasing to 53 cm^{-1} on deuteration), in agreement with experimental observations.

5.3.2.3. *Triazolidine Ring Vibrations*

In view of the dissimilarity of the bonds within the triazolidine ring it was not considered appropriate to take linear combinations of the five bond stretches and instead we took symmetric and antisymmetric combinations of the CN stretches for both anions, although the anions do not actually possess C_2 symmetry. For ring deformations (in-plane and out-of-plane) linear combinations were obtained in order to remove the 3 in-plane and 3 out-of-plane redundancies. The stretching and in-plane deformation modes of the triazolidine ring actually give rise to the strongest bands in the Raman spectra of both anions, and their assignment is straightforward by comparison of experimental and calculated spectra. However, in the 1000-1100 cm^{-1} region there is an additional band in the IR and Raman spectra of the urazole anion, which could be assigned to a triazolidine ring stretching vibration of the tautomer where deprotonation is at N4. This is, however, in contradiction to the NMR evidence and the aforementioned behaviour of the vibrations of the CO and NH groups. The vibration in question appears as a very strong band in the solid state Raman spectrum at 1079 cm^{-1} and as a weak band in the IR at 1097 cm^{-1}, where the wavenumber difference is ascribed to factor group splitting. On deuteration this vibration is upshifted due to coupling with δ_{ip}(ND) motion and appears as a medium intensity band in the solid state Raman band at 1276 cm^{-1} (a weak shoulder at 1270 cm^{-1} is attributed to factor group splitting). No other triazolidine ring vibrations can be confidently assigned to this second tautomer and the presence of this particular band is attributed to its intensity, especially in the Raman spectrum.

In the 4-methylurazole anion the bands in this region can all be assigned to a single species, although here there is also evidence for factor group splitting in the solid state spectra.

5.4. Conclusions

In this study we have shown that B3-LYP/cc-pVTZ calculations of the urazole and 4-methylurazole mono-anions provide an excellent fit to the observed IR and Raman spectra obtained in the solid and solution states, provided that hydrogen bonding is taken into account. Indeed it is likely that hydrogen bonding provides stability to the anions. Normal coordinate analysis for the 4-methylurazole anion, using the computed DFT force constants, has provided straightforward and detailed band assignments in terms of potential energy distributions. In the case of the urazole anion the interpretation of the vibrational spectrum is less straightforward because of the possible existence of two tautomers corresponding to deprotonation of urazole at either N1 or N4. What in fact is remarkable is that most of the vibrational spectrum (both IR and Raman) can be assigned to bands of a single tautomer, resulting from deprotonation at N1, in agreement with earlier ^{13}C NMR data. Nevertheless the observation of an additional triazolidine ring stretching vibration, which appears as a strong band in the Raman spectrum, and is firmly supported by the DFT calculations, provides clear evidence for the presence of the second tautomer in both aqueous solution and the solid state.

5.5. References

[1] J.P. Ryall, T.J. Dines, B.Z. Chowdhry, S.A. Leharne, R. Withnall, *Chem. Phys.*, 2010, **373** 219.

[2] M.J. Bausch, D. Selmarten, R. Gostowski, P. Dobrowolski, *J. Phys. Org. Chem.*, 1991, **4**, 67.

[3] M.J. Bausch, B. David, P. Dobrowolski, V. Prasad, *J. Ora. Chem.*, 1990, **55**, 5806.

[4] M.J. Bausch, B. David, P. Dobrowolski, C. Guadalupe-Fasano, R. Gostowski, D. Selmarten, V. Prasad, A. Vaughn, L.-H. Wang, *J. Org. Chem.*, 1991, **56**, 5643.

[5] F. Belaj, *Acta Cryst.*, 1992, **C48**, 1088.

[6] J.A. Tenon, M. Carles, J.-P. Aycard, *Acta Cryst.*, 1995, **C51**, 1440.

[7] M.J. Frisch, G.W. Trucks, H.B. Schlegel, G.E. Scuseria, M.A. Robb, J.R. Cheeseman, J.A. Montgomery, Jr., T. Vreven, K.N. Kudin, J.C. Burant, J.M. Millam, S.S. Iyengar, J. Tomasi, V. Barone, B. Mennucci, M. Cossi, G. Scalmani, N. Rega, G.A. Petersson, H. Nakatsuji, M. Hada, M. Ehara, K. Toyota, R. Fukuda, J. Hasegawa, M. Ishida, T. Nakajima, Y. Honda, O. Kitao, H. Nakai, M. Klene, X. Li, J.E. Knox, H.P. Hratchian, J.B. Cross, C. Adamo, J. Jaramillo, R. Gomperts, R.E. Stratmann, O. Yazyev, A.J. Austin, R. Cammi, C. Pomelli, J.W. Ochterski, P.Y. Ayala, K. Morokuma, G.A. Voth, P. Salvador, J.J. Dannenberg, V.G.

Zakrzewski, S. Dapprich, A.D. Daniels, M.C. Strain, O. Farkas, D.K. Malick, A.D. Rabuck, K. Raghavachari, J.B. Foresman, J.V. Ortiz, Q. Cui, A.G. Baboul, S. Clifford, J. Cioslowski, B.B. Stefanov, G. Liu, A. Liashenko, P. Piskorz, I. Komaromi, R.L. Martin, D.J. Fox, T. Keith, M.A. Al-Laham, C.Y. Peng, A. Nanayakkara, M. Challacombe, P.M.W. Gill, B. Johnson, W. Chen, M.W. Wong, C. Gonzalez, J.A. Pople, Gaussian 03, Revision E.01, Gaussian, Inc., Pittsburgh PA, 2007.

[8] A.D. Becke, *J. Chem. Phys.*, 1993, **98**, 5648.

[9] C. Lee, W. Yang, R.G. Parr, *Phys. Rev. B*, 1988, **37**, 785.

[10] T.H. Dunning, *J. Chem. Phys.*, 1989, **90**, 1007.

[11] M. Cossi, N. Rega, G. Scalmani, V. Barone, *J. Comput. Chem.*, 2003, **24**, 669.

[12] V. Barone, M. Cossi, B. Mennucci, J. Tomasi, *J. Chem. Phys.*, 1997, **107**, 3210.

[13] J.A. Schachtschneider, *Vibrational Analysis of Polyatomic Molecules*, Parts V and VI, Technical Report Nos. 231 and 57, Shell Development Co., Houston TX, 1964 and 1965.

[14] F. Belaj, *Acta Cryst.*, 1992, **C48**, 1088.

[15] J.A. Tenon, M. Carles, J.-P. Aycard, *Acta Cryst.*, 1995, **C51**, 1440.

[16] P. Pulay, G. Fogarasi, F. Pang, J.E. Boggs, *J. Am. Chem. Soc.*, 1979, **101**, 2550.

6. Vibrational Spectroscopy and DFT Calculations of N,N'–Dicyclohexylcarbodiimide

6.1. Introduction

N, N'-dicyclohexylcarbodiimide (DCC, Figure 6.1.) is a widely used laboratory reagent, e.g. as a carboxyl group activating agent in peptide synthesis[1], and for investigating biochemical systems[2]. More recently carbodiimide chemistry has been employed for the functionalisation of carbon nanotubes[3,4] and gold nanoparticles[5]. No X-ray crystal structure of DCC has been reported, presumably because of the difficulty in obtaining diffraction quality crystals. It is not therefore known whether DCC has a *cis* or skew C_2 structure with a linear of nonlinear NCN group, or a *trans* C_i structure with linear NCN group. For this reason we undertook a detailed study of the IR and Raman spectra of DCC, supported by DFT calculations, for the purposes of relating structural and vibrational spectral characteristics.

The IR and Raman spectra of DCC have not previously been reported, although it is well established that 1,3-dialkylcarbodiimides exhibit an intense ν_{as}(N=C=N) band in the IR in the region 2100-2150 cm^{-1} [6] and a ν_s(N=C=N) band in the Raman spectrum near 1460 cm-1 [7]. Microwave spectroscopic studies of the parent molecule, carbodiimide (HN=C=CH) [8], have revealed that it has a C_2 structure with r(C=N) = 1.0074 Å, θ(NCN) = 170.63°, and τ(HN---NH) = 88.98°. In an IR and Raman study of 1,3-dimethylcarbodiimide Rapi and Sbrana[9] established that the vibrational spectra could be interpreted in terms of C_2 symmetry. The IR and Raman spectra of disilylcarbodiimide have been reported[10] and have recently been analyzed in terms of a nonlinear C_2 structure using MP2 and B3-LYP methods[11]. For that species the symmetric and antisymmetric N=C=N stretches are about 100 cm^{-1} higher than in dialkylcarbodiimides.

It appears that a nonlinear C_2 structure may also be probable for DCC, there is also the possibility that the bulky cyclohexyl groups may lead to greater stability of a *trans* C_i structure. It has been established by ^{1}H NMR[12] that the carbodiimido group exerts a significant preference for the equatorial position on the cyclohexyl ring. In this Chapter the results of DFT calculations for C_2 and C_i structures with equatorial cyclohexyl rings are given and compared to the IR and Raman spectra in both solid and solution states, which support the argument in favour of a C_2 structure.

6.2. DFT Calculations

Preliminary calculations at a lower level (cc-pVDZ basis set) revealed that a non-symmetric structure (i.e. C_1 symmetry) had only marginally lower energy than the C_2 structure (<1 kJ mol-1), with almost identical bond distances and angles, and dihedral angles. Models with C_{2v} and C_{2h} symmetry were also considered but rejected because these had much higher energies and exhibited multiple vibrations with imaginary wavenumbers, indicating that these are not stable geometries.

The vibrational spectra of the equatorial *trans* (C_i) and *cis* (C_2) models were calculated at their optimised geometries and for computation of the potential energy distributions (p.e.d.s) associated with the vibrational modes, the Cartesian force constants obtained from the *Gaussian03*[13] output were converted to force constants expressed in terms of internal coordinates. Scaling was applied to the force constants before input to a normal coordinate analysis program derived from those of Schachtschneider.[14] In the DFT calculations the following scale factors were chosen to give the best fit to the experimental data: 0.915 (CH stretches), 0.91 (C=N stretches), 0.93 (CH deformations), 0.98 (all others). IR and Raman intensities were computed from the Cartesian dipole and polarizability derivatives of the *Gaussian03* output by transformation to internal coordinates and subsequently to normal coordinates.[15] These intensities, which are necessarily not the same as the Raman scattering activities provided in the *Gaussian03* output, were convoluted with a Lorentzian function (f.w.h.m. 10 cm^{-1}) for direct comparison with measured spectra.

6.3. Results and Discussion

6.3.1. DFT Calculations

Details of the calculations are listed in Table 6.1.

Table 6.1. Details of the computed DCC models

Symmetry	**Cyclohexane conformation**	N_{imag} **a.**	**Energy / H**	**Δ*E* / kJ mol^{-1}**
C_i	axial	1 (a_u)	-618.345421742	29.99
C_2	axial	0	-618.352668091	10.96
C_i	equatorial	2 ($2a_u$)	-618.347645005	24.15
C_2	equatorial	0	-618.356843192	0.00

a. N_{imag} is the number of computed vibrations with imaginary wavenumbers. Note that $N_{imag} = 1$ corresponds to a transition point but $N_{imag} > 1$ does not correspond to a stationary state on the potential energy surface.

The atom numbering scheme for DCC used in the DFT calculations is shown in Figure 6.1.

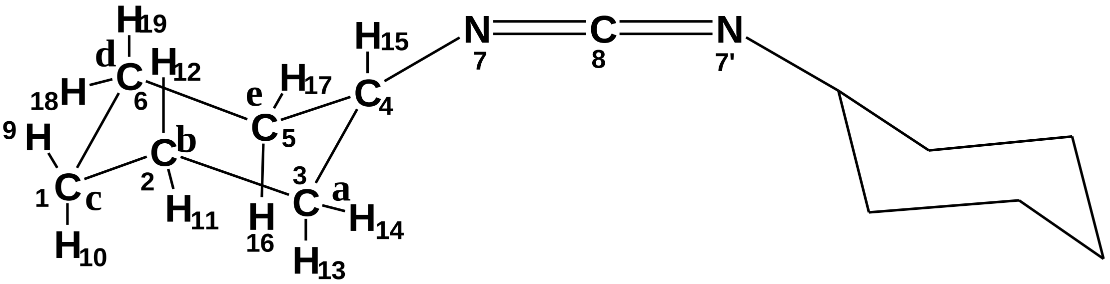

Figure 6.1. Atom numbering scheme for DCC used in the DFT calculations.

6.3.1.1. *Geometry Optimization*

It was found that the equatorial-C_2 structure has significantly lower energy than the axial-C_2 structure and both structures with C_i symmetry. Models with higher symmetry (C_{2v} and C_{2h}) were also considered but these had much higher energies and were not further explored. Calculation of the normal modes for the equatorial-C_i structure revealed two vibrations with imaginary wavenumbers. We did find that optimisation of the C_2 structure with smaller basis sets (e.g. cc-pVDZ) yielded one imaginary normal mode of *b* symmetry, indicating that, in this case, a basis set of at least triple-zeta quality is necessary in order to compute an accurate molecular geometry. The optimized structures are shown in Figure 6.2 with a list of computed bond distances, interbond angles and dihedral angles in Table 6.2.

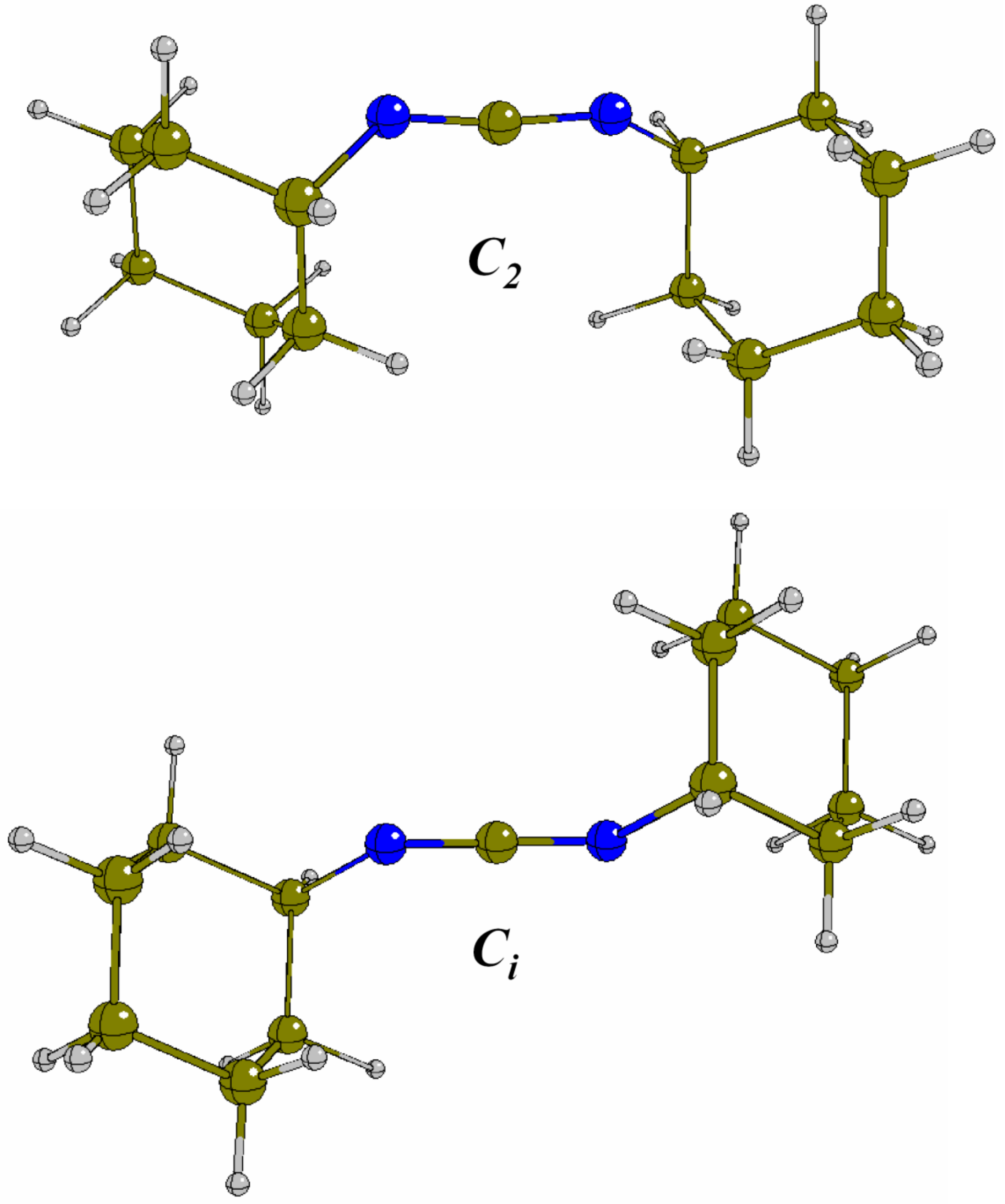

Figure 6.2. Optimised geometry of DCC From B3-LYP/cc-pVTZ calculations of models with C_2 and C_i symmetry.

The calculated structure of the *cis* model displays C_2 symmetry via 180° rotation around its principal axis (through atom C8); the two saturated ring systems (both of which possess a chair conformation) are connected by a non-linear N=C=N moiety, in agreement with the results reported by Jensen[11] for disilylcarbodiimide. On the other hand the calculated structure for the *trans* model has a linear N=C=N group.

Table 6.2. Calculated (B3-LYP/cc-pVTZ) geometric parameters and scaled principal force constants corresponding to the internal coordinates for the C_2 and C_i structures of DCC

	C_2 structure		C_i structure	
	r / Å	f / mdyn Å^{-1}	r / Å	f / mdyn Å^{-1}
r(C1-H10)	1.0949	4.596	1.0950	4.592
r(C1-H9)	1.0921	4.678	1.0922	4.676
r(C1-C6)	1.5313	3.204	1.5315	3.205
r(C2-C1)	1.5311	3.203	1.5330	3.192
r(C3-H13)	1.0938	4.645	1.0940	4.636
r(C3-C4)	1.5314	3.171	1.5310	3.202
r(C3-C2)	1.5314	3.223	1.5305	3.244
r(C4-C5)	1.5329	3.130	1.5359	3.068
r(C5-H16)	1.0938	4.647	1.0939	4.638
r(C5-H17)	1.0916	4.702	1.0919	4.592
r(C5-C6)	1.5320	3.214	1.5317	3.219
r(C6-H18)	1.0919	4.686	1.0920	4.680
r(N7-C4)	1.4660	4.431	1.4465	4.810
r(C8-N7)	1.2174	12.192	1.2096	12.908
r(H11-C2)	1.0919	4.683	1.0919	4.685
r(H12-C2)	1.0953	4.582	1.0953	4.582
r(H14-C3)	1.0918	4.695	1.0913	4.714
r(H15-C4)	1.0967	4.477	1.0975	4.453
r(H19-C6)	1.0952	4.584	1.0951	4.589

	C_2 structure		C_i structure	
	θ / °	f / mdyn Å^{-1}	θ / °	f / mdyn Å^{-1}
θ(H10-C1-H9)	106.5680	0.469	106.5490	0.468
θ(H10-C1-C6)	109.1846	0.560	109.1699	0.555
θ(H10-C1-C2)	109.2267	0.557	109.1953	0.553
θ(H9-C1-C6)	110.2603	0.550	110.2368	0.548
θ(H9-C1-C2)	110.2583	0.550	110.2834	0.547
θ(C6-C1-C2)	111.2206	0.558	111.2799	0.559
θ(C1-C6-C5)	111.6385	0.559	111.6013	0.559
θ(C1-C6-H18)	110.4147	0.548	110.4246	0.546
θ(C1-C6-H19)	109.1986	0.553	109.2373	0.550
θ(C1-C2-C3)	111.6044	0.558	111.6973	0.561
θ(C1-C2-H11)	110.4026	0.547	110.3406	0.548
θ(C1-C2-H12)	109.2057	0.553	109.1717	0.552
θ(H11-C2-H12)	106.3069	0.471	106.3097	0.471
θ(H13-C3-C4)	108.0662	0.574	108.2196	0.574
θ(H13-C3-C2)	110.0602	0.538	110.0420	0.534
θ(H13-C3-H14)	106.6947	0.470	106.7541	0.469
θ(C4-C3-C2)	111.7260	0.552	111.5837	0.558
θ(C3-C4-C5)	110.9291	0.436	110.8240	0.439
θ(C3-C4-N7)	109.3887	0.780	109.7159	0.792
θ(C4-C3-H14)	109.4193	0.570	109.2538	0.568
θ(C3-C4-H15)	108.5943	0.374	108.0216	0.366
θ(C3-C2-H11)	109.7098	0.551	109.8070	0.550
θ(C3-C2-H12)	109.4652	0.560	109.3617	0.558
θ(C2-C3-H14)	110.7121	0.538	110.8345	0.537
θ(C4-C5-H16)	108.2027	0.568	108.1908	0.567
θ(C4-C5-H17)	109.4121	0.567	109.4200	0.564
θ(C4-C5-C6)	111.5278	0.551	111.5181	0.556
θ(C5-C4-N7)	109.7066	0.746	111.6294	0.774
θ(C5-C4-H15)	108.3991	0.366	108.1869	0.366
θ(H16-C5-H17)	106.7703	0.468	106.8819	0.467
θ(H16-C5-C6)	110.1057	0.537	110.0173	0.534
θ(H17-C5-C6)	110.6762	0.540	110.6718	0.540
θ(C5-C6-H18)	109.7135	0.550	109.7445	0.549
θ(C5-C6-H19)	109.3877	0.562	109.3451	0.558
θ(H18-C6-H19)	106.3401	0.471	106.3419	0.471
θ(C4-N7-C8)	127.0484	0.491	138.8471	0.279
θ(N7-C4-H15)	109.8007	0.598	108.3493	0.573
θ(N7-C8-N7')	172.84	0.653	180.00	ip 0.698 op 0.498

	C_2 structure		C_i structure	
	τ / °	f / mdyn $Å^{-1}$	τ / °	f / mdyn $Å^{-1}$
τ(C5-C6-C1-C2)	54.5739	0.195	54.3412	0.193
τ(C6-C1-C2-C3)	-54.3988	0.196	-54.3255	0.193
τ(C1-C6-C5-C4)	-55.1260	0.186	-55.0883	0.186
τ(C1-C2-C3-C4)	54.9196	0.184	55.0872	0.184
τ(C5-C4-C3-C2)	-54.9260	0.198	-55.2156	0.196
τ(C3-C4-C5-C6)	54.9709	0.201	55.2477	0.197
τ(C3-C4-N7-C8)	-130.2839	0.159	-167.3603	0.159
τ(C5-C4-N7-C8)	107.8252	0.154	69.3864	0.159
τ(H15-C4-N7-C8)	-11.2067	0.127	-49.6432	0.184
τ(C4-N7-C8-N7')	-134.1861	0.136	180.00	---
τ(C4-N7-N7'-C4')	95.75	---	180.00	-0.045

6.3.1.2. ***Structure***

To our knowledge, the X-ray crystallographic structure of DCC has not been reported. We calculated the C=N distance to be 1.2174 Å and the NCN angle to be 172.84° for the equatorial-C_2 model, which are in excellent agreement with the values obtained by rotational spectroscopy for the parent molecule HNCNH[8] (1.2242 Å and 170.63°, respectively). The calculated CC bond distances in the cyclohexyl rings are in the range 1.5311-1.5329 Å, which compare favourably with experimental values for cyclohexane (1.5194-1.5275[16], and 1.5296-1.5403 Å[17]) and cylohexylamine hydrochloride (1.4931-1.5222 Å[21]). The computed C-N distance (1.4660 Å) is also comparable with that determined for cylohexylamine hydrochloride (1.4873 Å[18]). The computed bond distances for the equatorial-C_i model are very similar to those for the equatorial-C_2 model, except for the C-N and N=C distances which are somewhat shorter.

6.3.2. Vibrational Spectra and Assignments

DCC contains 37 atoms, thus there are 105 normal modes, which transform under C_2 symmetry as $\Gamma_{3N-6} = 53a + 52b$, and under C_i symmetry as $\Gamma_{3N-6} = 51a_g + 54a_u$. Although all vibrations are, in principle, active in both IR and Raman for the equatorial-C_2 model, we show that the band assignments (*vide infra*) establish that almost all of the

Raman bands could be attributed to vibrations of *a* symmetry and almost all the IR bands to vibrations of *b* symmetry. Normal coordinate analyses for the two models involved the use of a general valence force field (GVFF) defined by the set of 133 internal coordinates listed in Table 6.2. These were reduced to a set of $3N$-6 symmetry-adapted internal coordinates, by construction of local symmetry coordinates where appropriate, i.e. for methylene groups and the ring stretches, in-plane and out-of-plane deformations of the cyclohexyl rings. The GVFF principal force constants are listed in Table 6.1. Definitions of symmetry-adapted coordinates are given in Table 6.3.

Table 6.3. Definitions of symmetry-adapted internal coordinates

(a) carbodiimide group

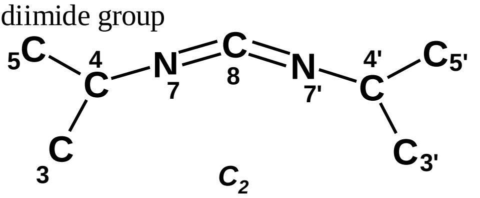

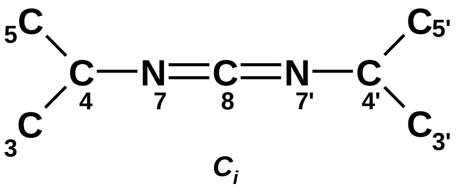

$\nu_s(NC) = {}^1/_{\sqrt{2}}\,[r(C4N7) + r(C4'N7')]$
$\nu_{as}(NC) = {}^1/_{\sqrt{2}}\,[r(C4N7) - r(C4'N7')]$
$\nu_s(NCN) = {}^1/_{\sqrt{2}}\,[r(N7C8) + r(N7'C8)]$
$\nu_{as}(NCN) = {}^1/_{\sqrt{2}}\,[r(N7C8) - r(N7'C8)]$
$\delta(CNC) = {}^1/_{\sqrt{2}}\,[\theta(C4N7C8) \pm \theta(C4'N7'C8)]$
$\tau(NC) = \frac{1}{2}\,[\tau(C8N7C4C5) + \tau(C8N7C4C3) \pm \tau(C8N7'C4'C5') \pm \tau(C8N7'C4'C3')]$
C_2: $\delta(NCN) = \delta(N7C8N7')$
$\tau(C{=}N) = {}^1/_{\sqrt{2}}\,[\tau(C4N7C8N7') \pm \tau(C4'N7'C8N7)]$
C_i: $\delta_{ip}(NCN) = \delta_{ip}(N7C8N7')$
$\delta_{op}(NCN) = \delta_{op}(N7C8N7')$

(b) methylene groups[a]

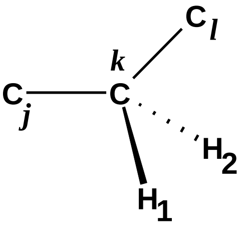

$r_i = r(C_kH_i)$
$\theta = 2(H_1C_kH_2)$
$(_i = 2(C_jC_kH_i)$
$*_i = 2(C_lC_kH_i)$

$\nu_s(CH_2^k) = {}^1/_{\sqrt{2}}\,(r_1 + r_2)$
$\nu_{as}(CH_2^k) = {}^1/_{\sqrt{2}}\,(r_1 - r_2)$
$\delta(CH_2^k) = {}^1/_{2\sqrt{2}}\,(4\alpha - \gamma_1 - \gamma_2 - \delta_1 - \delta_2)$
$\rho(CH_2^k) = \frac{1}{2}\,(\gamma_1 - \gamma_2 + \delta_1 - \delta_2)$
$\omega(CH_2^k) = \frac{1}{2}\,(\gamma_1 + \gamma_2 - \delta_1 - \delta_2)$
$\tau(CH_2^k) = \frac{1}{2}\,(\gamma_1 - \gamma_2 - \delta_1 + \delta_2)$

(c) methine groups[a]

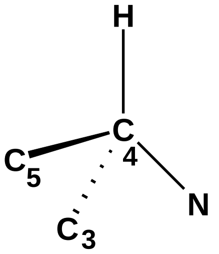

$\delta(CH) = {}^1/_{\sqrt{3}}\,[2\theta(HC4N) - \theta(HC4C5) - \theta(HC4C3)]$
$\delta'(CH) = {}^1/_{\sqrt{2}}\,[\theta(HC4C_5) - \theta(HC4C3)]$
$\delta(NC4C5) = \theta(NC4C5)$
$\delta(NC4C3) = \theta(NC4C3)$

(d) cyclohexyl rings[a]

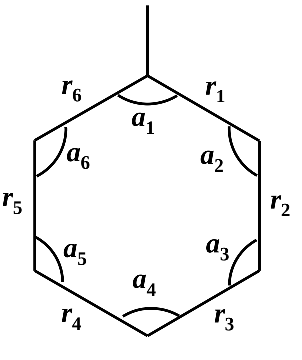

$\nu(\text{ring-1}) = {}^1/_{\sqrt{6}}\,(r_1 + r_2 + r_3 + r_4 + r_5 + r_6)$
$\nu(\text{ring-2}) = {}^1/_{\sqrt{12}}\,(-r_1 + 2r_2 - r_3 - r_4 + 2r_5 - r_6)$
$\nu(\text{ring-3}) = \frac{1}{2}\,(r_1 - r_3 + r_4 - r_6)$
$\nu(\text{ring-4}) = {}^1/_{\sqrt{6}}\,(-r_1 + r_2 - r_3 + r_4 - r_5 + r_6)$
$\nu(\text{ring-5}) = \frac{1}{2}\,(-r_1 + r_3 + r_4 - r_6)$
$\nu(\text{ring-6}) = {}^1/_{\sqrt{12}}\,(r_1 + 2r_2 + r_3 - r_4 - 2r_5 - r_6)$
$\delta(\text{ring-1}) = {}^1/_{\sqrt{12}}\,(-2\alpha_1 + \alpha_2 + \alpha_3 - 2\alpha_4 + \alpha_5 + \alpha_6)$
$\delta(\text{ring-2}) = \frac{1}{2}\,(\alpha_2 - \alpha_3 + \alpha_5 - \alpha_6)$
$\delta(\text{ring-3}) = {}^1/_{\sqrt{6}}\,(-\alpha_1 + \alpha_2 - \alpha_3 + \alpha_4 - \alpha_5 + \alpha_6)$
$\tau(\text{ring-1}) = {}^1/_{\sqrt{6}}\,(\tau_1 - \tau_2 + \tau_3 - \tau_4 + \tau_5 - \tau_6)$
$\tau(\text{ring-2}) = {}^1/_{\sqrt{12}}\,(-\tau_1 + 2\tau_2 - \tau_3 - \tau_4 + 2\tau_5 - \tau_6)$
$\tau(\text{ring-3}) = \frac{1}{2}\,(\tau_1 - \tau_3 + \tau_4 - \tau_6)$

τ_i is the torsion about the *i*th bond

a. In each case symmetric (a or ag) and antisymmetric (b or au) combinations were constructed for the equivalent coordinates on either side of the molecule to conform to overall C_2 or C_i symmetry.

Table 6.4. Comparison of experimental IR and Raman spectra of DCC with calculated spectra for the equatorial-C_2 model.

***a* symmetry group**

Experimental (solid)		Calculated(B3-LYP/cc-pVTZ)	
IR $\tilde{\nu}$ / cm^{-1}	Raman $\tilde{\nu}$ / cm^{-1}	$\tilde{\nu}$ / cm^{-1}	Potential energy distributions (%)
	2940vs	2933	$\nu_{as}(CH_2^a)$ (28), $\nu_{as}(CH_2^b)$ (55)
2930s	2922sh	2928	$\nu_{as}(CH_2^a)$ (56), $\nu_{as}(CH_2^e)$ (33)
		2924	$\nu_{as}(CH_2^b)$ (22), $\nu_{as}(CH_2^d)$ (42)
		2920	$\nu_s(CH_2^a)$ (12), $\nu_{as}(CH_2^c)$ (57), $\nu_s(CH_2^d)$ (10), $\nu_{as}(CH_2^d)$ (11)
		2920	$\nu_s(CH_2^b)$ (16), $\nu_{as}(CH_2^b)$ (42), $\nu_{as}(CH_2^c)$ (13), $\nu_{as}(CH_2^d)$ (17)
2903sh	2896w	2892	$\nu_s(CH_2^a)$ (36), $\nu_s(CH_2^e)$ (52)
		2888	$\nu_s(CH_2^a)$ (52), $\nu_s(CH_2^e)$ (35)
		2880	$\nu_s(CH_2^b)$ (16), $\nu_s(CH_2^c)$ (59), $\nu_s(CH_2^d)$ (19)
2853m	2854vs	2872	$\nu_s(CH_2^b)$ (31), $\nu_s(CH_2^d)$ (42), $\nu_{as}(CH_2^d)$ (13)
		2870	$\nu_s(CH_2^b)$ (27), $\nu_{as}(CH_2^b)$ (13), $\nu_s(CH_2^c)$ (23), $\nu_{as}(CH_2^c)$ (15), $\nu_s(CH_2^d)$ (13)
		2848	ν(CH) (96)
2066sh			combination
1463sh	1464sh	1458	$\delta(CH_2^a)$ (26), $\delta(CH_2^b)$ (15), $\delta(CH_2^c)$ (21), $\delta(CH_2^d)$ (14), $\delta(CH_2^e)$ (23)
1449m	1446m	1446	$\delta(CH_2^a)$ (22), $\delta(CH_2^b)$ (25), $\delta(CH_2^d)$ (37), $\delta(CH_2^e)$ (14)
		1441	$\delta(CH_2^b)$ (13), $\delta(CH_2^c)$ (34), $\delta(CH_2^d)$ (20), $\delta(CH_2^e)$ (29)
		1441	$\delta(CH_2^a)$ (13), $\delta(CH_2^b)$ (13), $\delta(CH_2^c)$ (71)
		1437	$\delta(CH_2^a)$ (29), $\delta(CH_2^b)$ (19), $\delta(CH_2^d)$ (18), $\delta(CH_2^e)$ (31)
	1406w	1404	ν_s(N=C=N) (61), ν_s(NC) (25)
1360m	1362sh	1352	δ(CH) (18), $\omega(CH_2^a)$ (27), $\omega(CH_2^e)$ (19)
1346m	1346w	1339	δ'(CH) (26), $\omega(CH_2^d)$ (31), $\tau(CH_2^d)$ (10)
		1336	δ'(CH) (19), $\omega(CH_2^b)$ (27)
		1334	$\omega(CH_2^c)$ (53)
1314sh		1324	$\omega(CH_2^b)$ (25), $\omega(CH_2^d)$ (27), $\tau(CH_2^c)$ (17)
	1305w	1298	$\omega(CH_2^a)$ (34), $\omega(CH_2^e)$ (15), $\tau(CH_2^b)$ (16)
1299m		1294	δ(CH) (41), $\omega(CH_2^e)$ (18), $\tau(CH_2^d)$ (20)
1268w	1268sh	1247	$\tau(CH_2^a)$ (37), $\tau(CH_2^e)$ (24)
1259w	1261m	1245	$\tau(CH_2^c)$ (42), $\tau(CH_2^e)$ (18)
1240w	1242w	1229	δ(CH) (11), $\tau(CH_2^b)$ (20), $\tau(CH_2^d)$ (18)
1189w	1189w	1173	ν(ring-3) (18), $\omega(CH_2^a)$ (11), $\omega(CH_2^e)$ (11), $\tau(CH_2^b)$ (13), $\tau(CH_2^d)$ (13)
1148w	1145m	1135	τ(ring-1) (13), $\rho(CH_2^a)$ (16), $\rho(CH_2^b)$ (11), $\rho(CH_2^c)$ (16), $\rho(CH_2^d)$ (10), $\rho(CH_2^e)$ (15)
1124w	1125vw		
1091vw		1081	ν(ring-4) (89)
1074vw	1075w	1058	ν(ring-3) (14), $\omega(CH_2^b)$ (11), $\omega(CH_2^d)$ (12), $\tau(CH_2^a)$ (16), $\tau(CH_2^c)$ (18), $\tau(CH_2^e)$ (17)
1047m	1053w	1035	ν(ring-3) (27), δ'(CH) (11), $\omega(CH_2^c)$ (12), $\tau(CH_2^b)$ (13), $\tau(CH_2^d)$ (14)
1023w	1027m	1021	ν(ring-2) (40), δ(ring-3) (18)
	1008w	1010	ν(ring-2) (25), δ(ring-3) (27)
952w	952vw	912	ν(ring-6) (36), $\rho(CH_2^a)$ (16), $\rho(CH_2^b)$ (16), $\rho(CH_2^d)$ (20), $\rho(CH_2^e)$ (16)
891m	892w	888	ν_s(N=C=N) (12), ν_s(NC) (22), ν(ring-5) (44)
	882w 878w	878	ν(ring-6) (34), $\rho(CH_2^a)$ (11), $\rho(CH_2^b)$ (12), $\rho(CH_2^d)$ (10), $\rho(CH_2^e)$ (15)
864vw	868sh	873	ν(ring-5) (12), $\rho(CH_2^a)$ (10), $\rho(CH_2^c)$ (24)
842w 836w	842sh 836m		
819w	818m	827	ν(ring-1) (39), ν(ring-5) (25), $\rho(CH_2^c)$ (19)
780sh	780s	778	ν(ring-1) (32), $\rho(CH_2^c)$ (10)
		773	ν(ring-3) (12), $\rho(CH_2^a)$ (19), $\rho(CH_2^b)$ (22), $\rho(CH_2^d)$ (24), $\rho(CH_2^e)$ (18)
670sh	668w	640	δ(CNC) (16), δ(NCN) (57)

***a* symmetry group**

Experimental (solid)		Calculated(B3-LYP/cc-pVTZ)	
IR $\tilde{\nu}$ / $\mathrm{cm^{-1}}$	Raman $\tilde{\nu}$ / $\mathrm{cm^{-1}}$	$\tilde{\nu}$ / $\mathrm{cm^{-1}}$	Potential energy distributions (%)
600w,br	600w		
	567vw		
540w	540sh		
526vw	521w		
518vw		503	δ(ring-3) (37), ρ($\mathrm{CH_2^c}$) (12)
475vw			
457vw	456w	456	δ(ring-2) (38), δ($\mathrm{NCC^e}$) (17)
	447sh	437	δ(ring-1) (40), τ(ring-1) (20)
		406	δ(ring-2) (43), τ(C=N) (16), δ($\mathrm{NCC^e}$) (16)
	354vw		
	335vw	329	τ(ring-2) (54), τ(ring-3) (13)
	306vw	285	δ(ring-2) (14), τ(ring-3) (21), ν_s(NC) (18), δ($\mathrm{NCC^a}$) (26)
	196vw	226	τ(ring-2) (99)
	179vw		
	168vw	145	τ(ring-3) (48), δ(CNC) (17), δ($\mathrm{NCC^e}$) (16)
		93	δ(CNC) (33), δ($\mathrm{NCC^a}$) (19), τ(C=N) (30)
		40	δ(CNC) (19), δ($\mathrm{NCC^e}$) (12), τ(C=N) (47), τ(NC) (12)
		26	τ(NC) (94)

***b* symmetry group**

Experimental (solid)		Calculated (B3-LYP/cc-pVTZ)	
IR $\tilde{\nu}$ / $\mathrm{cm^{-1}}$	Raman $\tilde{\nu}$ / $\mathrm{cm^{-1}}$	$\tilde{\nu}$ / $\mathrm{cm^{-1}}$	Potential energy distributions (%)
	2940vs	2933	ν_{as}($\mathrm{CH_2^a}$) (24), ν_{as}($\mathrm{CH_2^e}$) (59)
2930s	2922sh	2928	ν_{as}($\mathrm{CH_2^a}$) (61), ν_{as}($\mathrm{CH_2^e}$) (28)
		2923	ν_{as}($\mathrm{CH_2^b}$) (22), ν_{as}($\mathrm{CH_2^d}$) (41)
		2920	ν_{as}($\mathrm{CH_2^b}$) (14), ν_{as}($\mathrm{CH_2^c}$) (37), ν_s($\mathrm{CH_2^d}$) (13), ν_{as}($\mathrm{CH_2^d}$) (22)
		2920	ν_s($\mathrm{CH_2^b}$) (16), ν_{as}($\mathrm{CH_2^b}$) (32), ν_{as}($\mathrm{CH_2^c}$) (31)
2903sh	2896w	2892	ν_s($\mathrm{CH_2^a}$) (38), ν_s($\mathrm{CH_2^e}$) (50)
		2888	ν_s($\mathrm{CH_2^a}$) (49), ν_s($\mathrm{CH_2^e}$) (38)
		2880	ν_s($\mathrm{CH_2^b}$) (16), ν_s($\mathrm{CH_2^c}$) (59), ν_s($\mathrm{CH_2^d}$) (19)
2853m	2854vs	2872	ν_s($\mathrm{CH_2^b}$) (29), ν_s($\mathrm{CH_2^d}$) (43), ν_{as}($\mathrm{CH_2^d}$) (14)
		2870	ν_s($\mathrm{CH_2^b}$) (29), ν_{as}($\mathrm{CH_2^b}$) (14), ν_s($\mathrm{CH_2^c}$) (22), ν_{as}($\mathrm{CH_2^c}$) (15), ν_s($\mathrm{CH_2^d}$) (12)
		2846	ν(CH) (96)
2118vs		2120	ν_{as}(N=C=N) (98)
1463sh	1464sh	1458	δ($\mathrm{CH_2^a}$) (25), δ($\mathrm{CH_2^b}$) (15), δ($\mathrm{CH_2^c}$) (22), δ($\mathrm{CH_2^d}$) (15), δ($\mathrm{CH_2^e}$) (22)
1449m	1446m	1445	δ($\mathrm{CH_2^a}$) (23), δ($\mathrm{CH_2^b}$) (26), δ($\mathrm{CH_2^d}$) (36), δ($\mathrm{CH_2^e}$) (14)
		1441	δ($\mathrm{CH_2^a}$) (17), δ($\mathrm{CH_2^b}$) (40), δ($\mathrm{CH_2^d}$) (23), δ($\mathrm{CH_2^e}$) (17)
		1440	δ($\mathrm{CH_2^c}$) (73), δ($\mathrm{CH_2^e}$) (11)
1419vw		1437	δ($\mathrm{CH_2^a}$) (29), δ($\mathrm{CH_2^b}$) (17), δ($\mathrm{CH_2^d}$) (17), δ($\mathrm{CH_2^e}$) (34)
1360m	1362sh	1352	δ(CH) (18), ω($\mathrm{CH_2^a}$) (25), ω($\mathrm{CH_2^b}$) (11), ω($\mathrm{CH_2^e}$) (17)
1346m	1346w	1337	δ'(CH) (30), ω($\mathrm{CH_2^d}$) (27)
		1334	ω($\mathrm{CH_2^c}$) (53)
		1332	δ'(CH) (23), ω($\mathrm{CH_2^b}$) (20)
1314sh		1324	ω($\mathrm{CH_2^b}$) (24), ω($\mathrm{CH_2^d}$) (28), τ($\mathrm{CH_2^c}$) (17)
	1305w	1298	δ(CH) (11), ω($\mathrm{CH_2^a}$) (33), ω($\mathrm{CH_2^b}$) (16), ω($\mathrm{CH_2^e}$) (15)
		1293	δ(CH) (47), ω($\mathrm{CH_2^e}$) (16), τ($\mathrm{CH_2^d}$) (19)
1268w	1268sh	1247	τ($\mathrm{CH_2^a}$) (35), τ($\mathrm{CH_2^e}$) (26)
1259w	1261m	1245	τ($\mathrm{CH_2^c}$) (42), τ($\mathrm{CH_2^e}$) (16)
1240w	1242w	1230	δ(CH) (11), τ($\mathrm{CH_2^b}$) (21), τ($\mathrm{CH_2^d}$) (18)

***b* symmetry group**

Experimental (solid)		Calculated (B3-LYP/cc-pVTZ)	
IR $\tilde{\nu}$ / cm^{-1}	Raman $\tilde{\nu}$ / cm^{-1}	$\tilde{\nu}$ / cm^{-1}	Potential energy distributions (%)
1189w	1189w	1169	ν(ring-3) (18), ω(CH$_2^a$) (11), ω(CH$_2^e$) (11), τ(CH$_2^b$) (14), τ(CH$_2^d$) (14)
1148w	1145m	1137	τ(ring-1) (13), ρ(CH$_2^a$) (16), ρ(CH$_2^b$) (10), ρ(CH$_2^d$) (11), ρ(CH$_2^e$) (15)
1124w	1125vw		
1091vw			
1074vw	1075w	1080	ν(ring-4) (89)
1047m	1053w	1057	ν(ring-3) (12), ω(CH$_2^b$) (10), ω(CH$_2^d$) (11), τ(CH$_2^a$) (17), τ(CH$_2^c$) (18), τ(CH$_2^e$) (19)
1023w	1027m	1038	ν_{as}(NC) (37), δ(ring-3) (31)
		1034	ν(ring-3) (30), δ'(CH) (10), ω(CH$_2^c$) (13), ρ(CH$_2^b$) (12), ρ(CH$_2^d$) (14)
	1008w	1017	δ(ring-2) (61)
952w	952vw	946	ν_{as}(NC) (35), ν(ring-5) (11), δ(ring-3) (13)
925vw	925vw	911	ν(ring-6) (35), ρ(CH$_2^a$) (11), ρ(CH$_2^e$) (10), τ(CH$_2^c$) (10)
891m	892w	876	ν(ring-5) (11), ν(ring-6) (24), ρ(CH$_2^b$) (12), ρ(CH$_2^e$) (17)
864vw	868sh	876	ν(ring-5) (19), ν(ring-6) (14), ρ(CH$_2^a$) (16), ρ(CH$_2^c$) (13), ρ(CH$_2^d$) (10)
842w 836w	842sh 836m	834	ν(ring-1) (21), ν(ring-5) (39), ρ(CH$_2^c$) (24)
819 w	818m		
787 w		781	ν(ring-1) (44)
780sh	780s	772	ν(ring-3) (12), ρ(CH$_2^a$) (19), ρ(CH$_2^b$) (22), ρ(CH$_2^d$) (24), ρ(CH$_2^e$) (18)
643m,br			
629m,br	629vw	624	δ(CNC) (23), τ(C=N) (67)
600w,br	600w		
540w	540sh	533	δ(ring-3) (27), ρ(CH$_2^c$) (11)
525vw	521w		
518vw			
	484vw		
475vw		460	δ(ring-3) (17), τ(ring-1) (18), δ(NCC^e) (16), ρ(CH$_2^a$) (10)
	447sh	446	δ(ring-2) (66)
	395vw	392	δ(ring-1) (71)
	335vw	337	δ(ring-2) (11), τ(ring-1) (29), δ(NCC^e) (36)
	306vw	326	τ(ring-1) (32), τ(ring-3) (10), δ(NCC^a) (30)
	281vw		
	214vw	226	τ(ring-2) (99)
	208vw		
	196vw	196	τ(ring-3) (54), δ(CNC) (28), τ(C=N) (12)
	168vw		
		83	τ(ring-3) (22), δ(NCC^a) (10), δ(NCC^e) (10), δ(CNC) (39), τ(C=N) (10)
		13	τ(NC) (100)

The IR spectra of DCC in the solid state (as a KBr disc and from an ATR measurement of the pure solid) and in CDCl$_3$ solution, with solvent subtracted, are shown in Figure 6.3 together with the calculated IR spectra for both models.

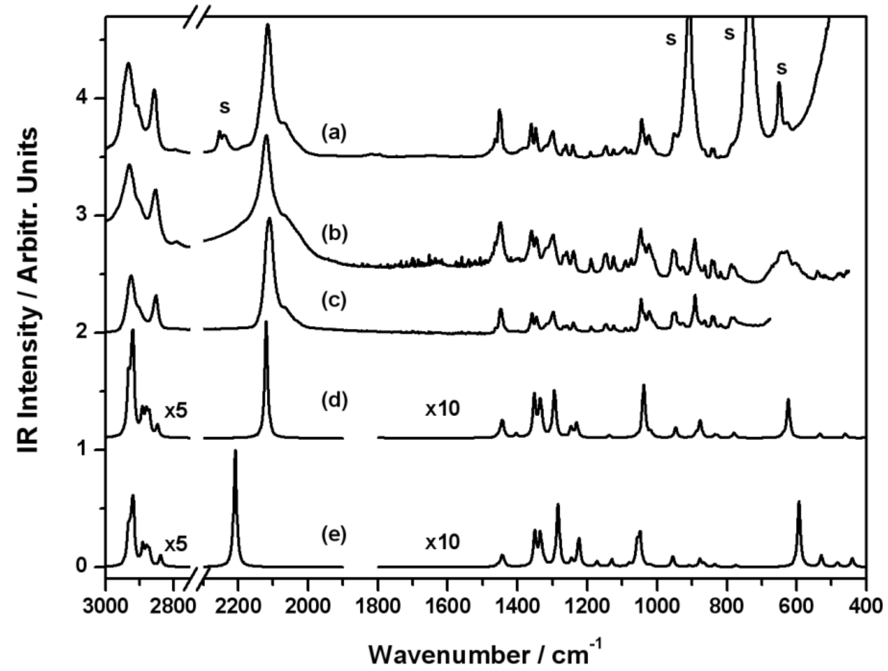

Figure 6.3. Experimental and calculated IR spectra of DCC. (a) IR spectrum of DCC in $CDCl_3$ solution, (b) IR spectrum of solid DCC in a KBr disc, (c) ATR-IR spectrum of solid DCC, (d) computed IR spectrum for the *cis* (C_2) model, and (e) computed IR spectrum for the *trans* (C_i) model.

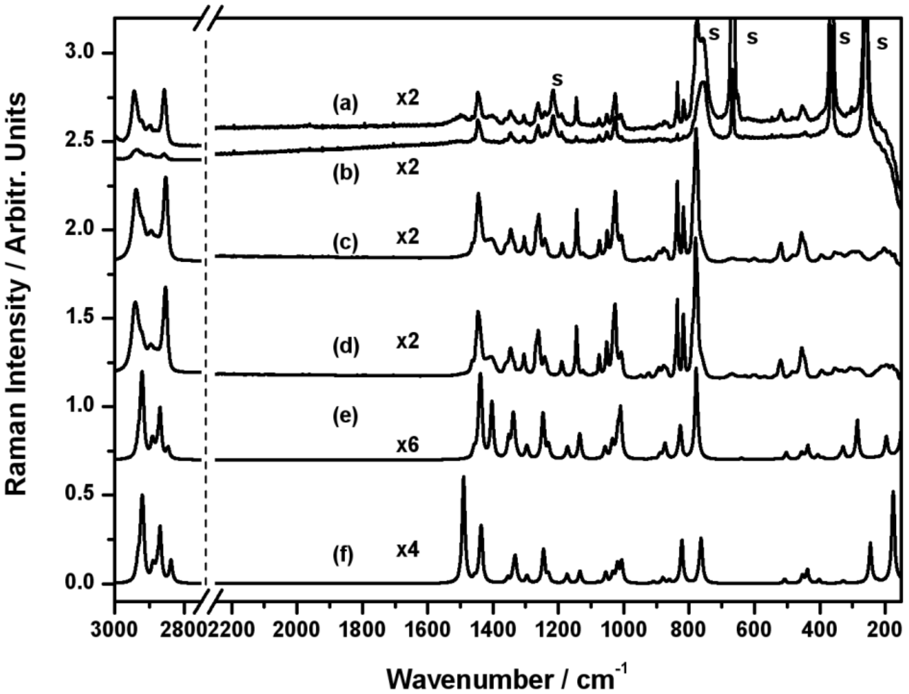

Figure 6.4. Experimental and calculated Raman spectra of DCC. (a) Polarised and (b) depolarised $CHCl_3$ solution spectra, (c), liquid state spectrum at 60 °C, (d) solid-state spectrum, (e) computed Raman spectrum for the *cis* (C_2) model, and (f) computed Raman spectrum for the *trans* (C_i) model.

The Raman spectra of DCC in $CHCl_3$ solution (polarized and depolarized) and in the liquid and solid states are shown in Figure 6.4 together with the calculated Raman spectra for both models. Experimental IR and Raman band positions are compared with the scaled computed values for the equatorial-C_2 model in Table 6.4. Where we have listed both IR and Raman band positions in both the *a* and *b* symmetry sections of the table to facilitate comparison. The listed experimental band positions are those obtained from the solid-state IR and Raman spectra because these are free of solvent interference. However, the solution phase band positions are mostly within 2 cm^{-1} of the solid state values and none deviate more than 4 cm^{-1}.

In order to support the assertion that the spectra are best interpreted in terms of the equatorial-C_2 model, spectroscopic data for the equatorial-C_i model was computed and compared with the experimental data in Table 6.5. Careful comparison of the experimental spectra with the calculated spectra of both models is required in order to be confident of structure prediction. In general, it appears that throughout most of the spectrum the rule of mutual exclusion is not obeyed, militating against the centrosymmetric equatorial-C_i structure. On the other hand, there is apparent mutual exclusion of the N=C=N stretching modes, since the antisymmetric stretch is seen in the IR spectrum but absent from the Raman spectrum, and vice versa for the symmetric stretch. Nevertheless, this is not inconsistent with IR and Raman spectra calculated for the equatorial-C_2 structure, which indicate very low Raman intensity for ν_{as}(N=C=N) and very low IR intensity for ν_s(N=C=N). It follows therefore that although the overall IR and Raman spectra clearly establish the equatorial-C_2 structure the apparent mutual exclusion of the N=C=N stretching modes is a consequence of very weak, and therefore undetectable, intensities for ν_{as}(N=C=N) in the Raman spectrum and ν_s(N=C=N) in the IR spectrum. Furthermore, for the equatorial-C_i model the predicted positions of both these bands are *ca.* 100 cm^{-1} higher than their experimental value.

Table 6.5. Comparison of experimental IR and Raman spectra of DCC with calculated spectra for the model with C_i symmetry.

a_g symmetry group

Raman	Calculated(B3-LYP/cc-pVTZ)	
$\tilde{\nu}$ / cm^{-1}	$\tilde{\nu}$ / cm^{-1}	Potential energy distributions (%)
2940vs	2934	$\nu_{as}(CH_2^a)$ (72), $\nu_{as}(CH_2^e)$ (12)
2922sh	2928	$\nu_{as}(CH_2^a)$ (14), $\nu_{as}(CH_2^e)$ (68)
	2923	$\nu_{as}(CH_2^b)$ (46), $\nu_{as}(CH_2^d)$ (19)
	2919	$\nu_s(CH_2^b)$ (12), $\nu_{as}(CH_2^b)$ (20), $\nu_{as}(CH_2^c)$ (36), $\nu_{as}(CH_2^d)$ (18)
	2919	$\nu_s(CH_2^c)$ (10), $\nu_s(CH_2^d)$ (15), $\nu_{as}(CH_2^c)$ (33), $\nu_{as}(CH_2^d)$ (31)
2896w	2891	$\nu_s(CH_2^a)$ (54), $\nu_s(CH_2^e)$ (31)
	2886	$\nu_s(CH_2^a)$ (28), $\nu_s(CH_2^e)$ (56)
	2879	$\nu_s(CH_2^b)$ (16), $\nu_s(CH_2^c)$ (52), $\nu_s(CH_2^d)$ (25)
	2873	$\nu_s(CH_2^b)$ (25), $\nu_s(CH_2^d)$ (43), $\nu_{as}(CH_2^d)$ (15)
2854vs	2870	$\nu_s(CH_2^b)$ (31), $\nu_s(CH_2^c)$ (26), $\nu_{as}(CH_2^b)$ (16), $\nu_{as}(CH_2^c)$ (15)
	2838	$\nu(CH)$ (97)
1464sh	1490	$\nu_s(N{=}C{=}N)$ (64), $\nu_s(NC)$ (32)
1446m	1456	$\delta(CH_2^a)$ (26), $\delta(CH_2^b)$ (15), $\delta(CH_2^c)$ (22), $\delta(CH_2^d)$ (16), $\delta(CH_2^e)$ (18)
	1445	$\delta(CH_2^a)$ (25), $\delta(CH_2^b)$ (25), $\delta(CH_2^d)$ (38)
	1440	$\delta(CH_2^a)$ (12), $\delta(CH_2^b)$ (38), $\delta(CH_2^d)$ (22), $\delta(CH_2^e)$ (26)
	1438	$\delta(CH_2^a)$ (11), $\delta(CH_2^c)$ (75)
1406w	1435	$\delta(CH_2^a)$ (23), $\delta(CH_2^b)$ (18), $\delta(CH_2^d)$ (19), $\delta(CH_2^e)$ (36)
1362sh	1355	$\delta(CH)$ (25), $\omega(CH_2^a)$ (27), $\omega(CH_2^e)$ (19)
1346w	1338	$\omega(CH_2^b)$ (28), $\omega(CH_2^d)$ (34)
	1333	$\delta'(CH)$ (14), $\omega(CH_2^b)$ (11), $\omega(CH_2^c)$ (31)
	1331	$\delta'(CH)$ (28), $\omega(CH_2^c)$ (33)
1305w	1323	$\omega(CH_2^b)$ (16), $\omega(CH_2^d)$ (26), $\tau(CH_2^c)$ (14)
	1297	$\delta(CH)$ (41), $\omega(CH_2^a)$ (22) , $\tau(CH_2^b)$ (21)
1268sh	1296	$\delta(CH)$ (11), $\omega(CH_2^a)$ (11), $\omega(CH_2^e)$ (34), $\tau(CH_2^d)$ (19)
1261m	1246	$\tau(CH_2^a)$ (38), $\tau(CH_2^e)$ (25)
1242w	1244	$\tau(CH_2^c)$ (42), $\tau(CH_2^e)$ (18)
1189w	1230	$\delta(CH)$ (10), $\tau(CH_2^b)$ (21), $\tau(CH_2^d)$ (19)
1145m	1174	ν(ring-3) (18), $\omega(CH_2^a)$ (11), $\omega(CH_2^e)$ (11), $\tau(CH_2^b)$ (12), $\tau(CH_2^d)$ (13)
1125vw	1135	$\rho(CH_2^a)$ (16), $\rho(CH_2^b)$ (10), $\rho(CH_2^c)$ (16), $\rho(CH_2^d)$ (11), $\rho(CH_2^e)$ (16), τ(ring-1) (13)
1075w	1080	ν(ring-4) (88)
1053w	1056	ν(ring-3) (15), $\omega(CH_2^b)$ (11), $\omega(CH_2^d)$ (13), $\tau(CH_2^a)$ (14), $\tau(CH_2^c)$ (17), $\tau(CH_2^e)$ (17)
1027m	1034	ν(ring-3) (24), $\delta'(CH)$ (12), $\omega(CH_2^c)$ (12), $\tau(CH_2^b)$ (13), $\tau(CH_2^d)$ (15)
	1019	ν(ring-2) (44), δ(ring-3) (14)
1008w	1006	ν(ring-2) (20), δ(ring-3) (31)
952vw		
892w	909	ν(ring-6) (40)
878w	880	ν(ring-5) (60)
868sh	878	ν(ring-6) (28), $\rho(CH_2^a)$ (12), $\rho(CH_2^b)$ (14), $\rho(CH_2^d)$ (10), $\rho(CH_2^e)$ (18)
842sh 836m	861	$\nu(NC)$ (10), $\rho(CH_2^a)$ (13), $\rho(CH_2^c)$ (28)
818m	822	ν(ring-1) (52), ν(ring-5) (21), $\rho(CH_2^c)$ (11)
780s	770	ν(ring-3) (12), $\rho(CH_2^a)$ (16), $\rho(CH_2^b)$ (26), $\rho(CH_2^d)$ (19), $\rho(CH_2^e)$ (20)
	763	ν(ring-1) (20), $\rho(CH_2^c)$ (12), $\rho(CH_2^d)$ (14)
668w		
600vw		
567vw		
540sh		
521w	508	δ(ring-3) (37), $\rho(CH_2^c)$ (12)

a_g symmetry group

Raman $\tilde{\nu}$ / cm^{-1}	Calculated(B3-LYP/cc-pVTZ)	
	$\tilde{\nu}$ / cm^{-1}	Potential energy distributions (%)
456w	454	δ(ring-2) (44), δ(NCC^e) (21)
447sh	438	δ(ring-1) (47), τ(ring-1) (13)
354vw	403	δ(ring-1) (11), δ(ring-2) (32), δ(NCC^e) (20), δ(CNC) (14)
335vw	329	τ(ring-1) (56), τ(ring-3) (16), δ(NCC^e) (15)
306vw	245	δ(ring-1) (11), τ(ring-3) (12), ν(NC) (16), δ(NCC^a) (36)
196vw	223	τ(ring-2) (96)
179vw	175	τ(ring-3) (39), δ(CNC) (31), δ(NCC^e) (14)
168vw		
	96	τ(ring-3) (23), δ(CNC) (49), δ(NCC^a) (18)
	34	τ(NC) (100)

a_u symmetry group

IR $\tilde{\nu}$ / cm^{-1}	Calculated(B3-LYP/cc-pVTZ)	
	$\tilde{\nu}$ / cm^{-1}	Potential energy distributions (%)
	2934	ν_{as}(CH$_2^a$) (72), ν_{as}(CH$_2^e$) (12)
2930s	2928	ν_{as}(CH$_2^a$) (15), ν_{as}(CH$_2^e$) (68)
	2923	ν_{as}(CH$_2^b$) (46), ν_{as}(CH$_2^d$) (18)
	2919	ν_s(CH$_2^b$) (12), ν_{as}(CH$_2^b$) (25), ν_{as}(CH$_2^c$) (21), ν_{as}(CH$_2^d$) (29)
	2919	ν_s(CH$_2^c$) (13), ν_{as}(CH$_2^d$) (13), ν_{as}(CH$_2^c$) (48), ν_{as}(CH$_2^d$) (21)
2903sh	2891	ν_s(CH$_2^a$) (53), ν_s(CH$_2^e$) (31)
	2886	ν_s(CH$_2^a$) (28), ν_s(CH$_2^e$) (56)
	2879	ν_s(CH$_2^b$) (16), ν_s(CH$_2^c$) (52), ν_s(CH$_2^d$) (25)
	2873	ν_s(CH$_2^b$) (26), ν_s(CH$_2^c$) (43), ν_{as}(CH$_2^d$) (14)
2853m	2870	ν_s(CH$_2^b$) (30), ν_s(CH$_2^c$) (27), ν_{as}(CH$_2^b$) (15), ν_{as}(CH$_2^c$) (15)
	2838	ν(CH) (96)
2118vs	2209	ν_{as}(N=C=N) (96)
2066sh		combination
1463sh	1457	δ(CH$_2^a$) (30), δ(CH$_2^b$) (14), δ(CH$_2^c$) (21), δ(CH$_2^d$) (14), δ(CH$_2^e$) (21)
1449m	1445	δ(CH$_2^a$) (23), δ(CH$_2^b$) (27), δ(CH$_2^d$) (40)
	1439	δ(CH$_2^a$) (12), δ(CH$_2^b$) (38), δ(CH$_2^d$) (24), δ(CH$_2^e$) (25)
	1438	δ(CH$_2^c$) (77)
1419vw	1435	δ(CH$_2^a$) (25), δ(CH$_2^b$) (17), δ(CH$_2^d$) (18), δ(CH$_2^e$) (37)
1360w	1350	δ(CH) (10), ω(CH$_2^a$) (25), ω(CH$_2^b$) (14), ω(CH$_2^d$) (11), δ(CH$_2^e$) (18)
1346m	1335	ω(CH$_2^a$) (11), ω(CH$_2^b$) (15), ω(CH$_2^d$) (26)
	1332	ω(CH$_2^b$) (12), ω(CH$_2^c$) (43)
	1329	δ'(CH) (33), ω(CH$_2^b$) (14), ω(CH$_2^c$) (16)
1314sh	1323	δ'(CH) (10), ω(CH$_2^b$) (13), ω(CH$_2^d$) (26), τ(CH$_2^c$) (13)
1299m	1296	δ'(CH) (12), ω(CH$_2^a$) (26), ω(CH$_2^e$) (27)
1268w	1284	δ(CH) (58), τ(CH$_2^b$) (14), τ(CH$_2^d$) (15)
1259w	1245	τ(CH$_2^a$) (38), τ(CH$_2^e$) (21)
1240w	1244	τ(CH$_2^c$) (41), τ(CH$_2^e$) (20)
1189w	1224	δ(CH) (19), τ(CH$_2^b$) (16), τ(CH$_2^d$) (14)
1148w	1172	ν(ring-3) (18), ω(CH$_2^a$) (12), ω(CH$_2^e$) (10), τ(CH$_2^b$) (13), τ(CH$_2^d$) (13)
1124w	1130	τ(ring-1) (12), ρ(CH$_2^a$) (17), ρ(CH$_2^c$) (16), ρ(CH$_2^e$) (16)
1091vw	1080	ν(ring-4) (87)
1074vw	1057	ν_{as}(NC) (13), ν(ring-3) (13), ω(CH$_2^d$) (10), τ(CH$_2^c$) (12), τ(CH$_2^e$) (14)
1047m	1048	ν_{as}(NC) (34), δ(ring-3) (19)
	1033	ν(ring-3) (26). δ'(CH) (11), ω(CH$_2^c$) (12), τ(CH$_2^b$) (12), τ(CH$_2^d$) (15)
1023w	1017	ν(ring-2) (59)

***a_u* symmetry group**

IR	Calculated(B3-LYP/cc-pVTZ)	
$\tilde{\nu}$ / cm^{-1}	$\tilde{\nu}$ / cm^{-1}	Potential energy distributions (%)
952w	955	ν_{as}(NC) (25), δ(ring-3) (18)
925vw	908	ν(ring-6) (39), ρ(CH_2^a) (10), ρ(CH_2^c) (10)
891 m	877	ν(ring-6) (32), ρ(CH_2^a) (12), ρ(CH_2^b) (12), ρ(CH_2^d) (10), ρ(CH_2^e) (16)
864vw	865	ν(ring-5) (31), ρ(CH_2^c) (22)
842w		
836w	834	ν(ring-1) (22), ν(ring-5) (39), ρ(CH_2^e) (23)
819 w		
787 w	773	ν(ring-1) (42), ρ(CH_2^b) (18), ρ(CH_2^e) (12)
780sh	769	ν(ring-3) (12), ρ(CH_2^a) (22), ρ(CH_2^b) (13), ρ(CH_2^d) (30), ρ(CH_2^e) (11)
670sh		
643m,br		
629w,br	593	δ_{ip}(CNC) (86)
540w		
525w	529	δ(ring-3) (28), ρ(CH_2^c) (11)
518vw	482	δ_{op}(CNC) (82)
475vw	445	δ(ring-2) (66)
	440	δ(ring-3) (11), τ(ring-1) (23), δ(NCC^a) (13), δ(NCC^e) (12), δ_{op}(CNC) (15)
	392	δ(ring-1) (72)
	325	τ(ring-1) (40), τ(ring-3) (13), δ(NCC^a) (26)
	301	δ(ring-2) (10), τ(ring-3) (14),δ(NCC^a) (12), δ(NCC^e) (62)
	223	τ(ring-2) (99)
	131	τ(ring-3) (68), δ(NCC^e) (47)
	29	δ(CNC) (78), τ(NC) (23)
	2*i*	τ(NC) (100)
	69*i*	τ(CN---NC) (100)

6.3.2.1. *ν(CH) Region*

The bands in the 2800-3000 cm^{-1} region of both the IR and Raman spectra are considerably fewer in number than predicted, since there are a total of 11*a* and 11*b* ν(CH) vibrations (11a_u + 11a_g for the equatorial-C_i model). This is undoubtedly because many of these are grouped closely together and therefore not resolved. For example, in the Raman spectrum the very strong band at 2940 cm^{-1} can be identified with the ν_{as}(CH_2) vibration calculated at 2933 cm^{-1}, but the bands at 2854, 2896 and 2922 cm^{-1} undoubtedly each have contributions from at least three ν(CH_2) vibrations. The two higher wavenumber bands mainly involve antisymmetric CH_2 stretching, while the two lower wavenumber bands involve mainly symmetric CH_2 stretching, and stretching of the isolated CH group (on C4). In the IR spectrum only three bands are seen in the 2800-3000 cm^{-1} region, each of which must be a composite of at least three vibrations.

6.3.2.2. *Vibrations of the –N=C=N- Group*

Band positions for the stretching vibrations of the –N=C=N- moiety are in agreement with those reported in the literature for other carbodiimides[6,7]. The antisymmetric stretch appears as a very strong band in the IR at 2118 cm^{-1} while the symmetric stretch appears as a weak Raman band at 1406 cm^{-1}. No mention can be found in the literature of the NCN deformation. The DFT calculations indicate that this contributes to a number of normal coordinates, but mainly to that responsible for the very weak Raman band at 668 cm^{-1}. From the calculated force field we obtained the following GVFF force constants for the –N=C=N- moiety: f_r = 12.192 , f_{rr} = 0.976 , f_θ = 0.653 and $f_{r\theta}$ = 0.196 mdyn $Å^{-1}$. In the IR spectrum there is a shoulder on the low wavenumber side of the ν_{as}(C=N) band, at 2066 cm^{-1}, which we attribute to the combination of the symmetric stretch and deformation (1406 + 668 = 2074 cm^{-1}). The intensity of this combination band is quite weak, in accordance with *a* symmetry, since Fermi resonance cannot occur with the antisymmetric stretch, which has *b* symmetry.

6.3.2.3. *δ(CH) Region*

CH_2 deformations appear at 1446 and 1464 cm^{-1} in the Raman spectrum and at 1449 and 1463 cm^{-1} in the IR spectrum. The DFT calculations indicate that there is strong mixing of the deformations from the five symmetrically inequivalent CH_2 groups and that there are many fewer bands than expected due to their close proximity. Deformations of the solitary CH groups are strongly mixed with CH_2 wagging and twisting motions and can be identified with bands in the 1100-1400 cm^{-1} region in both IR and Raman. CH_2 rocking vibrations appear in both IR and Raman spectra spanning the range 900-1125 cm^{-1}.

6.3.2.4. *Skeletal Ring Vibrations*

Ring stretching and in-plane and out-of-plane deformation coordinates have been defined in terms of the combinations recommended by Pulay *et al.*[19], which are analogous to the Wilson symmetry coordinates used for benzene and its derivatives[20]. The symmetric ring breathing mode designated here as $\nu(ring^{-1})$, observed at 802 cm^{-1} in the Raman spectrum of cyclohexane, appears as a medium intensity strongly polarized band at 818 cm^{-1} in the Raman spectrum of DCC. Of the *b* symmetry normal modes a vibration which has principally ring breathing motion character is predicted at 781 cm^{-1}, corresponding to a weak band in the IR spectrum at 787 cm^{-1}. The other ring stretching motions are mixed to some extent with other coordinates but can be clearly observed in both IR and Raman in the region 789-1145 cm^{-1}. Most of the Raman bands attributable to ring stretching are strongly polarized.

Ring deformation modes appear as a series of weak bands in the Raman spectrum between 306 and 456 cm^{-1}, and also as higher wavenumber vibrations where they are coupled with other types of motion. Analysis of the DFT calculations indicates that the three ring deformation coordinates are mixed with each other and also with δ(NCC) motion. Ring torsional modes also appear as very weak bands in the Raman spectrum, below 300 cm^{-1}, and the DFT calculations show that these too are mixed with other types of vibrational motion.

6.3.2.5. *Melting studies*

Prior to solid to liquid phase transition Raman studies, the melting point (uncorrected) of DCC was established (using an open capillary tube) was measured on a Mettler Toledo FP62 apparatus, at a heating rate of 2 °C min-1 and found to be 34.5 °C, in agreement with the manufacturer's specification.

Figure 6.5 shows the Raman spectra for the temperature induced melt of DCC in the range 20 to 60 °C. Integrated Raman intensities in the ranges 725-805 and 2800-3000 cm^{-1}, as a function of temperature, are shown in Figure 6.6 indicating a melting temperature of *ca.* 34.5 °C in agreement with the measured melting point.

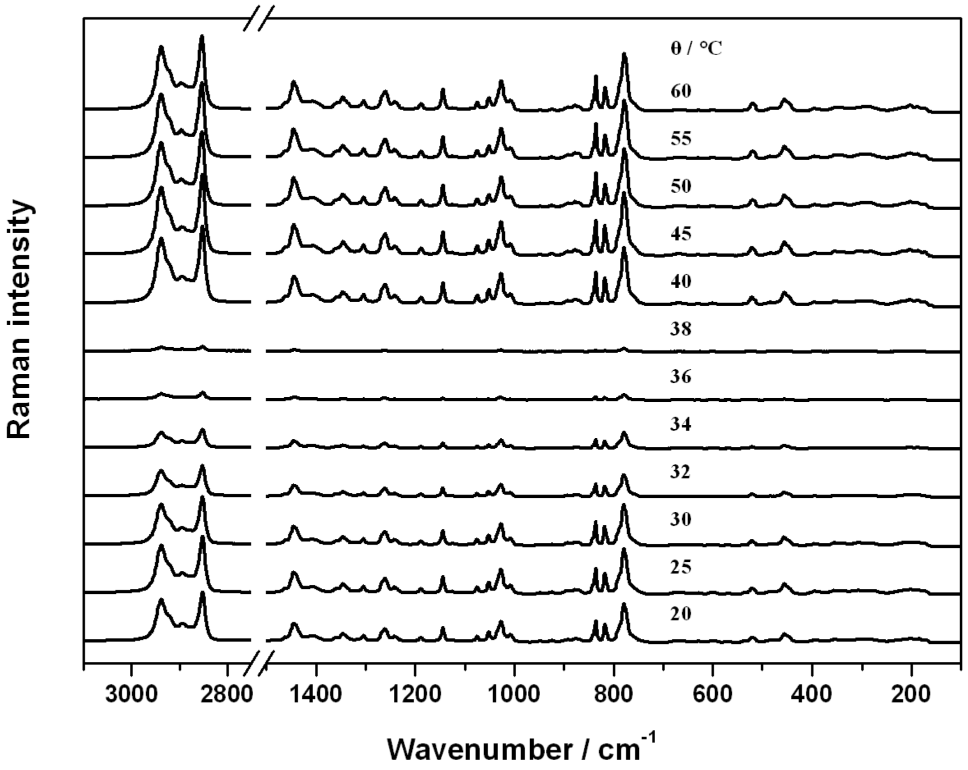

Figure 6.5. Raman spectra of DCC as a function of temperature over the range 20 to 60 °C.

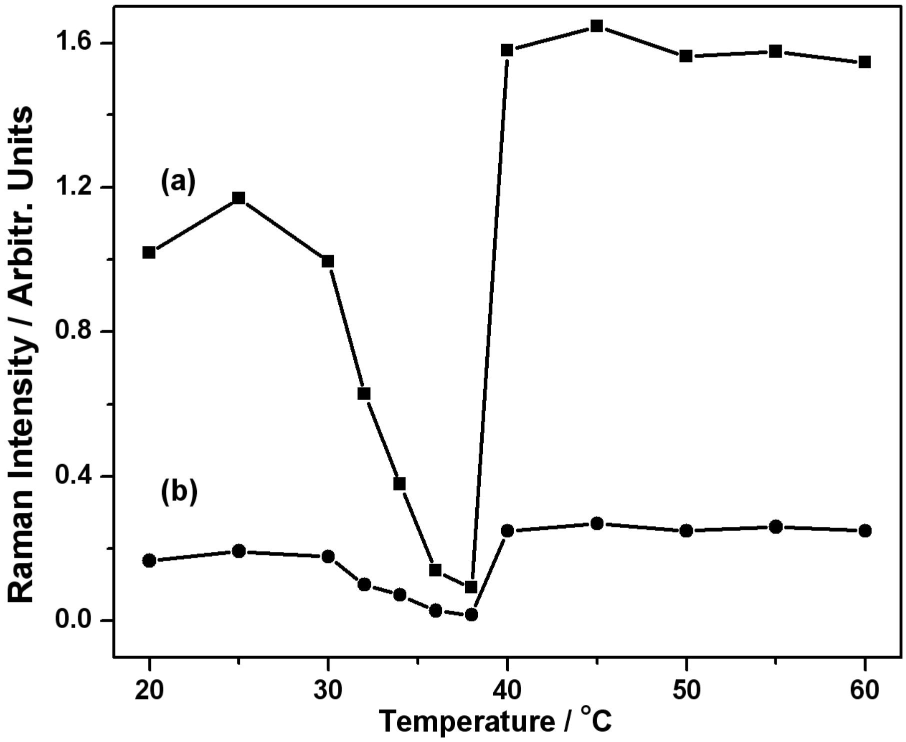

Figure 6.6. Melting profile of DCC from Raman intensity measurements as a function of temperature. (a) integrated Raman intensity in the range 2800 to 3000 cm^{-1}, and (b) integrated Raman intensity in the range 725 to 805 cm^{-1}.

The changes in the Raman spectral profiles can be explained in terms of the change in the DCC from the solid to the liquid state; the process being accompanied, in part, by a change in density of the material which is reflected in the changes in band intensities. Comparison of the solid and liquid phase Raman spectra reveals that band positions and relative intensities are identical, indicating no evidence for solid state effects. Thus in the solid state DCC molecules are held together by only weak van der Waals forces and any factor group splitting, if such exists, must be very small. This is supported by the observation that the solid-state and solution Raman spectra have identical relative band intensities and only very small differences in band wavenumbers, and the same is true for the solid state and solution IR spectra. However, one small difference between solid and liquid phase Raman spectra was found. The CH stretching band observed at 2851 cm^{-1} in the solid-state Raman spectrum shifts to 2854 cm^{-1} in the liquid state. This may reflect a change in orientation of the cyclohexyl rings upon melting.

6.4. Conclusions

The evidence demonstrates that a scaled quantum-chemical force field from B3-LYP/cc-pVTZ calculations of DCC as an isolated molecule in the gas phase provides an excellent fit to the observed IR and Raman spectra obtained in the solid, liquid and solution states. Although no crystal structure data are available for DCC the computed structure, of C_2 symmetry is nevertheless in good agreement with structures determined experimentally for related carbodiimide species. Normal coordinate analysis has provided detailed band assignments in terms of potential energy distributions and it appears that there are no solid state effects apparent in the vibrational spectrum, as evidenced by comparison of solid state and solution IR and Raman spectra, and by examination of the Raman spectrum as a function of temperature, above and below the melting temperature.

6.5. References

[1] S. Bräse, C. Gil, K. Knepper, *Bioorg. Med. Chem.* 2002, **10**, 2415.

[2] S.B. Vik, J.C. Long, T. Wada, D. Zhang, *Biochim. Biophys. Acta-Bioenerg.* 2000, **1458**, 457.

[3] K.A.S. Fernando, Y. Lin, B. Zhou, M. Grah, R. Joseph, L.F. Allard, Y. P. Sun, *J. Nanosci. Nanotechnol.* 2005, **5**, 1050.

[4] A. Garcia, M.A. Herrero, S. Frein, R. Deschenaux, R. Munoz, I. Bustero, F. Toma, M. Prato, *Phys. Status Solidi* A 2008, **205**, 1402.

[5] A. Gole, C.J. Murphy, *Langmuir* 2008, **24**, 266.

[6] G.D. Meakins, R.J. Moss, *J. Chem. Soc.* 1957, 993.

[7] P.H. Mogul, *Nucl. Sci. Abstr.* 1967, **21**, 47014.

[8] W. Jabs, M. Winnewisser, S.P. Belov, F. Lewen, F. Maiwald, G. Winnewisser, *Mol. Phys.* 1999, **97**, 213.

[9] G. Rapi, G. Sbrana, *J. Am. Chem. Soc.* 1971, **93**, 5213.

[10] E.A.V. Ebsworth, M.J. Mays, *Spectrochim. Acta* 1963, **19**, 1127.

[11] J.O. Jensen, *J. Mol. Struct.-Theochem* 2004, **686**, 173.

[12] C.H. Bushweller, J.W. O'Neill, *J. Org. Chem.* 1970, **35**, 276.

[13] *Gaussian03*, Revision E.03, M.J. Frisch, G.W. Trucks, H.B. Schlegel, G.E. Scuseria, M.A. Robb, J.R. Cheeseman, J.A. Montgomery, Jr., T. Vreven, K.N. Kudin, J.C. Burant, J.M.

Millam, S.S. Iyengar, J. Tomasi, V. Barone, B. Mennucci, M. Cossi, G. Scalmani, N. Rega, G.A. Petersson, H. Nakatsuji, M. Hada, M. Ehara, K. Toyota, R. Fukuda, J. Hasegawa, M. Ishida, T. Nakajima, Y. Honda, O. Kitao, H. Nakai, M. Klene, X. Li, J.E. Knox, H.P. Hratchian, J.B. Cross, V. Bakken, C. Adamo, J. Jaramillo, R. Gomperts, R.E. Stratmann, O. Yazyev, A.J. Austin, R. Cammi, C. Pomelli, J.W. Ochterski, P.Y. Ayala, K. Morokuma, G.A. Voth, P. Salvador, J.J. Dannenberg, V.G. Zakrzewski, S. Dapprich, A.D. Daniels, M.C. Strain, O. Farkas, D.K. Malick, A.D. Rabuck, K. Raghavachari, J.B. Foresman, J.V. Ortiz, Q. Cui, A.G. Baboul, S. Clifford, J. Cioslowski, B.B. Stefanov, G. Liu, A. Liashenko, P. Piskorz, I. Komaromi, R.L. Martin, D.J. Fox, T. Keith, M.A. Al-Laham, C.Y. Peng, A. Nanayakkara, M. Challacombe, P.M.W. Gill, B. Johnson, W. Chen, M.W. Wong, C. Gonzalez, J.A. Pople, Gaussian, Inc., Wallingford CT, 2004.

[14] J.A. Schachtschneider, *Vibrational analysis of polyatomic molecules, parts V and VI*, Technical Report Nos. 231 and 57, Shell Development Co.; Houston, 1964-1965.

[15] P. Pulay, G. Fogarasi, G. Pongor, J. E. Boggs, A. Vargha, *J. Am. Chem. Soc.* 1983, **105**, 7037.

[16] R. Kahn, R. Forne, A.M. Renaud, *Acta Chem. Scand. B* 1973, **29**, 131.

[17] N.B. Wilding, J. Crain, P. D. Hatton, G. Bushnell-Wye, *Acta Cryst. B* 1993, **49**, 320.

[18] S.T. Rao, M. Sundaralingam, *Acta Chem. Scand. B* 1969, **25**, 2509.

[19] P. Pulay, G. Fogarasi, F. Pang, J.E. Boggs, *J. Am. Chem. Soc.* 1979, **101**, 2550.

[20] G. Varsányi, *Vibrational Spectra of Benzene Derivatives*, Academic Press: New York, 1969.

7. Analysis of the Monomer Composition of Freeze-dried Poly (N-isopropylacrylamide/-vinylpyridine) Copolymer Microgels by Raman Spectroscopy

7.1. Introduction

Microgel particles are intra-molecularly cross-linked colloidal polymeric systems[1]. They are of both academic and applied interest. Microgels are particularly appealing academically because they provide an opportunity to investigate conformational changes in cross-linked, soft matter, polymeric systems. Nano-particle microgels also display interesting dispersion properties e.g. poly(N-isopropylacrylamide) [poly(NIPAM)], perhaps the most widely investigated microgel system, can reversibly de-swell and swell as a result of the application of external stimuli such as temperature, ionic strength, and solvent composition.[2] Microgels have been investigated for applications as diverse as rheological modification of materials, opto-electronic switches, water purification and drug delivery.[3] A wide range of techniques have been extensively used to characterise microgel systems including photon correlation spectroscopy (PCS), turbidity (usually as a function of temperature) and electrophoretic mobility measurements, transmission electron microscopy (TEM), small angle neutron scattering, differential scanning calorimetry, rheology, nuclear magnetic resonance and fluorescence spectroscopy.[4] There is a considerable amount of contemporary interdisciplinary scientific interest in the synthesis, physico-chemical characterization and academic as well as potential industrial/clinical applications of co-polymer microgels. The foregoing arises, in part, from the necessity to tailor-make microgels with particular microscopic and macroscopic properties (e.g. pH functionality) for specific applications.[5]

As part of a long term, systematic study of the synthesis and physico-chemical properties of microgel systems the current investigation examines the Raman spectral properties of freeze-dried homopolymer poly(NIPAM), poly(4-vinylpyridine) [poly(4-VP)] and copolymer poly(NIPAM/4-VP) *microgels*; the last prepared using different percentage compositions of 4-VP (relative to NIPAM) in the original synthetic reaction mixture. Besides fundamental knowledge base reasoning for conducting such a study, there are no known reports in the scientific literature of such analytical investigations from an applied perspective. A second (but equally important) reason is the problematic lack of suitable methods, of potentially wide applicability, for the qualitative/quantitative analysis of the monomeric composition of microgels. The poly(NIPAM/4-VP) copolymer microgel system is used herein to demonstrate *the principle* that Raman spectroscopy is a feasible technique for such purposes. This microgel system was chosen because its synthesis has been previously reported by two research groups.[6,7] In addition Pinkrah *et al.*, reported investigations of the physico-chemical properties of a poly(NIPAM/4-VP) microgel series of varying monomer ratios.[7]

A schematic for the synthesis of poly(NIPAM/4-VP) copolymer microgels is shown in Figure 7.1.

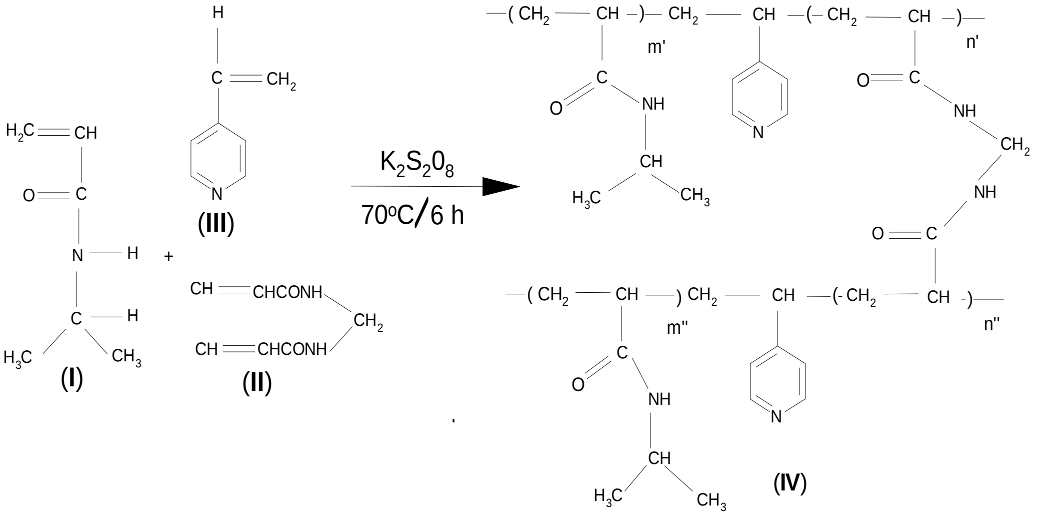

Figure 7.1. Synthesis of poly(NIPAM/4-VP) copolymer microgels (structures, **I**, **II**, **III**, and **IV**, represent N-isopropylacrylamide, N, N' methylenebisacrylamide, 4-vinylpyridine and poly(NIPAM/4-VP), respectively).

7.2. Results and Discussion

TEM micrographs of microgels[7] (not shown) showed a narrow size distribution of the colloidal particles and the PCS results were not significantly different from those previously reported for samples synthesized using the same starting compositions of reactants.[7]

The Raman spectra of freeze-dried microgels reported herein are, to our knowledge, the first examples of vibrational spectra of such systems to be examined although there have been several reports of the use of Raman spectroscopy in the study of *polymeric bulk gel systems*.[8-13] For example Appel *et al.*, have examined the interfacial thickening and smoothing of a NIPAM *hydrogel* (prepared via free radical polymerization), using Raman microimaging.[8] Moreover Appel and co-workers[9] also used Raman spectroscopy to characterize the temperature induced evolution of the pore structures of a macroporous NIPAM gel synthesized “using a suspension of 45 wt% toluene and 55 wt% pregel NIPAM solution”. In addition, Kato and Murakami have examined the VPT of neutral poly(NIPAM) *gels* (synthesized via free radical co-polymerization in water) immersed in “aqueous solutions of pyridine” using depolarized Rayleigh and Raman scattering.[10] Furthermore Hara and colleagues[11,12] have examined the low frequency Raman (and inelastic neutron scattering) spectra of dehydrated polyacrylamide gels. In relation to the foregoing studies, the Raman spectra shown herein have been obtained at a low laser exciting power (8 mW) compared to previous (between 50 and 300 mW) studies on any type of gel system; thus minimizing the possibility of problems arising from heating and/or photolytic effects. Moreover, the Raman spectra are rich in vibrational bands; in fact none of the previously cited studies of any microgel system have reported Raman vibrational data over the entire spectral region (0-4000 cm^{-1}), especially between 2600 and 3600 cm^{-1}.

Figure 7.2 shows the Raman spectral profiles of freeze-dried samples of homopolymeric poly(NIPAM) and homopolymeric poly(4-VP) microgels. There are, as expected, significant, totally reproducible, differences in the Raman vibrational band profiles of the two microgels.

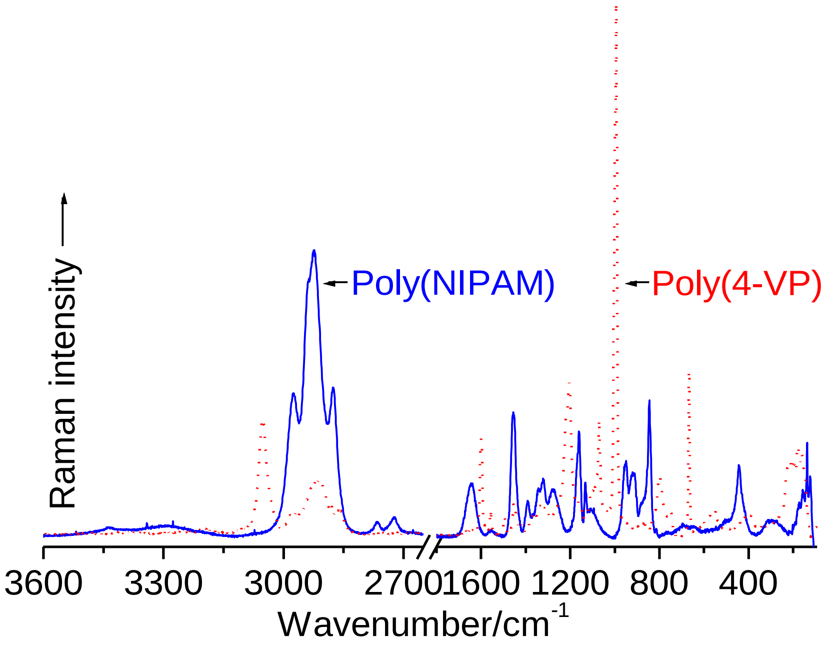

Figure 7.2. Raman spectra of: (a) poly(NIPAM) and poly(4-VP) homopolymer microgels over the 100 - 3600 cm^{-1} range

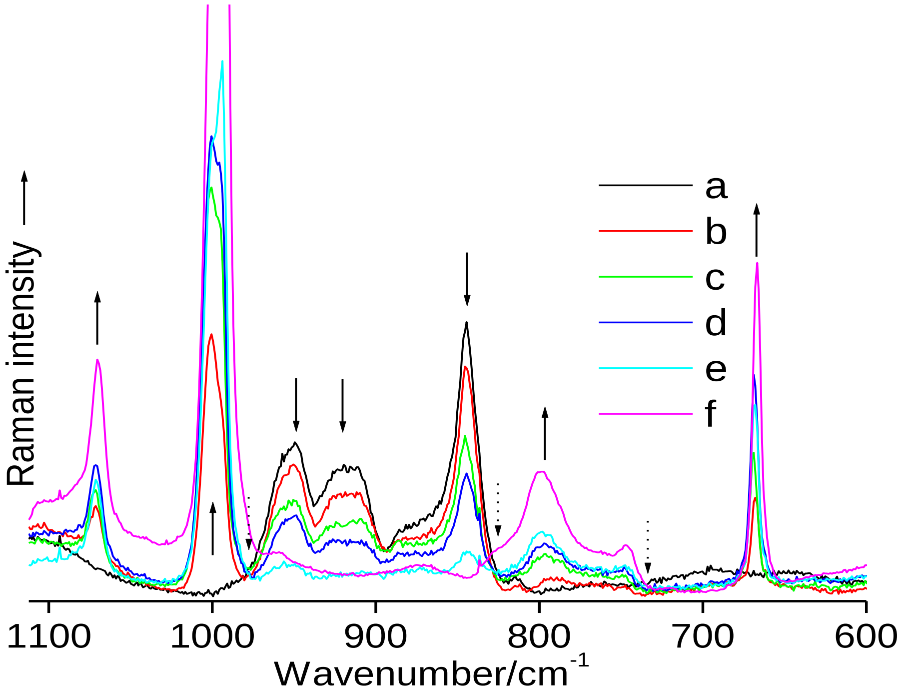

Figure 7.3. Raman Spectra of poly(NIPAM/4-VP) copolymer microgels, in the 600 -1100 cm^{-1} region.

The symbols a – f, in Figure 7.3 refer to freeze-dried microgels synthesized using percentage composition of 4-VP relative to NIPAM) of 0, 15, 25, 35, 55, and 100 respectively. The upward arrows indicate increasing intensities of the 4-VP Vibrational bands, whereas the downward arrows indicate decreasing intensities of the NIPAM vibrational bands and the dotted arrows indicate isosbestic points.

In addition Figure 7.3 shows, in an expanded plot, the differences in vibrational band intensities and wavenumber locations, over the 600-1100 cm^{-1} region, of the Raman spectral profiles for poly(NIPAM), poly(4-VP), and poly(NIPAM/4-VP microgels; the latter synthesized using percent composition of 7.5, 15, 25, 35, 55, 75, and 90% (w/w) of the 4-VP monomer (*relative* to the NIPAM monomer) in the original one pot reaction mixture.

The vibrational bands between ~2802 and 3000 cm^{-1} (due to aliphatic and aromatic C-H asymmetric/symmetric stretching modes; Figure 7.2) decrease in Raman intensity in the spectral profile of poly(4-VP) microgels compared to poly(NIPAM) microgels. The vibrational bands at *circa* 2723 and 2765 cm^{-1} (tentatively assigned to overtones of C-H bending vibrations in the 1300-1400 cm^{-1} region) are not present in the Raman profile of the poly(4-VP) microgel, whilst the 3051 cm^{-1} vibrational band, due to aromatic C-H stretching vibrational modes of pyridine present in the Raman profile of poly(4-VP) microgel is, as expected, absent in the Raman spectrum of the poly(NIPAM) microgel. In addition there are no Raman vibrational bands in the 3125-3500 cm^{-1} region for the freeze-dried poly(4-VP) microgel, whilst weak (low intensity) vibrational bands, due to different vibrational modes of “structural” water, are present in this region for poly(NIPAM). The foregoing statement is reconciled in view of the relative non-polar nature of the 4-VP monomer compared to that of the NIPAM monomer used in the synthesis of the poly(NIPAM) microgel.

Figure 7.4 shows a graphical analysis of the vibrational spectroscopic data, relating the initial percentage composition of 4-VP used in the synthesis of the poly(NIPAM/4-VP) microgels and the intensities (band areas) of specific Raman vibrational bands. The relative intensities of selected vibrational bands, of primary analytical interest, were estimated (from their band areas) using the software provided by the Raman instrument manufacturer.

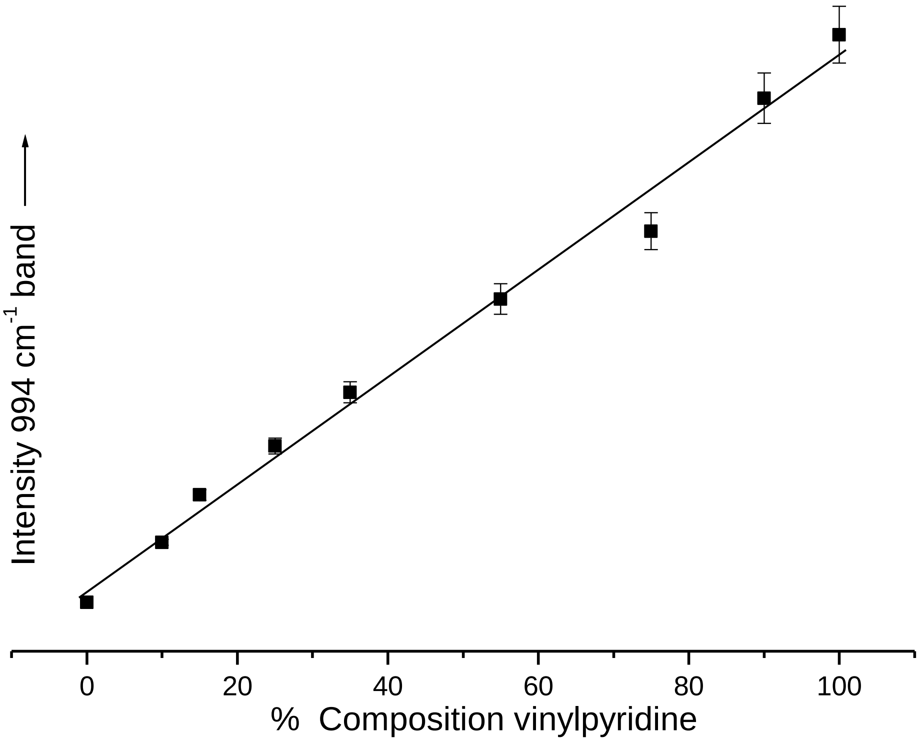

Figure 7.4. Graphical plot of the intensity of the ~994 cm^{-1} vibrational band of 4-VP for the poly(NIPAM/4-VP) copolymer freeze-dried microgels as a function of the percentage composition of 4-VP (relative to NIPAM) used in the original synthesis of the microgels.

It is noteworthy that many different vibrational bands could be used for analysis of the data relating vibrational band areas to 4-VP content of the poly(NIPAM/4-VP) microgels in different regions of the Raman spectra. However, as an exemplar, the vibrational band at about 994 cm^{-1} (assigned to the ring breathing mode of the pyridine moiety), see Figure 7.3, gives a linear relationship between vibrational band areas and percentage composition of 4-VP used in the synthesis of the microgels. It is to be noted that the values for the percentage composition of 4-VP on the abscissa axis of Figure 7.4 are not absolute because of losses during synthesis and purification. Attempts to obtain the Raman spectrum of pure 4-VP monomer were unsuccessful due to intrinsic fluorescence.

In view of the results presented above, there is a strong case to be made for Raman spectroscopy to be used as a novel, quick and easy method for assessing the relative level of incorporation of monomers into co-polymer microgels. Not withstanding the fact that Raman spectroscopy is a relatively specialised technique (compared e.g. to NMR spectroscopy, fewer laboratories are equipped with Raman instrumentation), the data show that the technique can be used to monitor the incorporation of the 4-VP as well as the decrease in the expected levels of the "base monomer", in this case NIPAM. Of course, the current study was devised to show the conceptual idea that in *principle*

Raman spectroscopy can be utilized for the foregoing purposes. It is to be noted that in the case of poly(NIPAM/4-VP) microgels the *relative trend* in increasing 4-VP content of these copolymer microgels synthesized using different starting ratios of the quantities of N-isopropylacrylamide to 4-VP in the reaction mixture can be established using UV spectroscopy.[7] However such an analysis assumes, *a priori*, that the extinction coefficient (molar absorptivity) for the vinyl pyridine monomer is, to a first approximation, the same as that in the polymer. Such an assumption is, of course, contentious. Also, there is no reason why Raman spectroscopy should not be applied to molecules that are not amenable to analysis by UV/VIS spectroscopy (i.e. are devoid of a suitable spectrophotometric chromophore) and/or a chemical moiety capable of being analysed using potentiometric/conductimetric methods. The structural information contained within Raman spectra is much greater than that attained by the use of UV/VIS spectroscopic techniques (as there are many more vibrational modes than there are electronic transitions for a given molecule). Also compared to using e.g. solid state NMR spectroscopy for the purpose of analysis of monomer composition, Raman spectroscopy is much less time consuming (Raman spectral acquisition time is < 10 mins), the measurements are easy to make and very small quantities of the material under investigation are required. In fact the Raman spectroscopic analyses of freeze-dried microgel samples can be conducted on “micrometre size” quantities of (“solid state”) material. Attempts to use solid state NMR spectroscopy for analysis of the composition of poly(NIPAM/4-VP) microgels by utilizing a 300 MHz NMR spectrometer (using a 6 mm diameter zirconium oxide rotor and cross polarization magic angle spinning or magic angle spinning gated decoupled pulse sequences), although successful, resulted in the acquisition of NMR spectra which took 2-3 hrs to attain and required 100-200 mg of sample. Interestingly, Hoare and Pelton[14] have reported the *indirect* determination of methacrylic acid (MAA), acrylamide (AM) and NIPAM in “(AM)/NIPAM and MAA/NIPAM copolymer” microgels using ^{1}H-NMR (500MHz) spectroscopy of lyophilized microgel samples *suspended* in deuteriated methanol. Moreover they also reported that conductimetric titration analysis allowed a direct measure of the MAA content of a MAA/NIPAM microgel. Although ^{1}H-NMR spectroscopy may be a useful method for the analytical determination of the composition of microgel components, it can be problematic in certain cases because of solubility problems (giving rise to suspensions) which in turn give broad-line chemical shifts.

Detailed Raman spectra (covering all spectral regions) together with vibrational band assignments and analyses of the relationship between vibrational band intensities and monomer composition (in spectral regions other than 600-1100 cm^{-1}) for other freeze-dried microgels are currently being investigated. In addition the use of internal standards (*e.g.* barium sulphate) and the use of relative band intensities for analysis of the composition of copolymer microgels will also be reported in the near future.

7.3. Conclusions

Raman spectroscopy has been demonstrated to be a novel, useful analytical technique for the qualitative and semi-quantitative analysis of the monomeric composition of poly(NIPAM/4-VP) co-polymer microgel dispersions.

7.4. References

[1] B.R. Saunders, B. Vincent, *Adv. Colloid Interface Sci*, 1999, **80**, 1.

[2] E. Daly, B.R. Saunders, *Phys. Chem. Chem. Phys*, 2000, **2**, 3187.

[3] M. Murray, B.Z. Chowdhry, M.J. Snowden, *Chemistry in Industry*.

[4] V.T. Pinkrah, PhD thesis, University of Greenwich, 2004.

[5] L. Benee, M.J. Snowden, B.Z. Chowdhry, *Encyclopedia of Advanced Materials*, John Wiley & Sons Ltd, New York, 2002.

[6] M. Iwaku, T. Haseba, T. Tatsuma, N. Oyama, J. *Electroanalytical Chemistry* 1998, **442**, 27.

[7] V.T. Pinkrah, M. J. Snowden, J. C. Mitchell, B. Z Chowdhry, J. Siedel, G. R. Fern, Langmuir, 2003, **19**, 585.

[8] R. Appel, T.W. Zerda, C. Wang, Z. Hu, *Polymer*, 2001, **42**, 1561.

[9] R. Appel, W. Xu, T.W. Zerda, Z. Hu, *Macromolecules*, 1998, **31**, 5071.

[10] E. Kato, T. Murakami, *Polymer*, 2002, **43**, 5607.

[11] K. Hara, A. Nakamura, N. Hiramatsu, A. Matsumoto, *Physica B: Condensed Matter*, 1999, **263-264**, 350.

[12] K. Hara, A. Nakamura, N. Hiramatsu, T. Kanaya, *Physica B: Condensed Matter*, 1997, **241-243**, 350.

[13] Y. Takasu, Y. Suzuki, I. Nishio, Proceedings of the Fourteenth International Conference on Raman Spectroscopy, Eds: N.-T. Yu, X.-Y. Li, John Wiley, 1994.

[14] T. Hoare, R. Pelton, *Langmuir* 2004, **20**, 2123.

8. Summary

Solid state IR and Raman as well as aqueous solution state Raman spectra have been obtained for urazole, 4-methylurazole and their anions for both deuterated and non-deuterated species. DFT calculations were undertaken at the B3-LYP/cc-pVTZ level for all the molecular species examined experimentally. The aforementioned calculations allowed the vibrational spectra to be computed, at the optimised molecular geometry/minimum energy, in the presence of solvent molecules. In the case of aqueous solution Raman spectra the structures and vibrational spectra could be accounted for using models which incorporated the conductor-like polarisable continuum solvation method together with explicit hydrogen-bonded water molecules. Normal coordinate analysis was also undertaken which yielded calculated vibrational spectra (IR and Raman) which were in good agreement with the experimental spectra. For all molecular species examined, computed potential energy distributions of the normal modes provided detailed vibrational assignments.

IR (solid sate) and Raman (solid state and in chloroform solution) have also been obtained for N, N'–dicyclohexylcarbodiimide (DCC). The computed vibrational spectra (again at the B3-LYP/cc-pVTZ level) together with the experimental spectra provide evidence that the DCC exhibits C_2 structure in both the solid and solution states. The melting behavior of DCC was also examined using variable temperature dependent Raman spectroscopy.

Freeze-dried samples of homopolymeric and co-polymer microgels have been studied using Raman spectroscopy. The latter were examined as a function of the ratio of the individual monomers. It was found that Raman spectroscopy could be used to ascertain, semi-quantitatively, the monomeric composition of the co-polymer microgels.

8.1. Future Work

Possible work that could be undertaken in order to extend, support and complement the studies reported in this thesis is as follows.

(1) Undertake surface enhanced Raman scattering (SERS) studies of urazole and 4-methylurazole. Such studies would allow:

    (i) a comparison of the SERS spectra with Raman spectra obtained from solid and aqueous state samples, and hence elucidation of the nature of the molecule-metal interaction.

    (ii) the determination of the limits of detection for the urazole compounds for semi-quantitative/quantitative analyses.

    (iii) the experimental SERS spectra of the interactions of the analyte molecules (urazole/4-methylurazole) with substrates (e.g. silver or gold colloids) to be compared with calculated SERS spectra obtained using the Gaussian program.

(2) It would be useful to obtain inelastic neutron scattering (INS) data for the two molecules. A comparison of the INS spectra of the deuterated and non-deuterated species would be particularly worthwhile because of the differences in the neutron scattering cross-sections of hydrogen and deuterium atoms. These studies would complement those already undertaken because INS could provide information relating to hydrogen-bonding dynamics in molecules.

(3) The microgel Raman studies reported in this thesis, using Raman, could certainly be extended by:

    (i) examining other co-polymeric microgel systems, and

    (ii) interrogating their SERS spectra. The SERS spectra of microgels have not been reported in the literature. It would be useful to compare the SERS spectra with those of the freeze-dried microgels. In addition it would be interesting to conduct the SERS experiments of microgels as a function of temperature. This would allow the volume phase transition temperature (VPT), of such macromolecular species, obtained by SERS to be evaluated and compared/contrasted with the VPT obtained using "classical" techniques such as turbidity measurements.

8.2. Addendum

8.2.1. Published Papers

Vibrational spectra and structures of urazole and 4-methylurazole: DFT calculations of the normal modes in aqueous solution and in the solid state, and the influence of hydrogen bonding – J.P. Ryall, T.J. Dines, B.Z. Chowdhry, S.A. Leharne, R. Withnall, *Chem. Phys.*, 2010, **373** 219.

8.2.2. Manuscripts in Press

Vibrational spectroscopy and DFT calculations of *N*, *N'*-dicyclohexylcarbodiimide – Babur Z. Chowdhry, Trevor J. Dines, Stephen A. Leharne, John P. Ryall, Iqbal T. Shadi, Robert Withnall [DOI: 10.1002/J. Raman Spectrosc., 2674 (2010)]

8.2.3. Submitted Manuscripts

Vibrational spectra and structures of the anions of urazole and 4-methylurazole: DFT calculations of the normal modes and the influence of hydrogen bonding – John P. Ryall, Trevor J. Dines, Babur Z. Chowdhry, S.A. Leharne and Robert Withnall (Submitted: Spectrochimica Acta; August, 2010)

8.2.4. Manuscripts in Preparation

Experimental and theoretical studies of eugenol and isoeugenol – J.P. Ryall, T.J. Dines, B.Z. Chowdhry and R.Withnall (To be submitted: Phys. Chem. Chem. Phys., 2010)

Experimental and theoretical studies of the IR and Raman spectra of 2-, 3- and 6- fluoro-x-deoxy-D-glucose molecules – J.P. Ryall, T. J.Dines, B.Z. Chowdhry and R.Withnall (To be submitted: J. Raman Spectrosc., 2010)

8.2.5. Conference Posters

Proceedings of the XIX International Conference on Raman Spectroscopy, (Brisbane, Australia), J. Wiley & Sons (2004).

Eds: P. Fredericks, R.L. Frost and L. Rintoul (2004)

Raman studies of amygdalin**, Ryall J.P.**, Shadi I.T., Withnall R., Dines T.J., Chowdhry B.Z, pp., 392–393.

Raman spectroscopy of structurally related chemically substituted carbohydrates: xfluoro-x-deoxy-d-glucose molecules, **Ryall J.P.**, Withnall R., Dines T.J., Chowdhry B.Z, pp., 394–395.

Raman spectroscopic studies of chemically modified pullulans, Gibson G.H., **Ryall J.P.**, Snowden M.J., Mitchell J.C., Withnall R., Chowdhry B.Z, pp., 398–399.

Interrogation of poly (N-isopropylacrylamide-bisacrylamide) microgel nanoparticles by Raman spectroscopy, **Ryall J.P.**, Withnall R., Mitchell J.C., Snowden M.J., Chowdhry B.Z, pp., 586–587.

Eugenol and isoeugenol: Raman, FT-IR and *ab initio* calculations, **Ryall J.P.**, Withnall R., Dines T.J., Chowdhry B.Z, pp., 384–385.

Analysis of the butylacrylate composition of co-monomer microgels by Raman spectroscopy, Gracia L.H., **Ryall J.P.**, Mendham A.P., Withnall R., Mitchell J.C., Snowden M.J., Chowdhry B.Z, pp., 590–591.

A novel use of Raman spectroscopy: analysis of the structural composition of comonomer microgels, **Ryall J.P.**, Mendham A.P., Withnall R., Gracia L.H., Pinkrah V. T.P., Mitchell J.C., Snowden M.J., Chowdhry B.Z, pp., 588–589.

4-methylurazole: Raman, FT-IR and *ab initio* calculations, **Ryall J.P.**, Withnall R., Dines T.J., Chowdhry B.Z, pp., 396–397.